Thi-Qar University Journal for Engineering Sciences, Vol. 4, No.3 2013

Numerical Investigation of Heat Transfer in Parallel Rectangular Microchannel Heat Exchanger

MSc. Hayder Mohammed Hasan

Shatra Technical Institute, Machines and Equipments department

ABSTRACT

The axial heat conduction in parallel flow microchannel heat exchanger with rectangular ducts was numerically investigated, for laminar, 3-D, incompressible, and steady state flow of water. The governing equations, continuity, Navier-Stokes equations (momentum equations), and the energy equations for the hot and cold fluids were solved by using SIMPLE algorithm with finite volume method and FORTRAN code to obtain the temperature distribution for the two fluids and the separating wall between them.

The results play an important role of the axial heat conduction on the effectiveness in parallel flow microchannel heat exchanger and the factors affecting the axial heat conduction are; Reynolds number Re, thermal conductivity ratio K_r, aspect ratio α and channel volume. Increasing of Re, K_r, α and channel volume each separately leads to increase the axial heat conduction and vice versa.

دراسة عددية لإنتقال الحرارة في مبادل حراري مايكروي متوازي ذي قنوات مستطيلة الشكل

م.م حيدر محمد حسن

المعهد التقني في الشطرة/ قسم المكائن والمعدات

الخلاصة

عدديا تمت دراسة تأثير التوصيل الحراري المحوري في مبادل حراري مايكروي ذي قنوات مستطيلة الشكل لجريان متوازي طباقي ثلاثي الأبعاد للماء وفي حالة الاستقرار ولا انضغاطي. تم حل المعادلات الحاكمة للجريان وهي معادلة الاستمرارية (continuity equation) ومعادلات الزخم (momentum equations) و معادلة الطاقة (energy equations) باستخدام طريقة (SIMPLE method) وقد تم تحويل المعادلات

الحاكمة إلى الشكل العددي باستخدام طريقة الحجوم المحددة (finite-volume method) وباستخدام لغة فورتران (FORTRAN). بهذه الطريقة تم إيجاد التوزيع لدرجتي حرارة المائعين والجدار الذي يفصل بينهما.

من خلال ملاحظة النتائج المستحصلة من الحل العددي، تبين بأن هنالك تأثير مهم للتوصيل الحراري المحوري على الفعالية في المبادل المايكروي كما إن هنالك مجموعة من العوامل التي تؤثر عليه وهي، عدد رينولدز(Reynolds number Re) ونسبة الموصلية الحرارية (K_r thermal conductivity ratio) والنسبة الباعية (α aspect ratio) وحجم القنوات. عند زيادة Re و K_r وα وحجم القنوات كل على حدة يزداد التوصيل الحراري المحوري، والعكس صحيح.

KEYWORDS: microchannel, heat exchanger, parallel flow, numerical solution, axial heat conduction and effectiveness.

NOMENCLACHRE

English symbols

c	specific heat . .. . J/(kgK)
C_c	heat capacity of cold fluid … *W/K*
C_h	heat capacity of hot fluid … *W/K*
C_{min}	minimum heat capacity ….. *W/K*
C_p	specific heat at constant pressure ..... J/(kgK)
D_h	hydraulic diameter . .. . *m*
H	channel height . . . . *m*
$H_{H.E}$	exchanger height .... *m*
k	thermal conductivity . . . . .*W/mK*
L	channel length . .. . *m*
$\dot{m}$	mass flow rate . . . . *kg/s*
p	pressure . . .. *Pa*
q	heat transfer rate . . ..*W*
T	temperature . . . . . *K*
t_s	separating wall thickness . . . . . *m*
u	fluid *x*-component velocity . . *m/s*
v	fluid *y*-component velocity . . . *m/s*
w	fluid *z*-component velocity ... . .*m/s*
W_{ch}	channel width . . . .*m*
$W_{H.E}$	exchanger width .... *m*
x	axial coordinate . .. .*m*

Greek symbols

ε	heat exchanger effectiveness
μ	dynamic viscosity . . . . *Pa.s*
ρ	density . . . . . *kg/m³*

Dimensionless groups

$K_r = k_s / k_f$	thermal conductivity ratio
$Re = \rho u_{h,in} D_h / \mu$	Reynolds number
$\Pr = \frac{\mu C_p}{k_f}$	prandtl number
$Pe = \mathrm{RePr}$	Peclet number
$\alpha = H/W$	aspect ratio

Subscripts

c	cold fluid
h	hot fluid
f	fluid
in	inlet
max	maximum value
min	minimum value
out	outlet
s	solid
u	unit
w	water

Superscripts

y horizontal coordinate . .. . m

z vertical coordinate . . . .m

1. INTRODUCTION

The fluid flow in microchannels becomes an attractive area of research during the last few years. This is due to the new applications of the microchannel flow in micro pumps, micro turbines, micro heat exchangers and other micro components. Advantages of compact structure and high heat transfer performance make the microscale heat exchangers showing a nice foreground on microelectronics, micro devices fabrication, bioengineering, micro electromechanical system (MEMS), and so on. Thus, is becoming more popular, both for commercial purposes and in scientific research [1]. Microchannel heat exchangers can be broadly classified as fluidic devices that employ channels of hydraulic diameter smaller than 1 mm [2]. Knudsen number is a measure of the degree of the rarefaction which is defined as the ratio of mean free path to the characteristic length scale of the system $Kn = \lambda / L_c$ where, λ is the mean free path and L_c is the characteristic length such as channel equivalent diameter. The flow regimes could be classified as: continuum regime when (Kn<0.001), slip flow regime (0.001<Kn<0.1), transient regime (0.1<Kn<10) and free molecular regime (Kn>10). In order to simulate the no slip flow regime, the Knudsen number is Kn<0.001. In conventional heat exchanger the solid thickness is small comparatively with the hydraulic diameter; therefore the axial heat conduction may be neglected. This means that the performance of the heat exchanger is primarily depending upon the flow in the ducts (fluid properties and mass flow rate). For microchannel heat exchanger, the solid thickness is large comparatively with the hydraulic diameter, therefore the axial heat conduction in the separating wall (solid) is important and the microchannel heat exchanger effectiveness may decrease due to the effect of axial heat conduction. The present study is deal with effect of the axial heat conduction in microchannel heat exchanger.

To understand the flow through microchannels, many researchers have been investigaty experimentally, analytically and numerically in last decade. For example, Al bakhit et al. [3] numerically investigated the flow and heat transfer in parallel flow microchannel heat exchangers. They used a hybrid approach, in which the nonlinear momentum equations for one or two channels were solved using CFD codes. The

velocity field was an input into a user developed code for solving the energy equation and they studied heat transfer for thermally developing laminar flow in two parallel rectangular channels which represent some kind of heat exchangers. From the results, it is found that in the entrance region the developing velocity profiles lead to higher values of overall heat transfer coefficient. Al-Nimr et al. [4] numerically investigated the hydrodynamics and thermal behaviors of the laminar, 2-D, fully developed, slip flow inside an insolated parallel-plate microchannel heat exchanger. They showed that both the velocity slip and the temperature jump at the walls increase with increasing Knudsen number. Yin and Bau [5] studied flow between infinite parallel plates and circular pipes to study the effect of axial heat conduction on the performance of microchannel heat exchangers. They used a fully developed velocity field and analytically they solved for temperature fields in the channel and solid wall. They found that, the axial conduction plays an important role at the entrance region. Stief et al. [6] numerically investigated the effect of solid thermal conductivity in micro heat exchangers. They showed that the reduction of conductivity of the wall material can improve the heat transfer efficiency of the exchanger due to influence of axial heat conduction in the separation wall. Also, they concluded that increasing heat capacity ratio leads to a reduction in effectiveness for all Knudsen number. Al-bakhit and Fakheri [7] numerically investigated the laminar, parallel flow microchannel heat exchanger with rectangular ducts for developing and fully developing velocity profiles with thermally developing flow in both cases. They showed that the overall heat transfer coefficient is rapidly changed for $x/D_h Pe$ (Graetz number) below 0.03, and therefore the assumption of constant overall heat transfer coefficient is not valid if the Graetz number based on the heat exchanger length is of the order of 0.03. Also, the accurate results can be obtained by solving thermally developing energy equation using fully developed velocity profiles. Mushtaq I. Hasan [8] made numerical investigation to study the counter flow microchannel heat exchanger with different channel geometries and working fluids. He studied the effect of axial heat conduction on the performance of counter flow microchannel heat exchanger with square shaped channel and he found that the existing of axial heat conduction lead to reduce the heat exchanger effectiveness.

ANALYSI

Schematic structure of a parallel flow microchannel heat exchanger with square channels is shown in figures 1 and 2 illustrated in with of channels details with rectangular profiles.

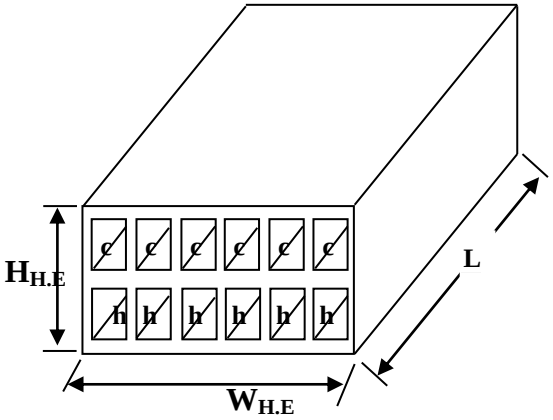

Figure 1 Schematic model of microchannel heat exchanger under concentration.

To study the entire parallel flow microchannel heat exchanger numerically, it is complicated and needs huge CPU time. Due to the symmetry between channels, the individual heat exchange unit is considered consists of two channels (hot and cold) with separating wall as shown in figure 2. Heat is transferred from hot fluid to cold fluid through the thick wall separating between them and this heat exchange unit represents a complete exchanger and gives an adequate indication about its performance.

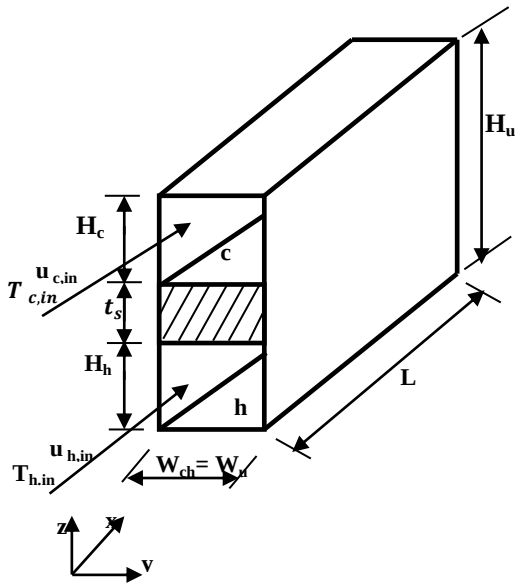

Figure 2 Three-dimensional sketch of the parallel flow heat exchanger unit.

However, the governing equations for the present model are based on the following physical and geometrical assumptions [9]:

- The flow is laminar and steady.
- The Knudsen number is small enough, so that the fluid is regard as continuous medium (no slip).
- The fluids are incompressible, Newtonian, with constant properties; in this case the water is used as working fluid.
- There is no heat transfer to/from the ambient medium.
- The energy dissipation is negligible.
- The pressure gradient is in axial direction only.
- Three dimensional of the flow and heat transfer.

The governing equations and its boundary conditions in Cartesian coordinates and nondimesionalized using the following variables according to [3]

$$x^* = \frac{x}{D_h},\ y^* = \frac{y}{D_h},\ z^* = \frac{z}{D_h},\ t_s^* = \frac{t_s}{D_h},\ W_{ch}^* = \frac{W_{ch}}{D_h}, H_i^* = \frac{H_i}{D_h},\ u_i^* = \frac{u_i}{u_{h,in}},\ v_i^* = \frac{v_i}{u_{h,in}}$$

$$, w_i^* = \frac{w_i}{u_{h,in}},\ p_i^* = \frac{p_i}{\rho u_{h,in}^2}, T_i^* = \frac{T_i - T_{c,in}}{T_{h,in} - T_{c,in}} \text{ and } \quad T_s^* = \frac{T_s - T_{c,in}}{T_{h,in} - T_{c,in}}$$

Continuity equation

$$\frac{\partial u_i^*}{\partial x^*} + \frac{\partial v_i^*}{\partial y^*} + \frac{\partial w_i^*}{\partial z^*} = 0 \qquad (1)$$

x-momentum equation

$$u_i^* \frac{\partial u_i^*}{\partial x^*} + v_i^* \frac{\partial u_i^*}{\partial y^*} + w_i^* \frac{\partial u_i^*}{\partial z^*} = -\frac{dp_i^*}{dx^*} + \frac{1}{Re_i}\left(\frac{\partial^2 u_i^*}{\partial x^{*2}} + \frac{\partial^2 u_i^*}{\partial y^{*2}} + \frac{\partial^2 u_i^*}{\partial z^{*2}}\right) \qquad (2)$$

y-momentum equation

$$u_i^* \frac{\partial v_i^*}{\partial x^*} + v_i^* \frac{\partial v_i^*}{\partial y^*} + w_i^* \frac{\partial v_i^*}{\partial z^*} = \frac{1}{Re_i}\left(\frac{\partial^2 v_i^*}{\partial x^{*2}} + \frac{\partial^2 v_i^*}{\partial y^{*2}} + \frac{\partial^2 v_i^*}{\partial z^{*2}}\right) \qquad (3)$$

z- momentum equation

$$u_i^* \frac{\partial w_i^*}{\partial x^*} + v_i^* \frac{\partial w_i^*}{\partial y^*} + w_i^* \frac{\partial w_i^*}{\partial z^*} = \frac{1}{Re_i}\left(\frac{\partial^2 w_i^*}{\partial x^{*2}} + \frac{\partial^2 w_i^*}{\partial y^{*2}} + \frac{\partial^2 w_i^*}{\partial z^{*2}}\right)$$

(4)

energy equation for fluid

$$u_i^* \frac{\partial T_i^*}{\partial x^*} + v_i^* \frac{\partial T_i^*}{\partial y^*} + w_i^* \frac{\partial T_i^*}{\partial z^*} = \frac{1}{Pe_i}\left(\frac{\partial^2 T_i^*}{\partial x^{*2}} + \frac{\partial^2 T_i^*}{\partial y^{*2}} + \frac{\partial^2 T_i^*}{\partial z^{*2}}\right)$$

(5)

where *i* is represented the subscript h or c which refer to the lower and upper (hot and cold) channels respectively. The diffusion equation for solid becomes

$$\frac{\partial^2 T_s^*}{\partial x^{*2}} + \frac{\partial^2 T_s^*}{\partial y^{*2}} + \frac{\partial^2 T_s^*}{\partial z^{*2}} = 0$$

(6)

The dimensionless boundary conditions are:

For lower channels (hot fluid) $(0 \le z^* \le H_h^*)$

At $x^* = 0$,$0 \le y^* \le W_{ch}^*$

$$u_{h,in}^* = 1, v^* = 0, w^* = 0, T_h^* = 1$$

$$p_{h,in}^* = \frac{p_{h,in}}{\rho\, u_{h,in}^2}$$

At $x^* = \frac{L}{D_h}$, $0 \le y^* \le W_{ch}^*$

$$\frac{\partial u^*}{\partial x^*} = \frac{\partial v^*}{\partial x^*} = \frac{\partial w^*}{\partial x^*} = \frac{\partial T_h^*}{\partial x^*} = 0$$

At $y^* = 0$, $0 \le x^* \le L^*$

$$u^* = v^* = w^* = \frac{\partial T_h^*}{\partial y^*} = 0$$

At $y^* = W_{ch}^*$, $0 \le x^* \le L^*$

$$u^* = v^* = w^* = \frac{\partial T_h^*}{\partial y^*} = 0$$

At $z^* = 0$,$0 \le x^* \le L^*$, $0 \le y^* \le W_{ch}^*$

$$u^* = v^* = w^* = \frac{\partial T_h^*}{\partial z^*} = 0$$

Fluid -solid interface

At $z^* = H_h^*$, $0 \le x^* \le L^*$, $0 \le y^* \le W_{ch}^*$

$$u^* = v^* = w^* = 0$$

$$\frac{\partial T_h^*}{\partial z^*} = K_r \ \frac{\partial T_s^*}{\partial z^*}$$

For upper channel (cold fluid) $(H_h^* + t_s^* \le z^* \le H_u^*)$

At $x^* = 0$,$0 \le y^* \le W_{ch}^*$

$$u_{c,in}^* = \frac{u_{c,in}}{u_{h,in}}, v^* = w^* = T_c^* = 0$$

$$p^*_{c,in} = \frac{p_{c,in}}{\rho\, u^2_{h,in}}$$

At $x^* = \frac{L}{D_h}$, $0 \le y^* \le W^*_{ch}$

$$\frac{\partial u^*}{\partial x^*} = \frac{\partial v^*}{\partial x^*} = \frac{\partial w^*}{\partial x^*} = \frac{\partial T^*_c}{\partial x^*} = 0$$

At $y^* = 0$, $0 \le x^* \le L^*$

$$u^* = v^* = w^* = \frac{\partial T^*_c}{\partial y^*} = 0$$

At $y^* = W^*_{ch}$, $0 \le x^* \le L^*$

$$u^* = v^* = w^* = \frac{\partial T^*_c}{\partial y^*} = 0$$

At $z^* = H^*_u$, $0 \le x^* \le L^*$, $0 \le y^* \le W^*_{ch}$

$$u^* = v^* = w^* = \frac{\partial T^*_c}{\partial z^*} = 0$$

Fluid -solid interface

At $z^* = H^*_h + t^*_s$, $0 \le x^* \le L^*$, $0 \le y^* \le W^*_{ch}$

$$u^* = v^* = w^* = 0$$

$$\frac{\partial T^*_c}{\partial z^*} = K_r \frac{\partial T^*_s}{\partial z^*}$$

Solid wall boundary conditions ($H^*_h \le z^* \le H^*_h + t^*_s$)

At $x^* = 0$, $0 \le y^* \le W^*_{ch}$

$$\frac{\partial T^*_s}{\partial x^*} = 0$$

At $x^* = \frac{L}{D_h}$, $0 \le y^* \le W^*_{ch}$

$$\frac{\partial T^*_s}{\partial x^*} = 0$$

At $y^* = 0$, $0 \le x^* \le L^*$

$$\frac{\partial T^*_s}{\partial y^*} = 0$$

At $y^* = W^*_{ch}$, $0 \le x^* \le L^*$

$$\frac{\partial T^*_s}{\partial y^*} = 0$$

At $z^* = H^*_h$, $0 \le x^* \le L^*$, $0 \le y^* \le W^*_{ch}$

$$\frac{\partial T_h^*}{\partial z^*} = K_r \frac{\partial T_s^*}{\partial z^*}$$

At $z^* = H_h^* + t_s^*, 0 \le x^* \le L^*$, $0 \le y^* \le W_{ch}^*$

$$\frac{\partial T_c^*}{\partial z^*} = K_r \frac{\partial T_s^*}{\partial z^*}$$

By solving the above governing equations using FORTRAN code the temperature distribution is determined in the hot, cold fluid and solid domains. From these distributions one can determine the axial heat conduction and exchanger effectiveness.

Heat exchanger effectiveness is the ratio of actual heat transfer to the maximum possible heat that can be transferred [10]:

$$\varepsilon = \frac{q}{q_{max.possible}}$$

(7)

where

$$q_{max} = C_{min}(T_{h,in} - T_{c,in})$$

(8)

and

$$q = C_c (T_{c,out} - T_{c,in}) = C_h (T_{h,in} - T_{h,out})$$

(9)

where $C_h = m_h c_h$ and $C_c = m_c c_c$

then the effectiveness is

$$\varepsilon = \frac{C_c(T_{c,out} - T_{c,in})}{C_{min}(T_{h,in} - T_{c,in})} = \frac{C_h(T_{h,in} - T_{h,out})}{C_{min}(T_{h,in} - T_{c,in})} \quad (10)$$

For the axial heat conduction in section *x* is

$$q_x'' = \left(k_s \frac{\bar{\bar{T}}_{s,i} - \bar{\bar{T}}_{s,i+1}}{\Delta x} \right)_x$$

(11)

where, $\bar{\bar{T}}_{s,i}$ is the average solid temperature, $\bar{\bar{T}}_{s,i+1}$ at the next section and Δ the distance between the two sections as shown in figure 3.

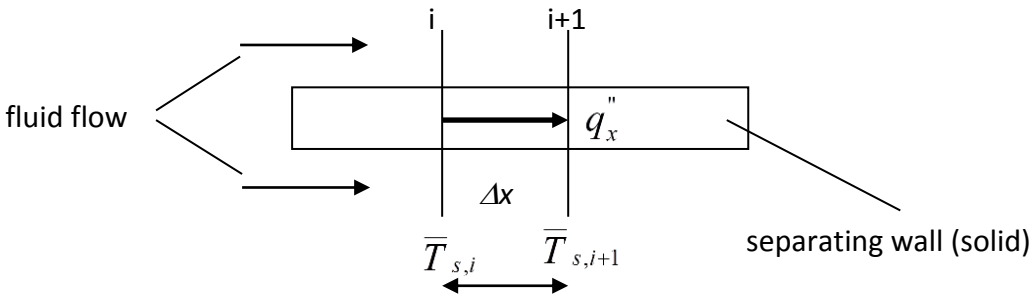

Figure 3 Schematic of separating wall.

2. NUMERICAL SOLUTION

Finite-volume method adopted which is applied to the integral form of the governing equations over the control volume (cell) as shown in figure 4. A cell containing node ***P*** has four neighbouring nodes identified as west, east, south and north nodes ***(W, E, S, N).*** The notation, ***w, e, s and n*** are used to refer to the west, east, south and north cell faces respectively. The methods which depend on this technique such central differencing scheme, upwind differencing scheme, hybrid differencing scheme and others. However, the present work is adopted on the hybrid differencing scheme with staggered grids arrangement to solve pressure-velocity coupling which associated with present problem and SIMPLE algorithm is used as listed in [11].

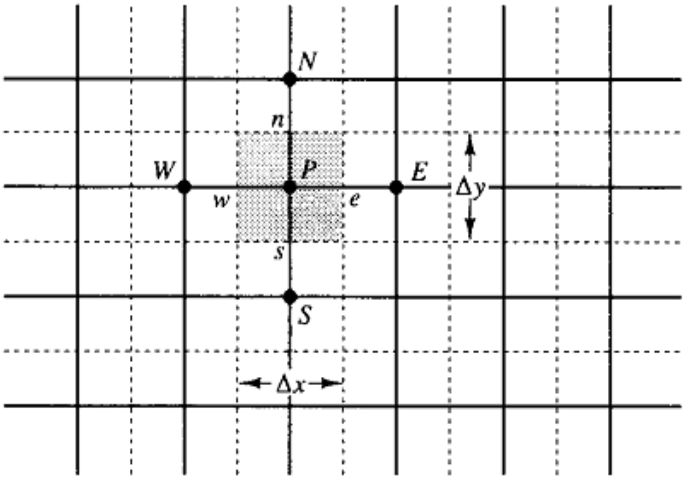

Figure 4 A cells in two-dimensional and neighbouring nods taken from [11].

SIMPLE algorithm is implicit method are preferred for steady state and slow transient flows, because they have less stringent time steps restrictions as compared the explicit schemes. Many solutions methods for steady incompressible flows use a

pressure (or pressure-correction) equation to solve pressure-velocity coupling [12]. Discretized *u*-component equation (2) is written in the following form [11]

$$a^*_{(i,J,K)}u^*_{i(i,J,K)} = \sum a^*_{nb}u^*_{i(nb)} + \left(p^*_{i(I-1)} - p^*_{i(I)}\right)A^*_x$$

(12)

where, $\sum a^*_{nb}u^*_{i(nb)}$ is the summation of neighboring components for *u*-component and the subscript *i* refer to cold or hot fluid. The values of coefficients $a^*_{(i,J,K)}$ and a^*_{nb} in equation (12) are calculated by using the hybrid method. However, to initiate the SIMPLE calculation process a pressure field $p^{*\bullet}_i$ is guessed. Discretised momentum equation (2) is solved using the guessed pressure field to yield velocity component $u^{*\bullet}_i$ as follows [11]

$$a^*_{(i,J,K)}u^{*\bullet}_{i(i,J,K)} = \sum a^*_{nb}u^{*\bullet}_{i(nb)} + \left(p^{*\bullet}_{i(I-1)} - p^{*\bullet}_{i(I)}\right)A^*_x$$

(13)

Now we defined the correction $p^{*''}_i$ as the difference between the correct pressure field p^*_i and the guessed pressure field $p^{*\bullet}_i$, so that

$$p^*_i = p^{*\bullet}_i + p^{*''}_i$$

(14)

Similarly we defined velocity correction $u^{*''}_i$ to relate the correct velocity u^*_i to the guessed velocity solution $u^{*\bullet}_i$

$$u^*_i = u^{*\bullet}_i + u^{*''}_i$$

(15)

Subtraction of equation (13) from equation (12) gives

$$a^*_{(i,J,K)}\left(u^*_{i(i,J,K)} - u^{*\bullet}_{i(i,J,K)}\right) = \sum a^*_{nb}\left(u^*_{i(nb)} - u^{*\bullet}_{i(nb)}\right) + \left[\left(p^*_{i(I-1)} - p^{*\bullet}_{i(I-1)}\right) - \left(p^*_{i(I)} - p^{*\bullet}_{i(I)}\right)\right]A^*_x$$

(16)

Using correction formulae (14) and (15), the equation (16) may be rewritten as follows

$$a^*_{(i,J,K)}u^{*''}_{i(i,J,K)} = \sum a^*_{nb}u^{*''}_{i(nb)} + \left(p^{*''}_{i(I-1)} - p^{*''}_{i(I)}\right)A^*_x$$

(17)

At this point an approximation is introduced: $\sum a^*_{nb} u^*_{i(nb)}$ is dropped to simplify equation (17) for velocity correction. Omission of that term is the main approximation of the SIMPLE [11]. We obtain

$$u^{*"}_{i(i,J,K)} = d^*_{(i,J,K)} \left(p^{*"}_{i(I-1)} - p^{*"}_{i(I)} \right) \quad (18)$$

where $d^*_{(i,J,K)} = A^*_x / a^*_{(i,J,K)}$. Equation (18) describe the correction to be applied to *u*-component through equation (15), which gives

$$u^*_{i(i,J,K)} = u^{*\bullet}_{i(i,J,K)} + d^*_{(i,J,K)} \left(p^{*"}_{i(I-1)} - p^{*"}_{i(I)} \right) \quad (19)$$

Similar expression exist for $u^*_{i(i+1,J,K)}$ [11]

$$u^*_{i(i+1,J,K)} = u^{*\bullet}_{i(i+1,J,K)} + d^*_{(i+1,J,K)} \left(p^{*"}_{i(I)} - p^{*"}_{i(I+1)} \right) \quad (20)$$

where $d^*_{(i+1,J,K)} = A^*_x / a^*_{(i+1,J,K)}$.

The SIMPLE algorithm gives a method of calculating pressure and velocity. The method is iterative and when other scalars like present problem are coupled to the momentum equations, the calculations needs to be done sequentially [11]. The sequence of operations in a FORTRAN procedure which employs the SIMPLE algorithm is given in figure 5.

In figure 5, the correct pressure field p^*_i and correct velocity field u^*_i, v^*_i and w^*_i for two channels are obtained separately. There is no coupling between the two channels for these variables as shown in the steps 1, 2 and 3. The previous steps represent the solution for pressure-velocity coupling problem (pressure-correction method). While, the last step represent the solution for convection-conduction conjugate heat transfer problem (simultaneously solution for the temperatures), where

$$b^*_{(I,J,K)} = \left(u^{*\bullet}_{(i,J,K)} - u^{*\bullet}_{(i+1,J,K)} \right) A^*_x + \left(v^*_{(I,j,K)} - v^*_{(I,j+1,K)} \right) A^*_y + \left(w^*_{(I,J,k)} - w^*_{(I,J,k+1)} \right) A^*_z \quad (21)$$

the A^*_x, A^*_y *and* A^*_z represents the control volume face area in *x*, *y* and *z* directions.

The pressure field p^*_i is obtained by solving the pressure correction $p^{*"}_i$ equation. It is common practice to fix the absolute pressure at one inlet node and set the

pressure correction to zero ($p_i^{*"}$ =0) at that node. Having specified a reference value, the absolute pressure field inside the domain can now be obtained [11].

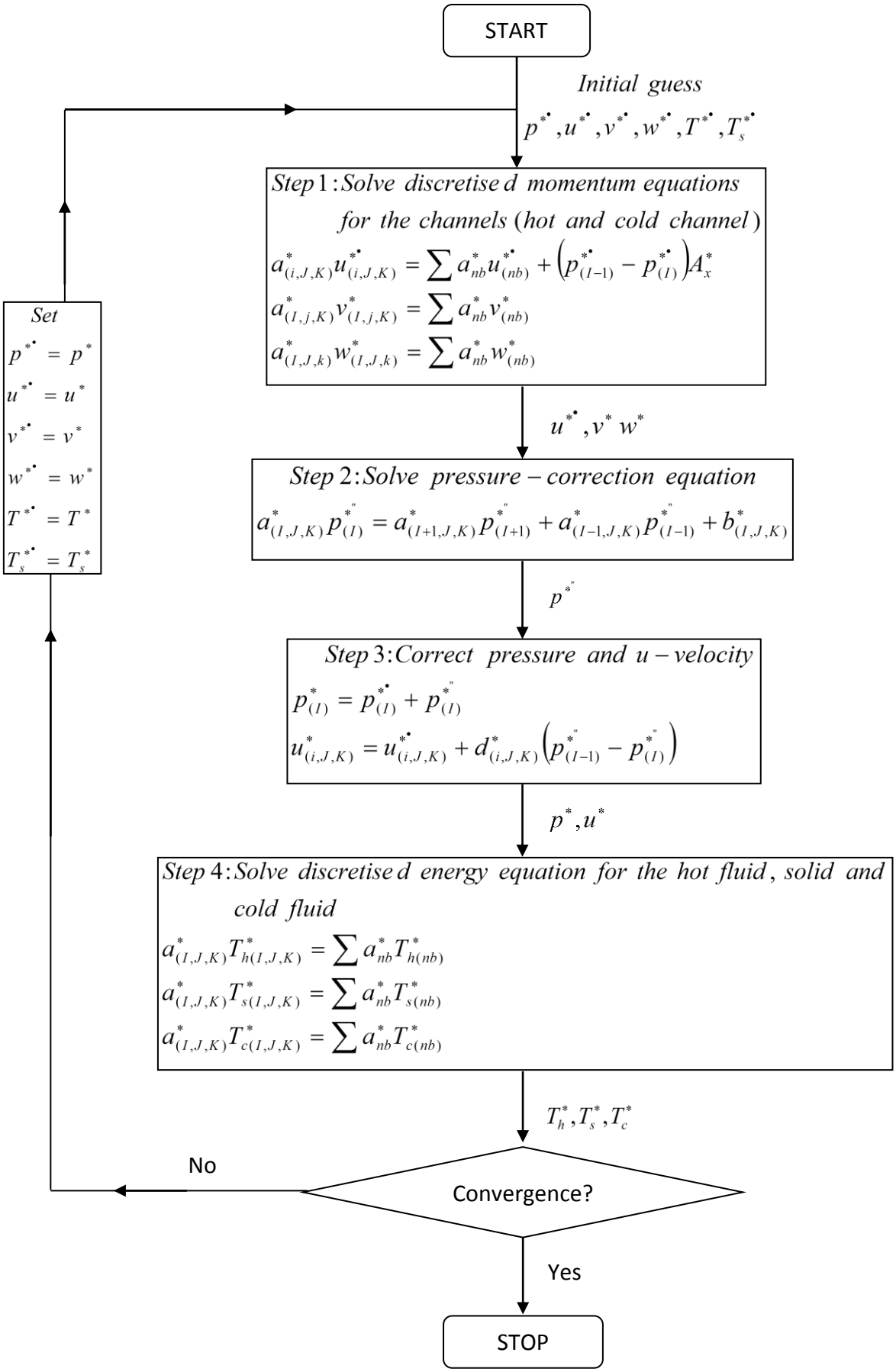

Figure 5 The SIMPLE algorithm.

4. RESULTS

In this section, the results about the influences of Reynolds number Re, thermal conductivity ratio *Kr*, aspect ratio α and channel volume on the local and average axial heat conduction ($q_x^{"}$ and $q_{average}^{"}$) and the effectiveness to average axial heat conduction ratio $\varepsilon/q_{average}^{"}$ in parallel flow rectangular microchannel heat exchanger for different conditions is studied. Study the ratio $\varepsilon/q_{average}^{"}$ to indicate the effect of axial conduction on the exchanger effectiveness, but before that it's necessary to study the $q_{average}^{"}$ and ε each separately.

In order to verify the accuracy of present numerical model, a comparison is made between the results of present model for rectangular microchannel heat exchanger and that in literature. Figure 6 represents a comparison for dimensionless mean temperature for hot and cold fluids in rectangular microchannel heat exchanger for present numerical model and that of [7]. The dimensionless mean temperature $T_m^* = \dfrac{T_i - T_{c,in}}{T_{h,in} - T_{c,in}}$ is presented in this figure for the hot and cold fluids in rectangular microchannel heat exchanger against the dimensionless axial distance $x^+ = \dfrac{x}{D_h \,\mathrm{Re}\,\mathrm{Pr}}$ at Re=100, Pr=0.7 and $\dfrac{k_w D_h}{k_s t_s}$=100. The figure indicates for both results that dimensionless mean temperature converge to each other toward fully developed region, this refer to that the heat is transferred from hot to cold fluid. Also, the figure shows that there is a good agreement between the present numerical results and the results of [7], the maximum percentage error was ±2.01%.

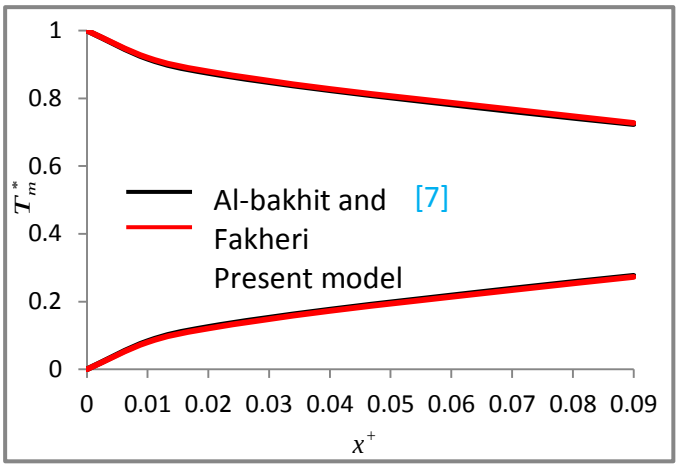

Figure 6 Comparison of the dimensionless mean temperature of the hot and cold fluids.

Figure 7 shows the longitudinal variation of the axial heat conduction $q_x^{"}$ with axial distance *x* for different thermal conductivity ratios K_r at t_s=50μm, Re=200 and α=1. For all thermal conductivity ratios, the figure indicates that the $q_x^{"}$ is high in entrance region and decrease toward fully developed region due to the effect of entrance. Also, the figure shows that the $q_x^{"}$ increases with K_r, due to that the heat transferred from hot fluid to cold fluid increase with increase K_r.

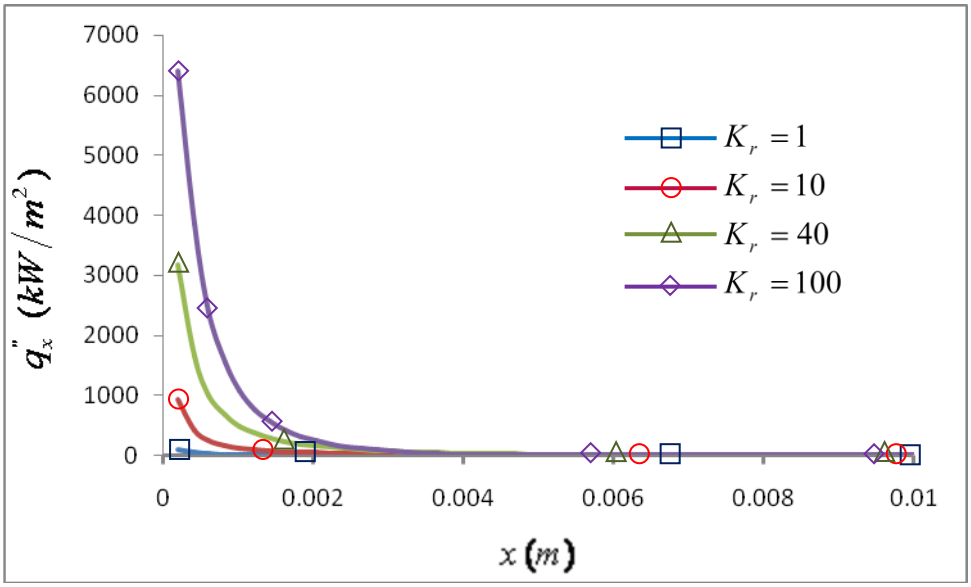

Figure 7 Longitudinal variation of the axial heat conduction with axial distance *x* for different values of K_r.

Figure 8 shows the variation of longitudinal axial heat conduction in the separating wall $q_x^{"}$ with axial distance *x* for different Reynolds numbers at K_r=1, t_s=50μm and α=1. This figure shows that the $q_x^{"}$ for all Reynolds number is high in the entrance region, due to the effect entrance region since maximum heat transfer accrued in the entrance region and as a result maximum value of axial heat conduction is also created in this region. As the heat transfer process increased with increasing Re and so, the fraction of axial conduction increased. Also, as $q_x^{"}$ increased with Re, the heat transferred from hot fluid to cold fluid decrease and both fluids and separating wall are still conserve heat and there is no sufficient time for heat exchange at high Re.

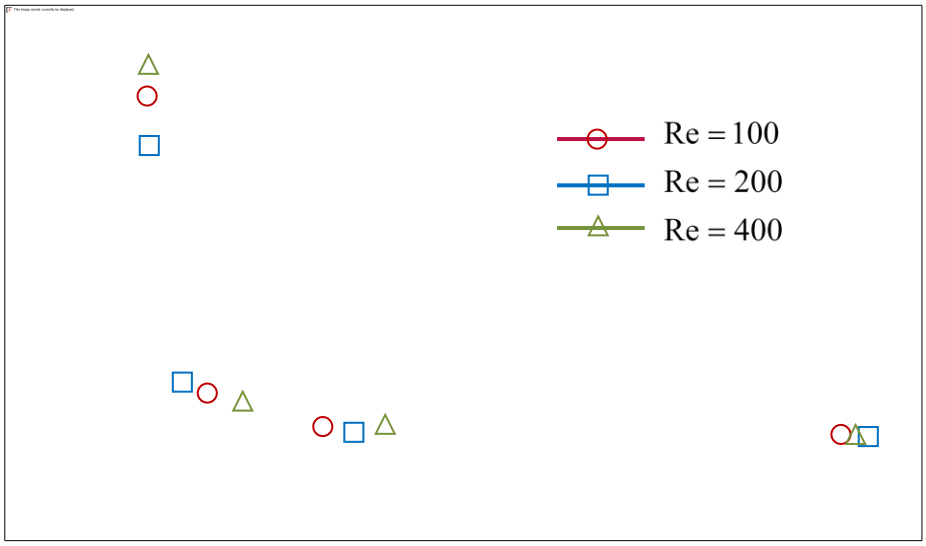

Figure 8 Longitudinal variation of the axial heat conduction with axial distance *x* for different Reynolds numbers.

Figure 9 illustrates the variation of average axial heat conduction $q_{average}^{"}$ with Reynolds number Re for different aspect ratios at K_r=1 and t_s=50μm. For all α, the $q_{average}^{"}$increases with Re for the raised reason is the same in pervious figure. Also, $q_{average}^{"}$ decrease when α decrease, this is refer to the cowing of heat transferred between both fluids overcome on the axial conduction in small α and vice versa.

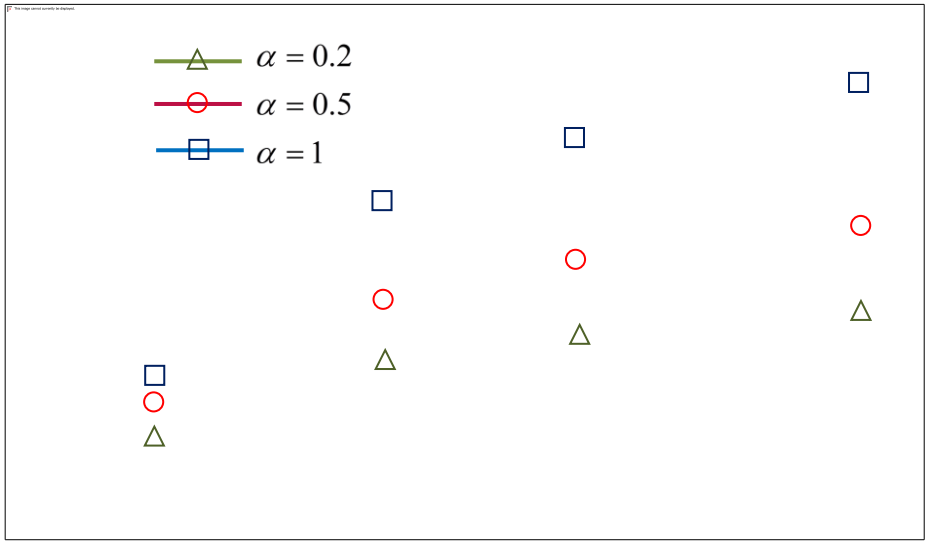

Figure 9 Variation of the average axial heat conduction with Reynolds number for different aspect ratios.

Figure 10 shows the variation of the average axial heat conduction $q''_{average}$ with aspect ratio α for different Reynolds numbers at K_r=1 and t_s=50μm. For all Re, $q''_{average}$increases with α, this is because any increasing of fluid in the channel leads to increasing the heat remaining in the fluids and separating wall and then the $q''_{average}$ increase. As illustrated in previous figures $q''_{average}$ increase with Re.

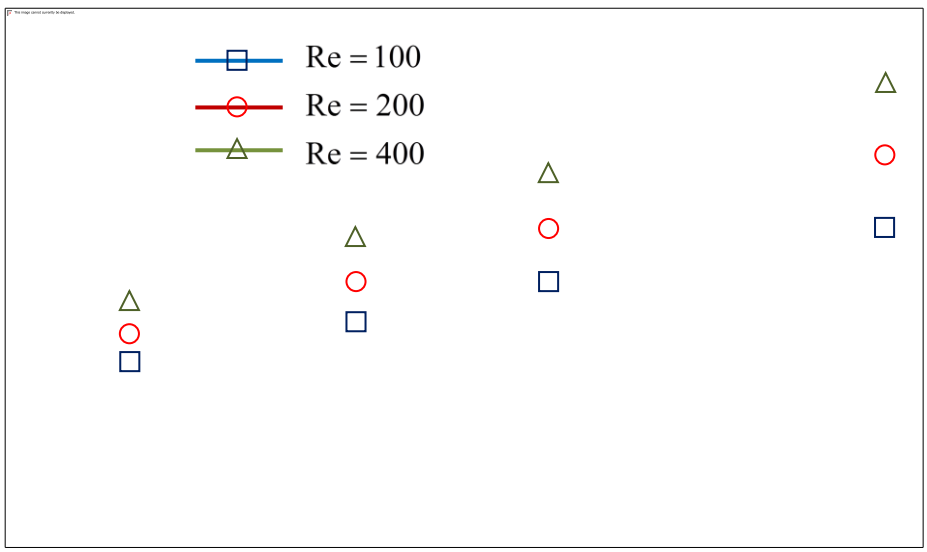

Figure 10 Variation of the average axial heat conduction with aspect ratio for different Reynolds.

Figure 11 shows the variation of the average axial heat conduction $q''_{average}$ with thermal conductivity ratio K_r for different Reynolds numbers at t_s=50μm and α=1

and. For all Re, $q''_{average}$ increases with K_r, this is because that more heat transferred between the two fluids through the separating wall at high K_r, and this lead to increase the axial heat conduction.

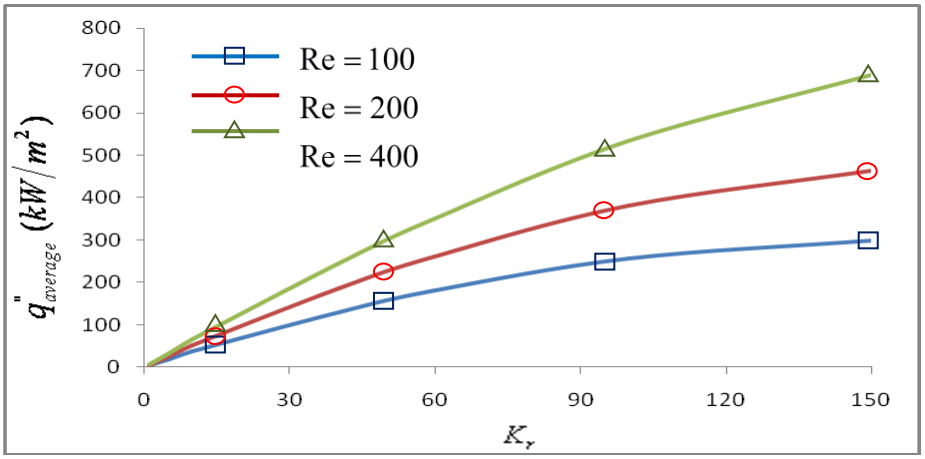

Figure 11 Variation of the average axial heat conduction with thermal conductivity ratio for different Reynolds numbers.

Figure 12 shows the variation of the average axial heat conduction $q''_{average}$ in axial direction with aspect ratio α for different thermal conductivity ratios at Re=200 and t_s =50μm. For all K_r, the $q''_{average}$increases with α (due to increasing of fluid in the channel lead to increasing the heat remaining in the fluids and separating wall). Also, $q''_{average}$ increases with K_r because the heat transferred through the separating wall increases.

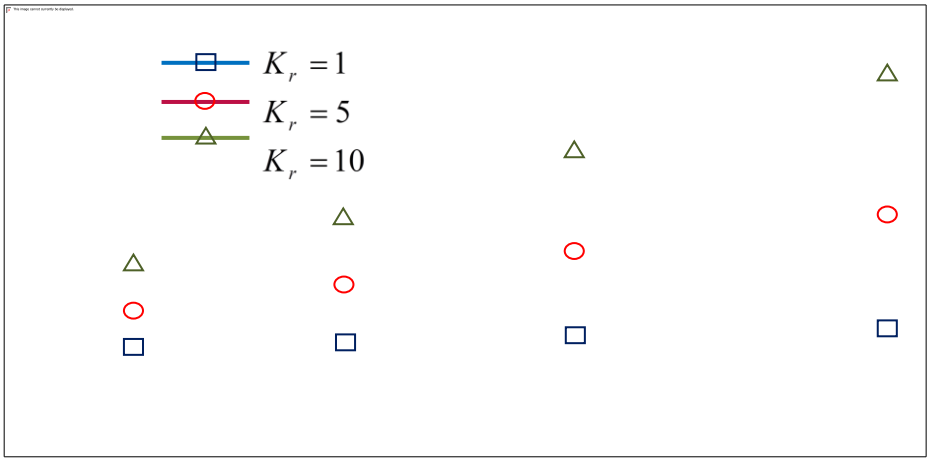

Figure 12 Variation of the average axial heat conduction with aspect ratio for different thermal conductivity ratios.

Figure 13 clarifies the variation of the average heat conduction in axial direction $q''_{average}$ with channel volume for different Reynolds number at K_r=1 and t_s=50μm. For all Re, $q''_{average}$ increases with channel volume in which lead to increasing the heat remaining in the fluid and separating wall and then the $q''_{average}$ increase.

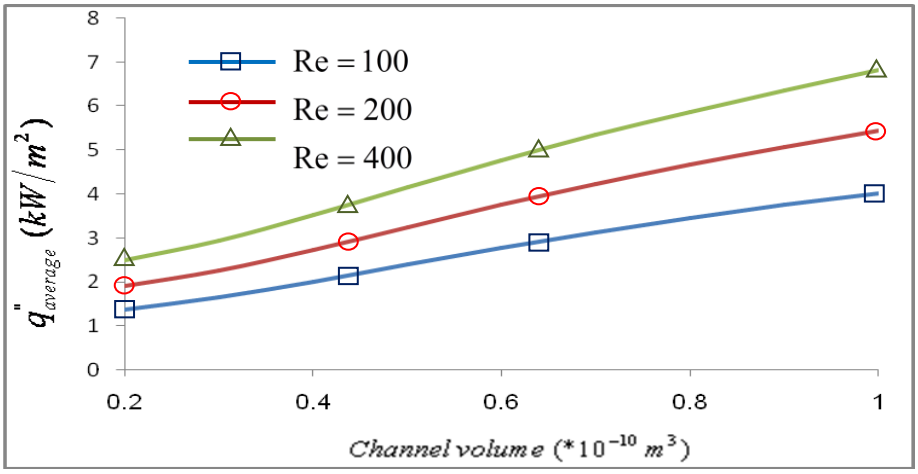

Figure 13 Variation of the average axial heat conduction with channel volume for different Reynolds numbers.

Figure 14 shows the variation of the average heat conduction in axial direction $q''_{average}$ with channel volume for different thermal conductivity ratios at Re=200 and t_s =50μm. For all K_r, $q''_{average}$increases with channel volume. Also, $q''_{average}$ increase with K_r in which heat transferred between the two fluids through the separating wall increases.

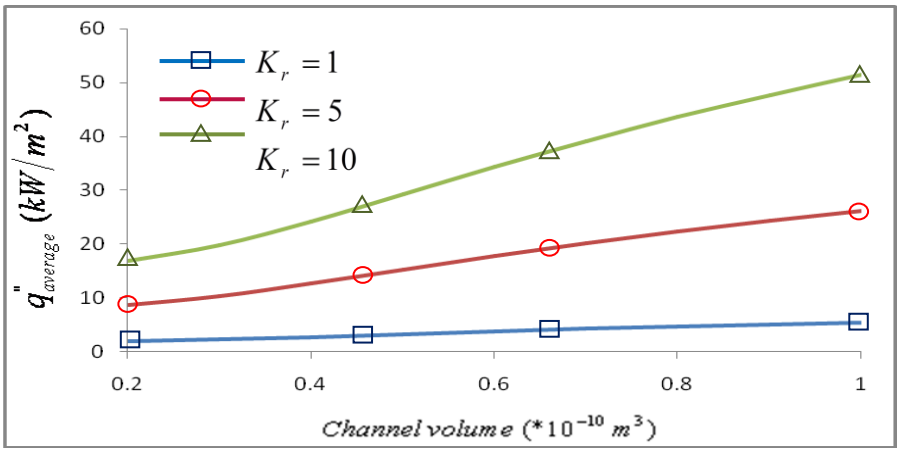

Figure 14 Variation of the average axial heat conduction with channel volume for different thermal conductivity ratios.

Figure 15 illustrates the variation of the microchannel heat exchanger effectiveness ε with Reynolds number for different aspect ratios at K_r=1 and t_s=50μm. The effectiveness decrease with Re for all α, this is due to that the amount fluid increases when Re increase and then ΔT decrease. On other hand, the axial conduction in the solid also increase with Re as before. The effectiveness at low Re is seems to be converge to each other but the difference increase at high Re, this refer to low Re (there is sufficient time to heat exchange and the effect of axial conduction is small in all cases and vice versa). On other hand, ε is increased at low α, and at α=0.2 gives best ε because the axial conduction decrease and heat transferred increase.

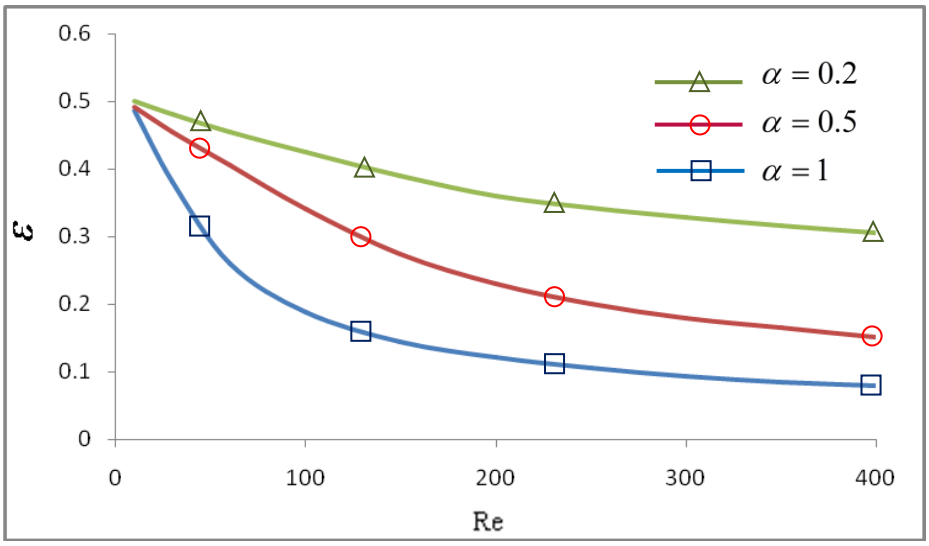

Figure 15 Variation of the microchannel heat exchanger effectiveness with Reynolds number for different aspect ratios.

Figure 16 illustrates the variation of microchannel heat exchanger effectiveness ε with thermal conductivity ratio K_r at α=1 and t_s=50μm for different Reynolds numbers. For all Re, the effectiveness increases with increase K_r and more heat transferred from hot to cold fluid in spite of the axial conduction, also increases with K_r, but the heat transfer overcome on it. Also, the figure indicates that the ε is higher at Re=100.

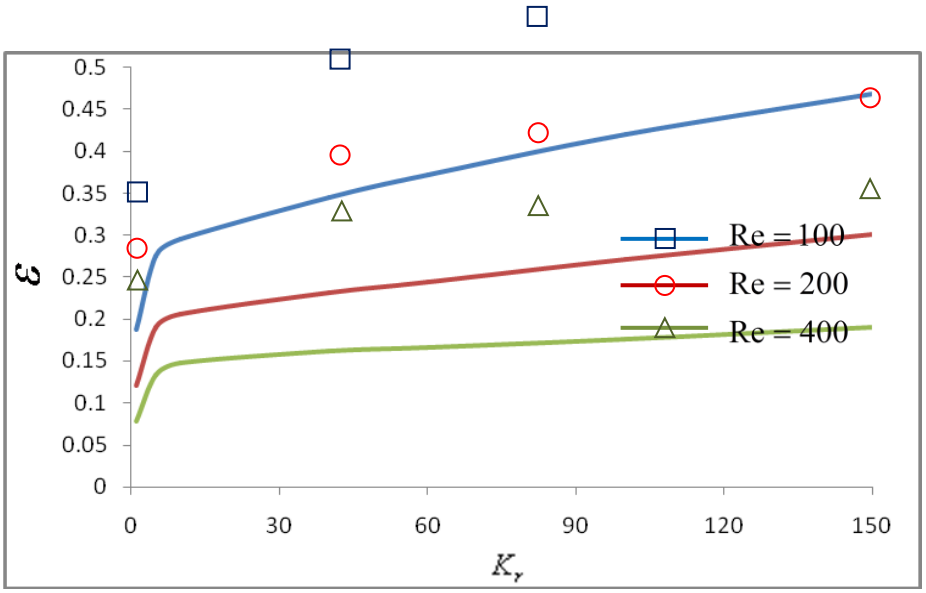

Figure 16 Variation of the heat exchanger effectiveness with thermal conductivity ratios for different Reynolds numbers.

Figure 17 shows the variation of the microchannel heat exchanger effectiveness ε with aspect ratio α for different Reynolds numbers at K_r=1 and t_s=50μm. For all Re, the figure clarifies that the effectiveness decreases with α. This is due to the amount of fluid increases when α increase and then ΔT decrease. On other hand, the axial conduction in the solid also increases with α as shown before. Also, the figure shows that, the effectiveness at Re=100 is more than the others for same reason.

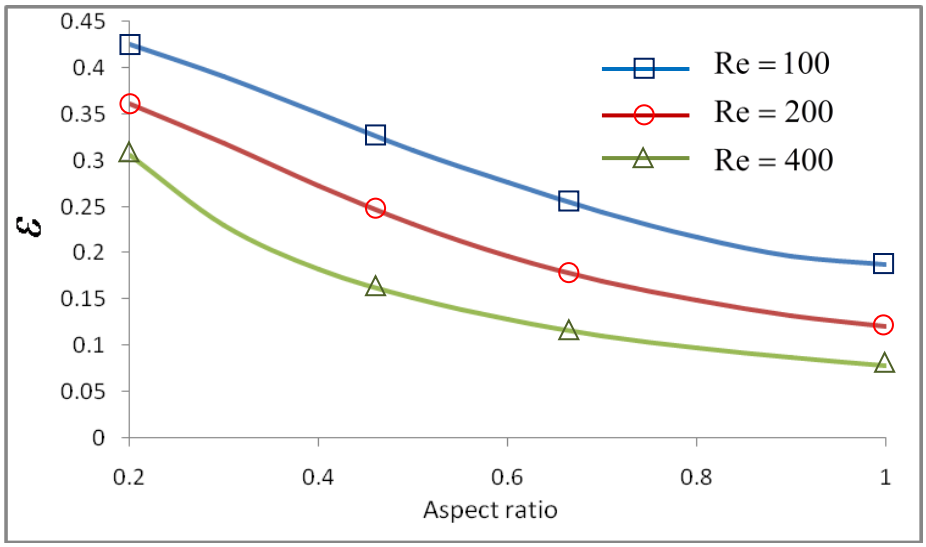

Figure 17 Variation of the heat exchanger effectiveness with aspect ratio for different Reynolds numbers.

Figure 18 illustrates the variation of the microchannel heat exchanger effectiveness ε with channel volume for different thermal conductivity ratios at Re=200 and t_s=50μm. For all K_r, the effectiveness decreases with channel volume. This is due to the amount of fluid increases when channel volume increase and then ΔT decrease.

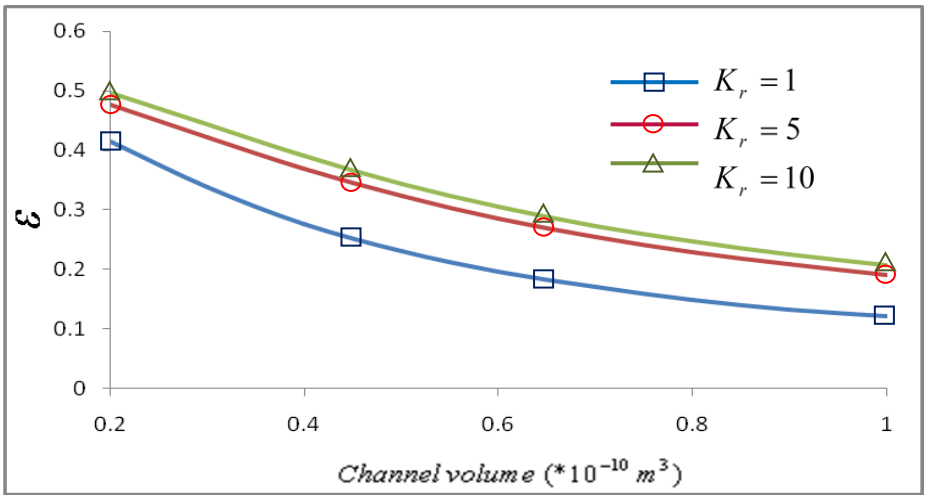

Figure 18 Variation of the heat exchanger effectiveness with channel volume for different thermal conductivity ratios.

Figure 19 shows the variation of the microchannel heat exchanger effectiveness ε with thermal conductivity ratio K_r for different aspect ratios at Re=200 and t_s=50μm. The ε increases with K_r this is due to increasing the conductivity of the separating wall and more heat is transferred in this case in spite of the axial conduction also increases, but the heat transferred between the two fluids overcome on it. Also, the ε at α=0.2 more than the others, this is because the amount of fluid decreases when the α decrease. For α=0.2 the effectiveness increase with K_r but normally not above ε=0.5 for nearly K_r=10 then the effectiveness will be constant.

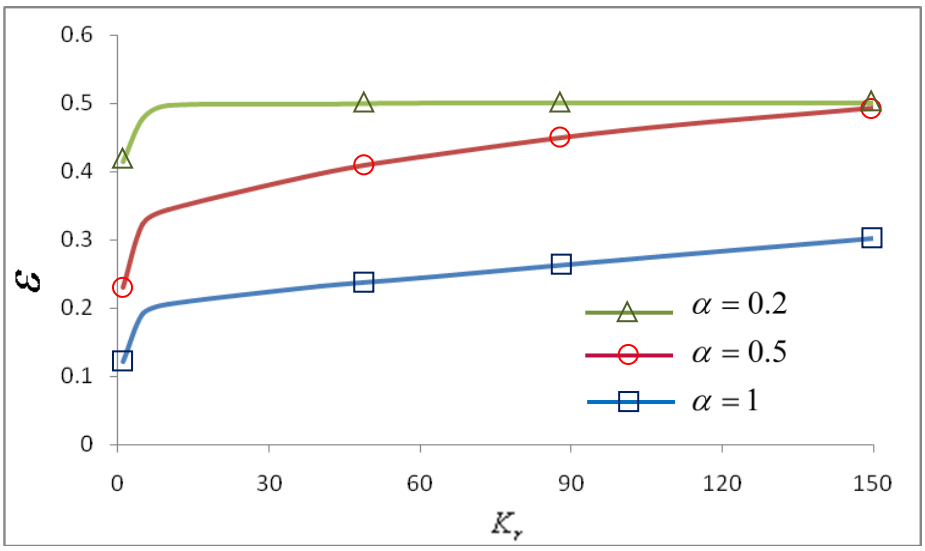

Figure 19 Variation of the heat exchanger effectiveness with thermal conductivity ratio for different aspect ratios.

Figure 20 illustrates the variation of the microchannel heat exchanger effectiveness to average axial conduction ratio $\varepsilon/q''_{average}$ with Reynolds number for different aspect ratios at K_r=1 and t_s=50μm. For all α, $\varepsilon/q''_{average}$ decreases with Re, this is because the effectiveness decreases and the axial conduction in the solid increases with Re. For α=0.2 gives the best value of $\varepsilon/q''_{average}$ especially at low Re due to both the ε increase and $q''_{average}$ decrease at small Re.

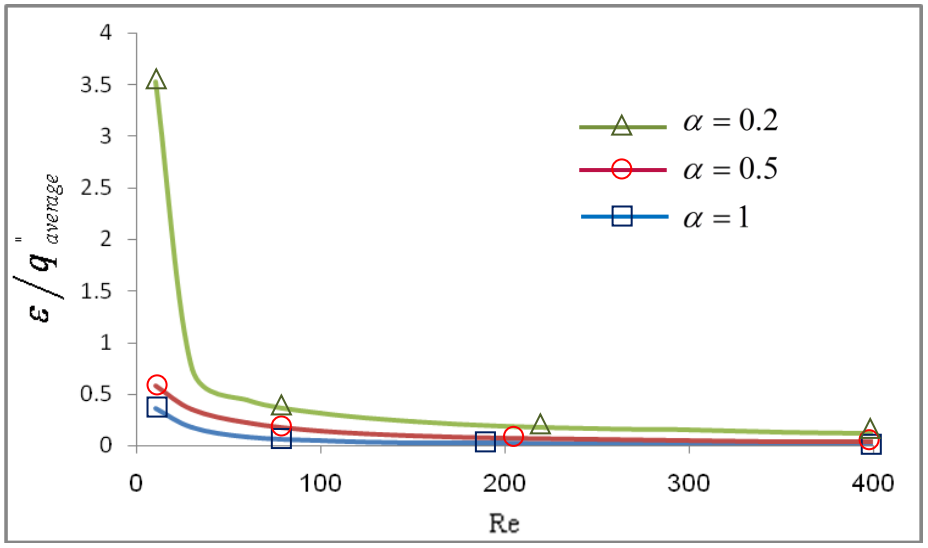

Figure 20 Variation of the microchannel heat exchanger effectiveness to average axial heat conduction ratio with Reynolds number for different aspect ratios.

Figure 21 shows the variation of the microchannel heat exchanger effectiveness to average axial heat conduction ratio $\varepsilon/q''_{average}$ with thermal conductivity ratio for different aspect ratios at Re=200 and t_s =50μm. $\varepsilon/q''_{average}$ decreases with K_r, this is due to the $q''_{average}$ increases with K_r, in spite of that ε also increase in this case, but the increasing in $q''_{average}$ is more than that for the ε. Also, at α=0.2 gives the best value of $\varepsilon/q''_{average}$.

\

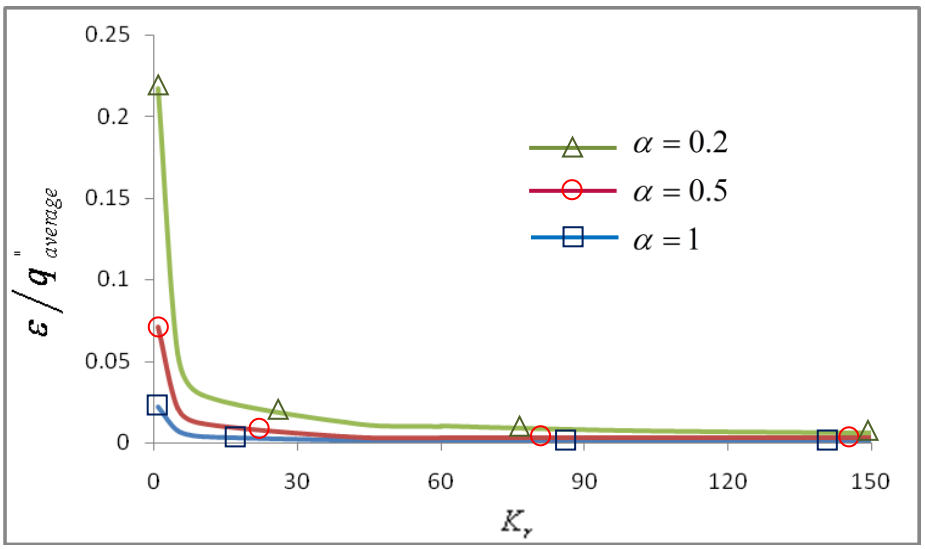

Figure 21 Variation of the microchannel heat exchanger effectiveness to average axial heat conduction ratio with thermal conductivity ratio for different aspect ratios.

Figure 22 illustrates the variation of the microchannel heat exchanger effectiveness to average axial heat conduction ratio $\varepsilon/q''_{average}$ with thermal conductivity ratio K_r for different Reynolds numbers at α=1 and t_s =50μm. For all Re, as expected $\varepsilon/q''_{average}$ is decrease with K_r. Also, $\varepsilon/q''_{average}$ decrease with Re, since amount of fluid increases when Re increase then ΔT and ε decreases. On other hand, the axial conduction in the solid also increase with Re.

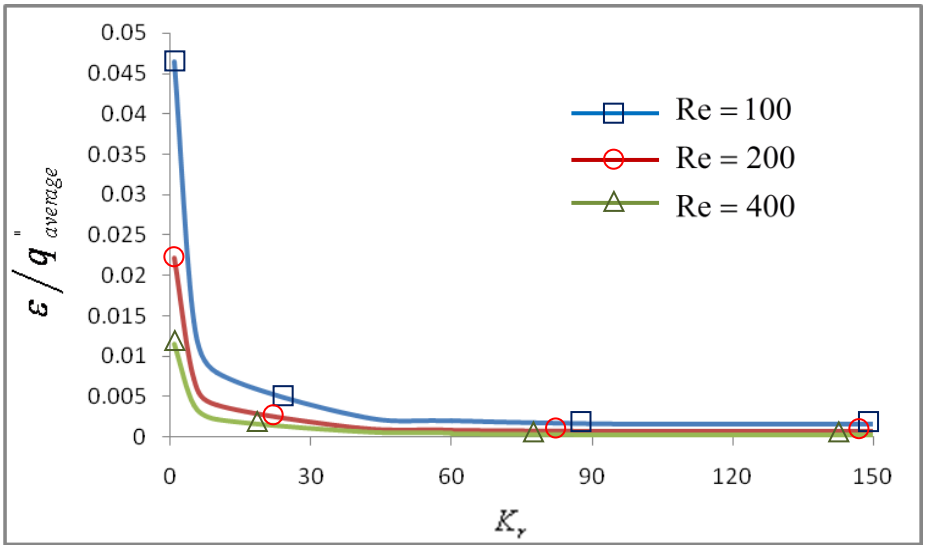

Figure 22 Variation of the microchannel heat exchanger effectiveness to average axial heat conduction ratio with thermal conductivity ratio for different Reynolds numbers.

Figure 23 shows the variation of the microchannel heat exchanger effectiveness to average axial heat conduction ratio $\varepsilon/q''_{average}$ with channel volume for different Reynolds numbers at K_r =1 and t_s =50μm. For all Re, $\varepsilon/q''_{average}$ decreases with channel volume this is due to the effectiveness decreases with channel volume and the axial conduction in the solid increases with channel volume.

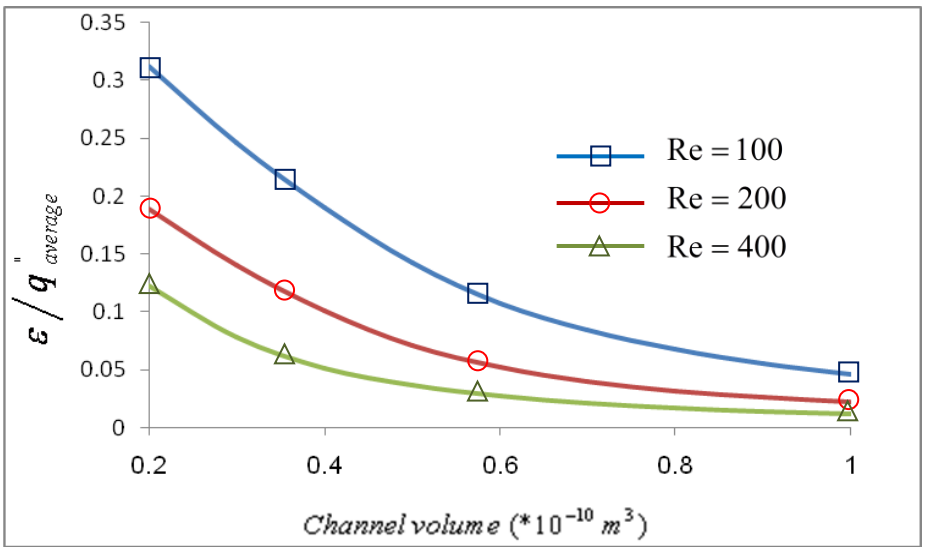

Figure 23 Variation of the microchannel heat exchanger effectiveness to average axial heat conduction ratio with channel volume for different Reynolds numbers.

Figure 24 shows the variation of the microchannel heat exchanger effectiveness to average axial heat conduction ratio $\varepsilon/q''_{average}$ with channel volume for different thermal conductivity ratios at Re=200 and t_s =50μm. It seen from this figure the best ratio of $\varepsilon/q''_{average}$ is at K_r =1.

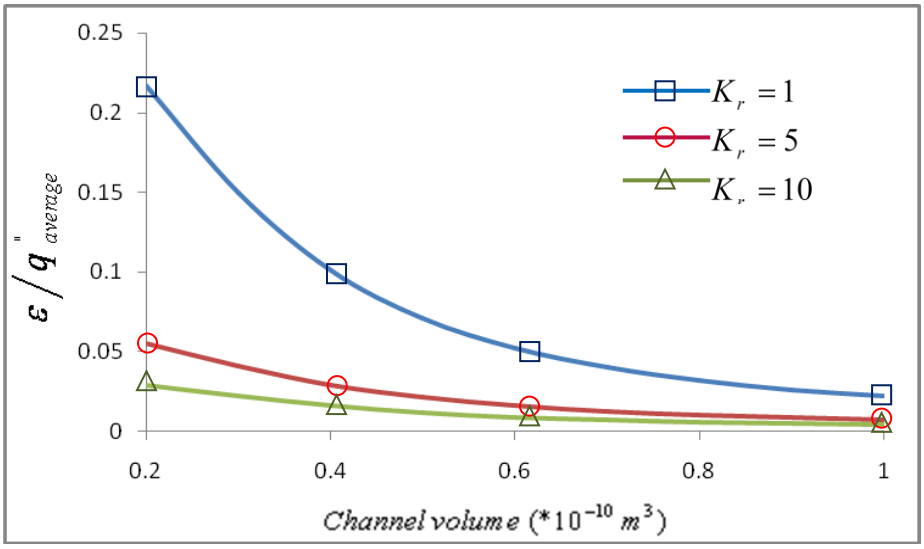

Figure 24 Variation of the microchannel heat exchanger effectiveness to average axial heat conduction ratio with channel volume for different thermal conductivity ratios.

5. CONCLUSIONS

The effects of axial heat conduction in rectangular microchannel heat exchanger with parallel flow was studied numerically through the microchannel heat exchanger effectiveness to average axial conduction ratio $\varepsilon/q''_{average}$ considering thermally and hydradynamically developing flow conditions. The Navier–Stokes and energy equations are solved in a three-dimensional domain using the finite-volume method with FORTRAN code. However, from the results obtained the following conclusions can be drawn:

- The parameters affect the axial conduction and the effectiveness in rectangular microchannel heat exchanger are: thermal conductivity ratio K_r, Reynolds number Re, aspect ratio α and channel volume.
- Increasing of the thermal conductivity ratio K_r, Reynolds number Re, aspect ratio α and channel volume each separately lead to increase of the axial heat conduction and vice versa.

- The microchannel heat exchanger effectiveness ε increase with increasing thermal conductivity ratio K_r while decrease with increasing Reynolds number Re, aspect ratio α and channel volume each separately.
- The effect of the axial heat conduction is reflected in the microchannel heat exchanger effectiveness to average axial heat conduction ratio $\varepsilon/q''_{average}$ which decrease with increasing thermal conductivity ratio K_r in spite of the effectiveness increase due to the axial heat conduction effect, and increasing of K_r will not enhance the effectiveness, and $\varepsilon/q''_{average}$ decreases with Reynolds number Re, aspect ratio α and channel volume each separately.

REFERENCES

[1] M.A. Al-Nimr, M. Maqableh, A.F. Khadrawi, S.A. Ammourah," Fully developed thermal behaviors for parallel flow microchannel heat exchanger", International Communications in Heat and Mass Transfer, Vol. 36, pp. 385-390, 2009.

[2] B. Mathew, H. Hegab, "Application of effectiveness-NTU relationship to parallel flow microchannel heat exchangers subjected to external heat transfer", International Journal of Thermal Sciences, Vol. 30, pp.1-10, 2009.

[3] H. Al-bakhit and A. Fakheri, "A hybrid Approach for Full Numerical Simulation of Heat Exchangers", ASME Heat Transfer Summer Conference, San Francisco, CA, USA, pp. 17-22, 2005.

[4]M.A. Al-Nimr, M. Maqableh, A.F. Khadrawi, S.A. Ammourah," Fully developed thermal behaviors for parallel flow microchannel heat exchanger", International Communications in Heat and Mass Transfer, Vol. 36, pp. 385-390, 2009.

[5] Yin X. and Bau H. H., "Axial Conduction Effect Performance of Micro Heat Exchangers", ASME Winter Annual Meeting, New Orleans, Louisiana, USA, November 28-December 3, 1992.

[6] Stief T., Langer O. U. and Schubert K., "Numerical Investigation of Optimal Heat Conductivity in Micro Heat Exchangers", Chem Engineering Technology, Vol. 22, pp. 297-303, 1999.

[7] Hussien Al-bakhit and Ahmad Fakheri, "Numerical Simulation of Heat Transfer in Simultaneously Developing Flows in Parallel Rectangular Ducts", Applied Thermal Engineering, Vol. 26, pp. 596-603, (2006).

[8] Mushtaq I. Hasan, "Numerical Simulation of Counter Flow Microchannel Heat Exchanger with Different Channel Geometries and Working Fluid", PhD Thesis, Mechanical Engineering Department, Collage of Engineering, Basrah University, 2009.

[9] **Hyder M. Hasan, "** Numerical Simulation of Parallel Flow Microchannel Heat Exchanger with Isosceles Right Triangular Geometry", MSc Thesis, Engineering Collage, University of Basrah, 2009.

[10] Sean Ashman and Satish G. Kandlikar, "A review of Manufacturing Processes for Microchannel Heat Exchanger Fabrication", Proceedings of ICNMM2006, Fourth International Conference on Nanochannels, Microchannels and Minichannels, Limerick, Ireland, June 19-21 (2006).

[11] H. K. Versteeg and W. Malalasekera, "An introduction to Computational Fluid Dynamics-The Finite-Volume Method", Longman, (1995).

[12] Amit S. Kulkarni, "Effects of Surface Roughness in Microchannel Flows", MSc Thesis, University of Florida, (2004).

ESTIMATING SOIL LOSS BY WATER EROSION

1- Dr. Ahmed. M. H. Al-Kadhimi, 2- Zainb. A. A. Al-Saad,

3- Fatima A. A. Al-Badran

Department of Civil Engineering, College of Engineering, University of Basrah, Iraq.

ABSTRACT:

The study is focused on the estimation of rate of soil erosion, using the Universal Soil Loss Equation(USLE), for the embankment of Al-Garma Bridge in Basrah, Iraq. The soil erosion is estimated for the zone of average slope in the study area. The factors considered are rainfall, intensity of rainfall, type of soil, slope length, slope steepness, land use classification, and the existing of soil conservation practices. Detailed analysis of soil samples were done to asses the texture, structure, permeability and organic matter content of the soil samples of the embankment of the Al-Garma Bridge. The average annual erosivity index is obtained as (124.99(MJ. mm/(ha.h))) and the annual average soil erosion rate is estimated as (61.5 t/ha/year).

الخلاصة

هذه الدراسة ركزت على تخمين مقدار تآكل التربة ، باستخدام المعادلة الجامعة للتآكل للتعلية الترابية لجسر الكرمة الواقع في مدينة البصرة في العراق. المعاملات التي أخذت بنظر الاعتبار هي المطر ، الشدة المطرية ،نوع التربة ، طول الميل ،انحدار الميل، استخدامات الأرض، وجود استراتيجيا معينة لحفظ التربة من التآكل. تحاليل مفصلة للنماذج التي أخذت من موقع الدراسة لتحديد البناء والتركيب والنفاذية وتحديد نسبة المواد العضوية لهذه النماذج. تآكل التربة خمن للمنطقة الموجودة في الوسط أي في وسط الميل للتعلية الترابية. وجد ان المعدل السنوي لمعامل المطر هو 124.99 وان معدل التآكل السنوي لموقع الدراسة هو (61.5 طن/هكتار/سنه).

Keywords: soil erosion, Universal Soil Loss Equation USLE.

1-INTRODUCTION:

Soil erosion results from the detachment, the transportation and sedimentation of the soil particles. Factors such as wind characteristics and similar climatic conditions play paramount roles in the disintegration of soil structure. Rain as an external factor plays the most important role and, of soil factors, erodibility phenomenon is importance (Giovanini et al.,2001).

It is useful to make an estimate of how fast the soil is being eroded, before implementing any conservation strategies. Thus methods of predicting the soil loss under a wide range of conditions are required. Erosion models are necessary tools to

predict excessive soil loss and to help in the implementation of an erosion control strategy. As part of literature review, a wide range of soil erosion models is studied which includes the Universal Soil Loss Equation (USLE), GIS based USLE (Murimi and Prasad 1998), WEPP (Amore et al 2004), AGNPS (Harregewegn and Yohannes 2003), LISEM(De Ros and Jetten 1999) and Cs137 (Ionita and Margineanu 2000). The Universal Soil Loss Equation (USLE) was developed by Weischmeier and Smith (1978), is the most widely used erosion prediction method.

2-STUDY AREA:

To estimate soil loss field study was conducted in Al- Garmaa located in the south of Basrah. The study area was the embankment of Al-Garmaa Bridge as shown in figure (1). The climate is very hot in summer, cold and rainy in winter with an average annual precipitation of 154.4 mm and a mean annual temperature of 26.5C^{o} (Meteorological Departments, Baghdad- Basrah). Rainfalls mostly occur in spring from March to April, autumn from October to November, and in winter from December, January, and February. The average slope of the embankment is 11%. No land cover and no land use in this embankment as shown in figures (2), (3), and(4).

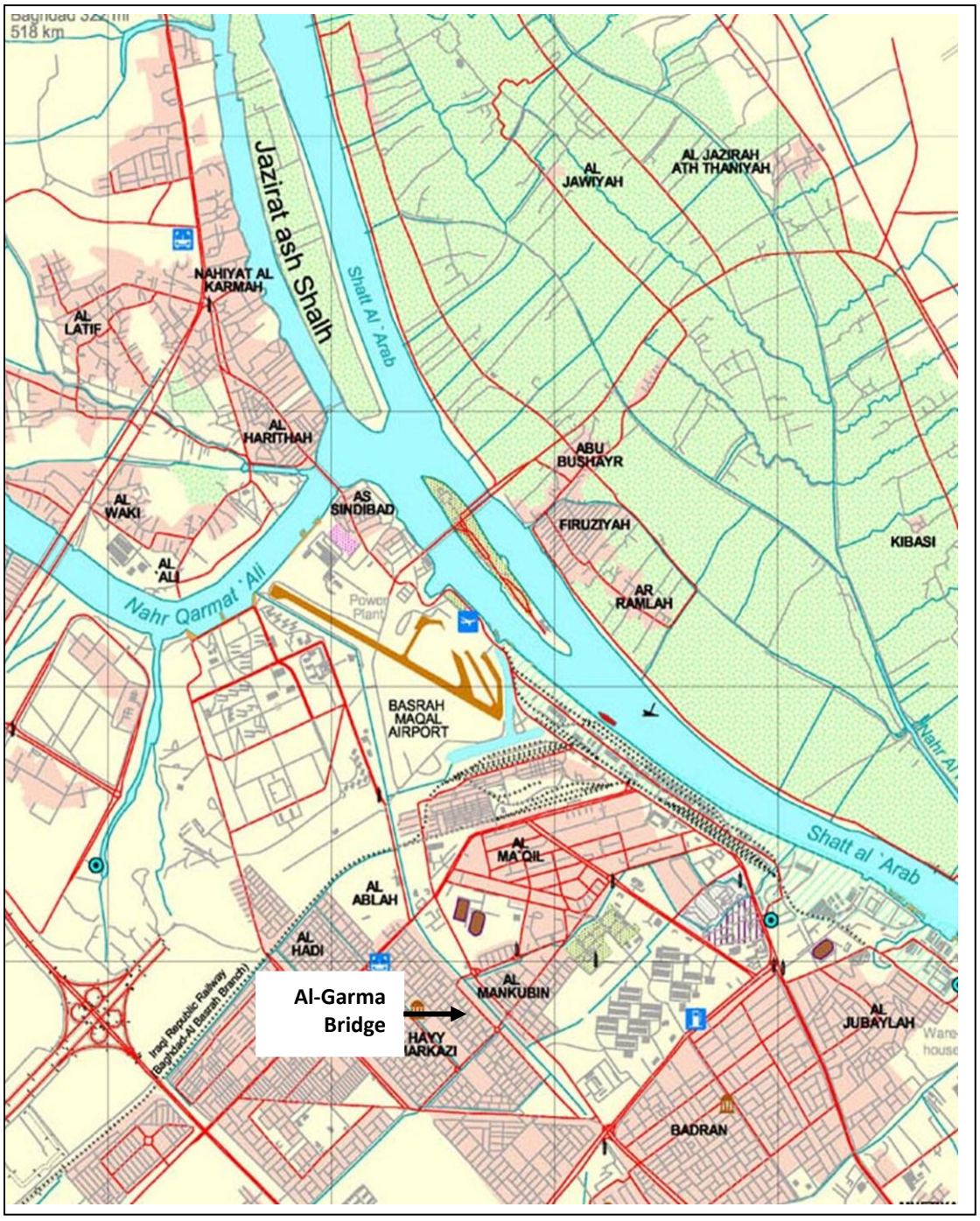

Fig.(1) Location of Al-Garma Bridge in Basrah

Fig.(2) Study embankment with remarked gully erosion

Fig.(3) Study embankment with remarked gully erosion

Fig.(4) Study embankment with remarked gully erosion

3-MODEL DESCRIPTION:

The Universal Soil Loss Equation(USLE) is a hydrological model, which uses a set of parameters to compute soil loss. The four major factors that affect erosion are climate, inherent soil properties including soil erodibility, topography and land use (Jasmin and Ravichandran 2008).

The Universal Soil Loss Equation (USLE) (Wischmeier and Smith 1978):

A = R.K.L.S.C.P ---------- (1)

Where;

A = annual average soil loss (t/ha/year),

R = rainfall and erosivity index for geographic location (MJ. mm/(ha.h)),

K = soil erodibility factor ((t/ha)/(MJ. mm)),

L = slope length factor,

S = slope steepness factor,

C = cropping factor (cover management factor),

P = conservation practice factor.

3-1- CLIMATE

The most important characteristics of rainfall are rainfall intensity and rainfall amount. The average annual erosivity factor, R, is an index of erosivity at a location. Average annual erosivity is computed as the sum of the erosivity (EI_{30}) due to rainfall at a given location , which is the product of the total energy and the maximum 30-min intensity of individual storms. The average annual erosivity is computed as (Jasmin and Ravichandran 2008):

$$\mathbf{R = \sum R_m / m} \quad \text{---------- (2)}$$

Where;

R_m = erosivity of an individual storm,

m = number of storms.

Erosivity of an individual storm is calculated as

$$\mathbf{R_m = EI_{30}} \quad \text{---------- (3)}$$

Where;

E = total storm energy (MJ /ha),

I_{30} = maximum 30-min intensity of individual storm (mm/h).

The total energy of a storm is computed by

$$\mathbf{E = e\,\Delta v} \quad \text{---------- (4)}$$

Where;

e = unit energy (MJ/(ha. mm)),

Δv = rainfall amount (mm).

The unit energy is computed from

$$\mathbf{e = 0.29\,[1 - 0.72\,exp\,(-\,0.082i)]} \quad \text{---------- (5)}$$

where;

i = rainfall intensity (mm/h)

3-2- SOIL:

Erodibility defines the resistance of the soil to both detachment and transport and erodibility varies with soil texture, aggregate stability, shear strength, and organic amount. It was shown that large particles are resistant to transport because of the greater force required entraining them and that fine particles are resistant to detachment because of their cohesiveness.

Soil varies in their susceptibility to erosion. Some soils are naturally more erodible than other soils. Knowledge of basic soil properties such as texture provides an indication of erodibility, which is an important variable.

The equation for soil erodibility factor is: (Jasmin and Ravichandran 2008)

$$K=(k_t k_o + k_s + k_p) / 100 \quad \text{---------- (6)}$$

Where;

K =soil erodibility factor ((t/ha)/(MJ.mm)),

k_t = soil texture subfactor,

k_o = soil organic matter subfactor,

k_s = soil structure subfactor,

k_p = soil profile permeability subfactor.

The soil texture sub factor equation is given by

$$K_{tb} = 2.1[(p_{si} + p_{vfs})(100 - p_{cl})]^{1.14} / 10000 \quad \text{--- (7)}$$

$$K_{t68} = 2.1[68(100 - p_{cl})]^{1.14} / 1000 \quad \text{---------- (8)}$$

$$K_t = k_{tb} \text{ for } p_{si} + p_{vfs} \leq 68\% \quad \text{---------- (9)}$$

$$K_t = k_{tb} - [0.67(k_{tb} - k_{t68}) 0.82] \text{ for } p_{si} + p_{vfs} > 68\% \quad \text{------- (10)}$$

Where;

p_{si} = percentage of silt,

p_{vfs} = percentage of very fine sand,

p_{cl} = percentage of clay,

k_{tb} = base soil texture subfactor,

k_{t68} = soil texture subfactor corresponding to 68%.

The soil organic matter subfactor is given by

$$K_o = (12 - O_m) \quad \text{---------- (11)}$$

Where;

Om = percentage of inherent soil organic matter

The soil structure subfactor is given by

$$K_s = 3.25 (S_s - 2) \quad \text{---------- (12)}$$

Where;

S_s = soil structure class

The soil structure class

1- very fine granular, 2- fine granular, 3- medium or coarse granular, and 4- blocky, play or massive.

The soil profile permeability subfactor is given by

Kp = 2.5 (Pr - 3) ---------- (13)

Where;

Pr = the soil profile permeability rating

The soil profile permeability rating

1- rapid, 2- moderate rapid, 3- moderate, 4- slow to moderate, 5- slow, and 6- very slow.

3-3- TOPOGRAPHY:

The slope length component and slope steepness component constitute the topography part of the model.

The LS factor can be obtained from the equation (Morgan1979)

$$\mathbf{LS} = \sqrt{L/100}\left(0.136 + 0.097S + 0.0139S^2\right) \text{ ------ (14)}$$

Where;

L =slope length (m),

S = slope %.

3- 4- LAND USE:

Erosion occurs when the soil is left bare and exposed to rain drop impact. Among the four factors, land use is the most important because it has the greatest effect and it is the only factor that can most easily be changed to control soil loss and sediment yield. This factor includes the effect of cover, crop sequence, productivity level, length of growing season, tillage practices, residue management, and expected time distribution of erosive events.

The cropping system factor (C) is the ratio of soil loss from land cropped under specific conditions to the corresponding loss from clean- tilled, continuous fallow land. This factor measures the combined effect of all the interrelated cover and management variables. The (C) factor was computed for each crop, crop stage, and supporting practice information in each land use, using agricultural studies (NRCE 1992) and Wischmeier and Smith (1978).

The supporting practices factor (P) is the ratio of soil loss with a specific support practice to the corresponding loss with up- and down- slope culture. The (P) factor was computed for each supporting practice information in each land use, using agricultural studies (NRCE 1992) and Wischmeier and Smith (1978).

4- DATA COLLECTION AND METHODOLOGY:

The estimation of rate of soil erosion has been conducted in the embankment of the AL-Garmaa Bridge using the Universal Soil Loss Equation (USLE). Soil erosion depends upon rainfall intensity, type of soil, slope length, slope steepness, land use / land cover and soil conservation practices. Rainfall data were collected from the office of (Al-anwaa Al-Jawiya) in Basrah for the period (1988 to 2007)except 2003 and 2004. Rainfall records during these years were missing due to the war circumstances. These gagging read rainfall for each 12 hours only and not data for the intensities of this rainfall reading. The relationship between intensity and duration may be expressed by the equation (Holfelder 1980).

$$i = a / (t + b) \quad \text{---------- (15)}$$

Where;

i = rainfall intensity (mm/h),

t = duration of rainfall (min),

a,b = constants.

Rainfall intensity curves have been derived from 24- hour records for frequencies of rains up to once in 10 years as shown in figure (5). From figure (6) “probability of daily rainfall” shows the number of rain events over the period of one year is very small indeed; 19 days with a 24- hour- rain of 1 mm and 15 days with a 24- hour-period of 2 mm.

For European countries ceiling intensities from 25mm/h to 38 mm/h are generally adopted. For Basrah the consultant proposes to use a ceiling intensity of 17.5 (mm/h) which corresponds approximately to duration of 15 min for a “one to two year storm” i.e. I_{30} equal to 12.7 (mm/h)for a duration of 30 min. (Holfelder 1980).

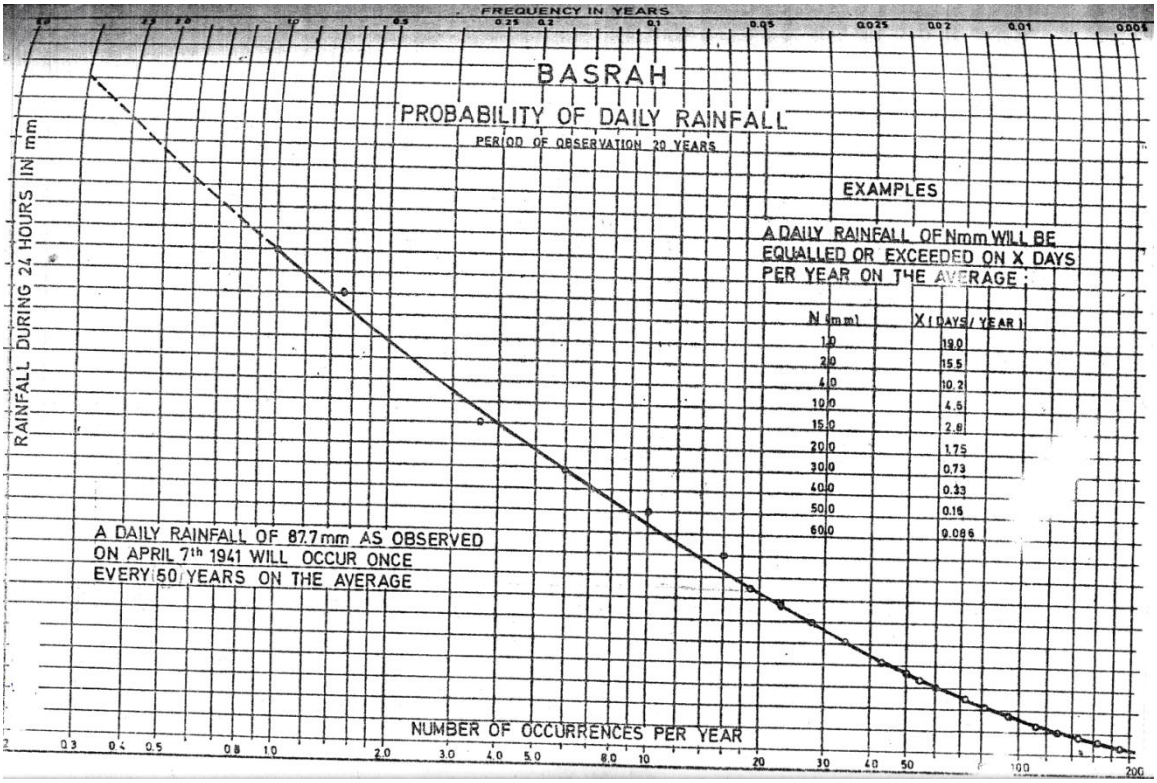

Fig.(5)Basrah probability of daily rainfall (period of observation 20 years). Holfelder(1980).

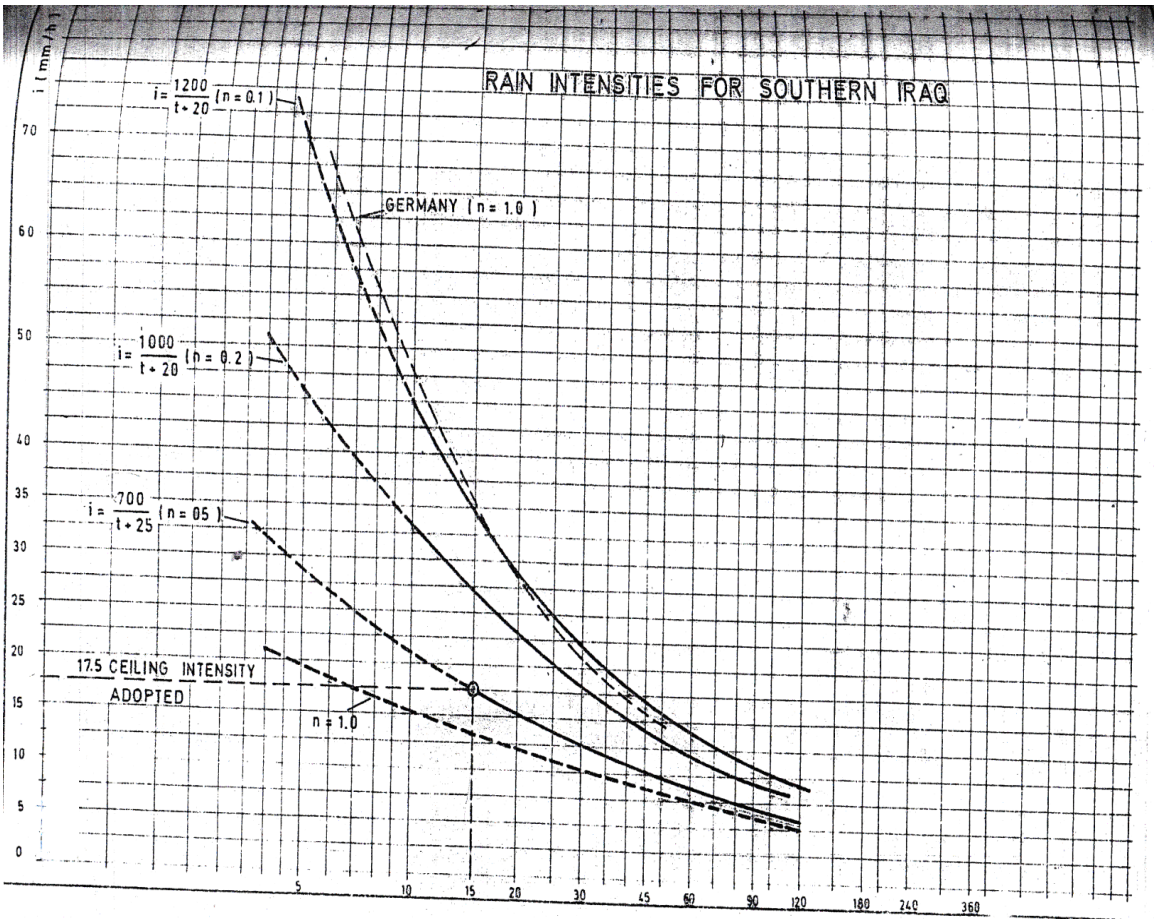

Fig.(6) Rain intensities for southern Iraq. Holfelder (1980).

From these data the annual erosivity index (R) for each year is calculated and the average annual erosivity index is estimated. The average slope of the embankment is 11%. From the average slope zone three soil samples has been taken and the physical soil analysis was done through sieve analysis and hydrometer analysis was done for finding out the percentage of sand, silt, and clay in each sample. The percentage of organic carbon content of soil samples and the permeability for each sample were determined.

Values for cover factor (C) and practice factor (P) were taken as (1). This was done according to the physical condition of the site.

5-RESULTS AND DISCUSSION:

The annual values of rainfall for each year are shown in figure (7) and table (1). It was shown that the maximum rainfall occurred at 1991as (247.1) and the minimum rainfall occurred at 1990 as (48.3). The annual values of erosivity index for each year are obtained as shown in table (1) and figure (8).

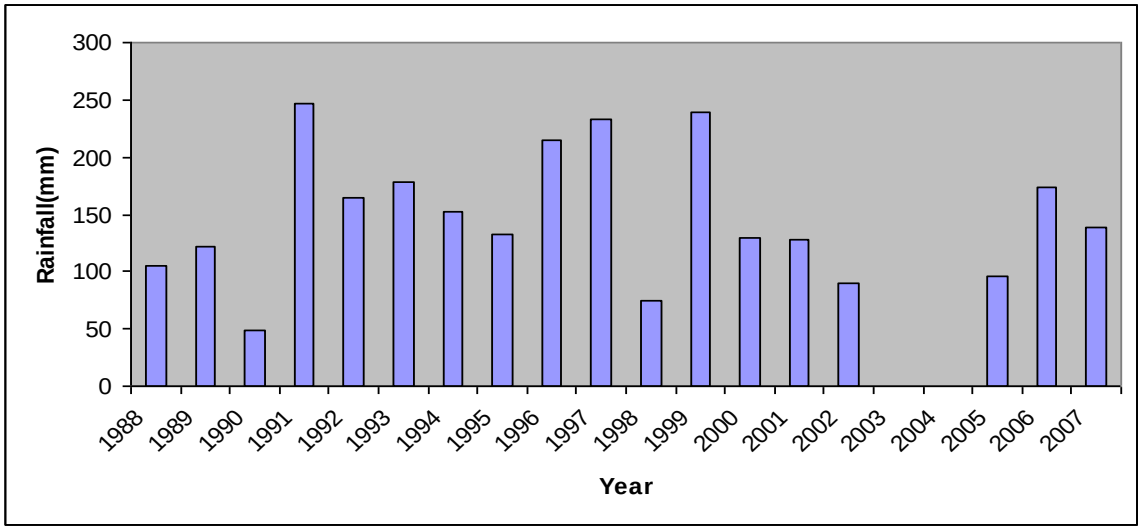

Fig.(7) Annual values of rainfall

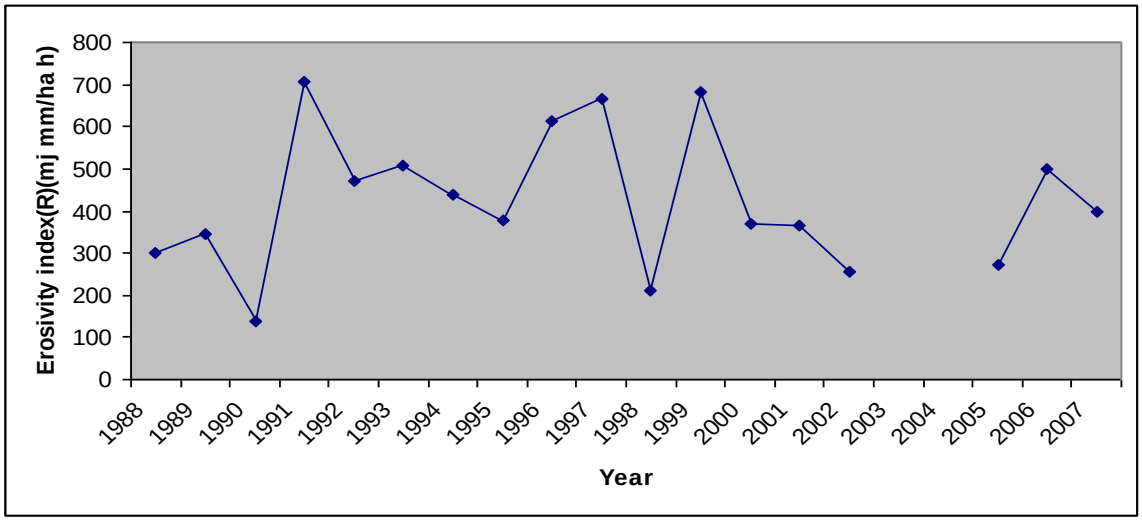

Fig.(8) Annual values for erosivity index (R)

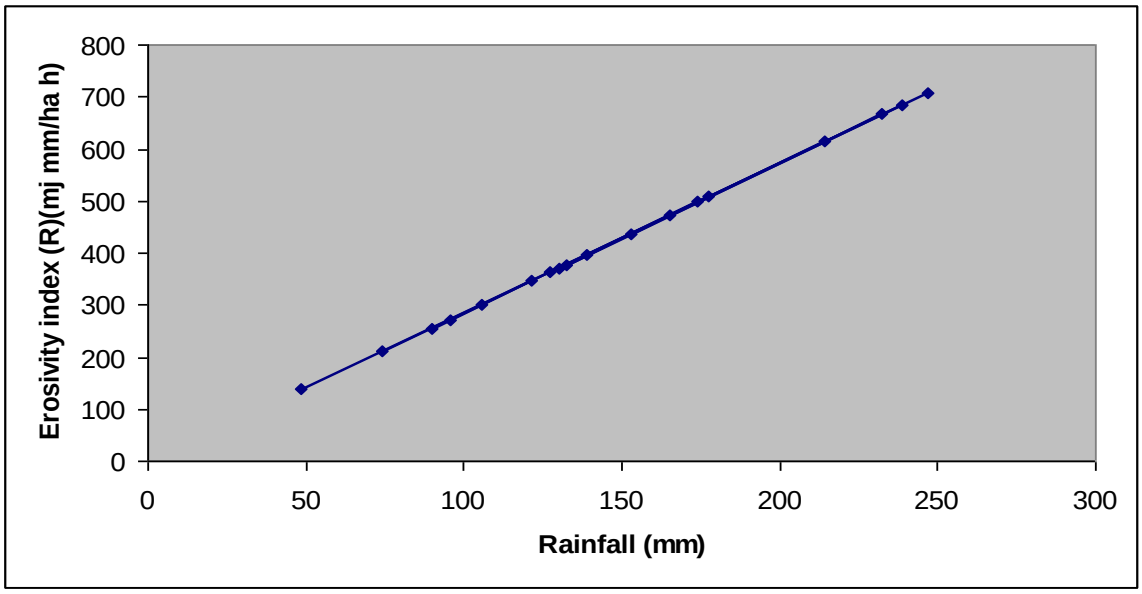

Fig.(9) The relationship between rainfall and the erosivity index

Table (1) : Annual distribution of the erosivity index values (R).

Year	Rainfall (mm)	Kinetic energy(E)	Erosivity index (R)
1988	105.7	8.615	109.4
1989	121.4	9.91	125.9
1990	48.3	3.93	49.9
1991	247.1	20.24	257
1992	165.2	13.5	171.5
1993	177.6	14.51	184.3
1994	153	12.49	158.6
1995	132.3	10.796	137.1

1996	214.2	17.54	222.8
1997	232.5	19.04	241.8
1998	74.2	6.04	76.7
1999	238.6	19.54	248.2
2000	130	10.61	134.7
2001	127.3	10.39	131.9
2002	89.7	7.31	92.8
2005	95.5	7.78	98.8
2226	174.1	14.224	180.6
2007	139.2	11.36	144.3

From table (1),figure(7), and figure (8) it was shown that the minimum erosivity index (R)is 49.9 at 1990 where the rainfall is also minimum and the maximum value of the erosivity index (R) is 257 at 1991 where the rainfall is also maximum and the average annual erosivity index is obtained from equation (2) as 124.99 (MJ mm/ha h). Figure (9) showed that the erosivity index is increased when rainfall increased too.

On the basis of investigations conducted with the presented methodology, the percentage values of silt, clay, sand, very fine sand, and organic amount have been obtained as shown in table (2).

Table (2): Soil parameters for estimation of soil erodibility factor (K).

Sample	O_m%	P_{sl}%	P_{sd}%	P_{vfs}%	P_{cl}%	S_s	P_r
1	4.36	30.64	49.54	12.32	7.5	3	2
2	3.55	1.55	74.98	21.7	1.77	3	2
3	4.12	17.06	61.5	15.94	5.5	3	2
Average	4.01	16.4	62	16.65	4.92	3	2

By using the above values of these indicators and applying them in equation (6) the erodibility factor (K) have been obtained for each sample as shown in table (3).

Table (3): Values of the erodibility factor (K).

Sample	K
1	0.211
2	0.127
3	0.167
Average	0.168

The least resistant particles are silts and fine sands. Thus soils with high silt content are erodible (Richter and Negendank 1977). The erodibility factor is 0.127 for samble(2) and 0.211 for sample (1) and this because the percentage of silt in sample (2) is very small comparatively with sample (1) which is 30.64.

From equation (14) the (LS) factor is obtained as 2.93 for the zone of the average slope.

The cropping management factor (C) and the erosion control practice factor (P) are eliminated which relate specifically to agricultural lands and is applied as a single unit.

Equation (1) is used to estimate the soil erosion for the embankment for the period from 1988 to 2007 as shown in table (4).

Table (4): Values of parameters for estimating soil erosion.

Total(R) (MJmm/ha h)	K ((t/ha)/MJ mm)	LS	C	P	Soil erosion (A)(t/(ha/))
2249.5	0.168	2.93	1	1	1107.29

From the average annual erosivity index (124.99) the average annual soil erosion is obtained as (61.5(t/(ha/year))).

CONCLUTONS:

1-The Universil Soil Loss Equation (USLE) prove to be a very sensitive tool to evaluate soil erosion indexes for:

a- different soil types

b- different rainfall intensities

2- A linear relationship was detected between rainfall and erosivity index.

3- Soil erodibility factor (K) increases with percentage of silt in the studied samples.
4- Annual soil erosion rates according to USLE is in the order of 61.5(t/ha/year).

RECOMMONDATIONS

1- Study the effect of probability maximum precipitation (PMP) on soil erosion.
2- Incorporate the delivery factor in estimating soil erosion.
3-

NOTATIONS:

USLE - universal soil loss equation
A - annual average soil loss
R - erosivity index
K - soil erodibility factor
L - slope length factor
S -slope steepness factor
C -cropping factor
P - conservation practice factor
R_m -erosivity for an individual storm=EI_{30}
m -number of storms
EI -total energy of a storm
I_{30} -maximum 30 minute- intensity of individual storm
e -unit energy
Δv -rainfall amount
i - rainfall intensity
Kt -soil texture sub factor
Ko -soil organic matter sub factor
Ks -soil structure sub factor
Kp -soil profile permeability sub factor
Psi -percentage of silt%
Pvfs -percentage of very fine sand%
Pcl -percentage of clay%
Ktb -base soil texture sub factor%
Kt68 -soil texture sub factor corresponding to 68%

Psd -percentage of sand%

Om -percentage of inherent soil organic matter%

Ss -soil structure class

Pr -soil profile permeability rating

a&b -constants

t -duration of rainfall

REFERENCES:

Amore E., Carlo M., Nearing, MA Santoro, VC(2004).Scale effect of USLE and WEPP application for soil erosion computation from three Sicilian basins. J Hydrol 293:100-114.

De Roo APJ, Jetten VG(1999). Calibrating and validating the LISEM model for two data sets from Netherland and south Africa. Catena37.477-493.

Giovannini, G., Valijo, R., Lucchesi, S., Bautista, S., and Liovet, J. (2001). Effect of land use and eventual fire on soil tradability in dry Mediterranean conditions. Forest Ecol. Manage., 147;15-23.

Haregewegn N., Yohannes F.,(2003).Testing and evaluation of agricultural non- point source pollution model (AGNPS) on Augucho catchment, Western Hararghe, Ethiopio. Agric. Ecosyst Environ99-201-212.

Holfelder G.,(1980). Basrah sewerage and drainage scheme, preliminary phase report, Ministry of housing and construction, Baghdad , Iraq.

Ionita I., Margineanu RM(2000).Application of Cs137 for measuring soil erosion and deposition rate in Romania Acta Geologia Hispania 35-311-319.

Jasmin I., Ravichandran, S., (2008). (RUSLE2) Model application for soil erosion assessment using remote sensing and GIS., Center for water resources, College of Engineering Guindy, Anna University, Chennai, India.

Meteorological Departments, Baghdad- Basrah.

Morgan R., (1979). Soil Erosion., National College of Agricultural Engineering, Silsoe, Bedfordshire, by Longman Inc., New York.

Murimi S. K.,Prassad H.(1998). Modelling potential soil erosion in lake Nakuru Drainage Basin. Ecohydrology. Subramanian V and Ramanathan AL., pp403-414.

Natural Resources Consulîation Engineers (NRCE), (1992). *Watershed Management Studies of Damavand. Ministry of Construction*, Tehran, Iran.

Richter. G. and Negendank, J. F. W.(1977). Soil erosion processes and their measurement in the German area of the Moselle river. Earth surface processes, 2,261-78.

Wischmeier W.H., and *D.D. Smith, (1978). Predicting rainfull erosion tosses-a guide to conservation planning.* USDA, AJncuItural Handbook, NO. 537,58pp.

Effects of Fusion Zone Size on Failure Modes and Mechanical Performance of Dual Phase (DP600) Steel Sheets Spot Welds.

Fadhel A. Hashim[1], Raid K. Salim[2] and Hassanen L. Jaber[3]
1: University of Technology 2: Technical College – Baghdad
3: University of Thi-Qar/ Engineering College/ Mechanical department(hasnen1983@gmail.com)

الخلاصة

يهدف البحث الى دراسة تأثير حجم منطقة اللحام والتركيب المجهري للوصلات الناتجة من لحام المقاومة النقطي لفولاذ ثنائي الطور و شكل الفشل لهذه الوصلات، تم استخدام المجهر الالكتروني الماسح في دراسة التراكيب المجهرية في حين استخدام اختبار الشد-القص لدراسة الخواص الميكانيكية و تحديد نوع او شكل الفشل. بينت النتائج ان التركيب المجهري لمنطقة الانصهار عباره عن مارتنسايت بقيمة صلاده قدرها 450 فيكرز، اما المنطقة المتأثرة بالحرارة فهي عبارة عن فوق الحرجة و تركيبها مارتنسايت صلادته 420 فيكرز والمنطقة ما بين الحرجة بتركيب مارتنسايتي-فرايتي لتنخفض صلادتها الى 310 فيكرز، كذلك بينت النتائج ان نوع (شكل) الفشل يعتمد على مقدار التيار المستخدم حيث ان الفشل يتحول من بيني الى انجراري (انسحابي) عند قيمة تيار قدرها 8,5.

ABSTRACT

This paper examines the effects of fusion zone size on failure modes, quasi tension -shear test and energy absorption of resistance spot welds (RSW) of dual phase (DP600) steels. Optical microscopy was used for microstructure investigation. The results showed that some samples failed in pullout failure mode and other samples failed in interfacial failure mode and the failure was located at the base metal. The conventional weld size guidance of $4t^{0.5}$ and $5t^{0.5}$is not sufficient to produce nugget pullout failure mode for DP600 resistance spot welds.

KEYWORDS: Dual-Phase Steels, Shear-Tension Test, Failure Mode and Resistance Spot Weld

INTRODUCTION

Advanced high-strength steels (AHSSs) have been used in the automotive industry as a solution for the weight reduction, safety performance improvement and cost saving[1- 4]. The Ultra-Light Steel Auto Body (ULSAB) project has shown that

car body mass can be reduced by 25% using advanced high-strength steels (AHSS) and innovative processes[5,6]. It is anticipated that AHSS usage in automotive bodies will climb to 50% by 2015[7].

Dual phase (DP) steels are one of the most common AHSS steels. Dual phase (DP) steels possess a unique microstructure consisting of soft ferrite and hard martensite that offers favorable combination of strength, high work-hardening rate, ductility and formability [2,8]. DP steels are commercially available at present in 500, 600, 780, and 980 MPa minimum tensile strength levels. In recent years, DP600 applications are widely used in different automobile models such as Porsche Cayenne, Land Rover LR2 and Jaguar XF fig. (1)[3,9]. Compared to High-strength low-alloy (HSLA) steels, DP600 steels exhibit a slightly lower yield strength, a continuous yield behavior due to enough active slip systems in the ferrite phase, and a more uniform and higher total elongation (over 21%)[5,7,8].

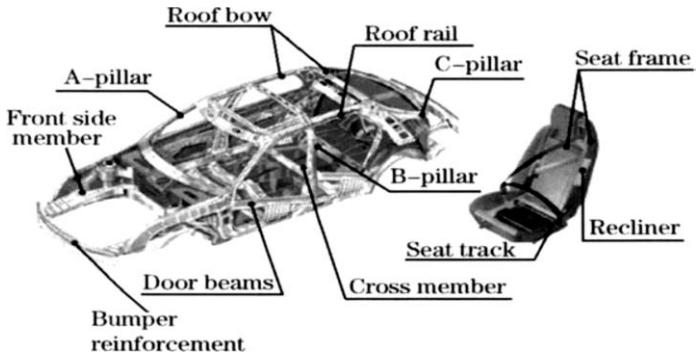

Fig. (1): The automobile parts in which DP 600 steel is used **[**3**].**

DP steels are joined by several welding methods. Resistance spot welding (RSW) is the main joint method of assembly auto body due to its high efficiency in processing thin DP steel sheets. RSW for DP steels is the simplest, fastest, and most controllable. Hence, the automotive industry uses RSW at several thousand welding points about (2000–5000) spot welds in each automotive body structures[10,11]. Therefore, there is a need to study the spot welding behavior of this materials. Generally, there are three measures for quality evaluation of resistance spot welds including physical weld attributes (e.g. fusion zone size,), mechanical properties and failure mode[12,13].

1-1 Physical and metallurgical weld attributes

1 - weld nugget or FZ size (d) which is defined as the width of the weld nugget at the sheet/sheet interface in the longitudinal direction (Fig(2)) is the most important factor in determining the quality of spot welds. Quantitative measurements of the weld size were conducted in two ways: (i) from the weld button diameter on test coupons with a digital calliper (ii) from the cross-section of weld nugget[12,14].

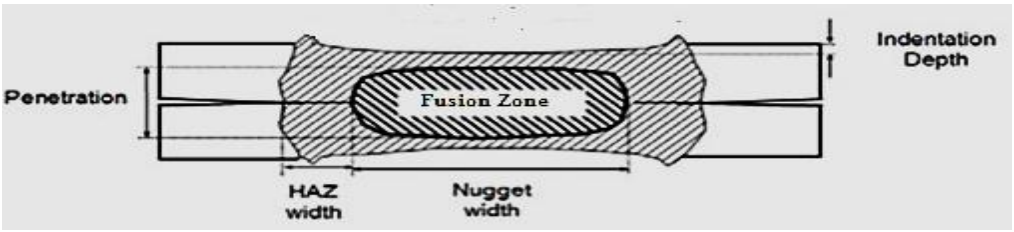

Fig (2) : Geometric Attributes of the Spot Weld [15]

2 – *Expulsion*: The expulsion is The ejection of molten metal from the faying interface (interface between two test coupons) of the samples and observing whether metal "whiskers" or "fingers" are evident at the interface and can lead to a lack of material to fill the weld nugget upon solidification Fig (3).[12,13]

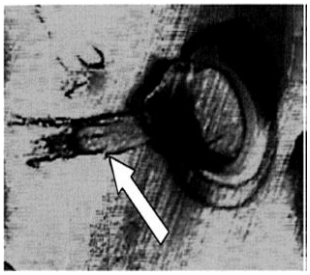

Fig (3) : Expulsion traces at the faying interface of a steel weld [13].

3- *hardness and material properties of fusion zone(*FZ) *and heat affected zone (*HAZ): Hardness and material properties of FZ and HAZ are controlled by the interaction of weld thermal cycle, chemical composition and the initial microstructure of the base metal[16].

1-2 Failure mode

Failure mode of resistance spot welds is a qualitative measure of mechanical properties[13]. Basically, spot welds can fail in two distinct modes described as follows:(i) Interfacial mode (IF), In the IF mode, failure occurs via crack propagation through fusion zone, often occurring in a small weld. The weld fails at the interface of the two sheets, leaving half of the weld nugget in one sheet and half in the other sheet Fig(4) [17].

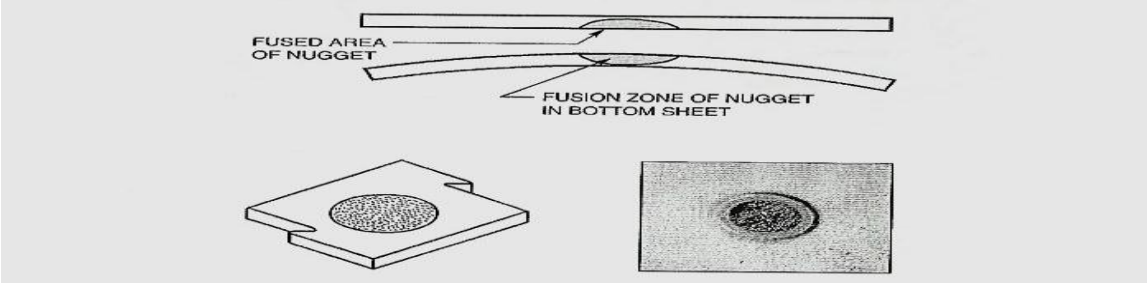

Figure (4): Interfacial Fracture [12]

(ii) pullout failure (PF) occurs via nugget withdrawal from one of the sheets, the weld nugget is completely pulled out from one of the metal sheets, leaving a circular hole in the sheet Fig (5). Some of them failed via complete nugget pullout failure from two sheets called (double pullout) (DPF) while, others experienced sheet tearing after nugget withdrawing from one sheet [17]. Generally, the PF mode exhibits the most satisfactory mechanical properties. Therefore, it is needed to adjust welding parameters so that the PF mode is guaranteed.

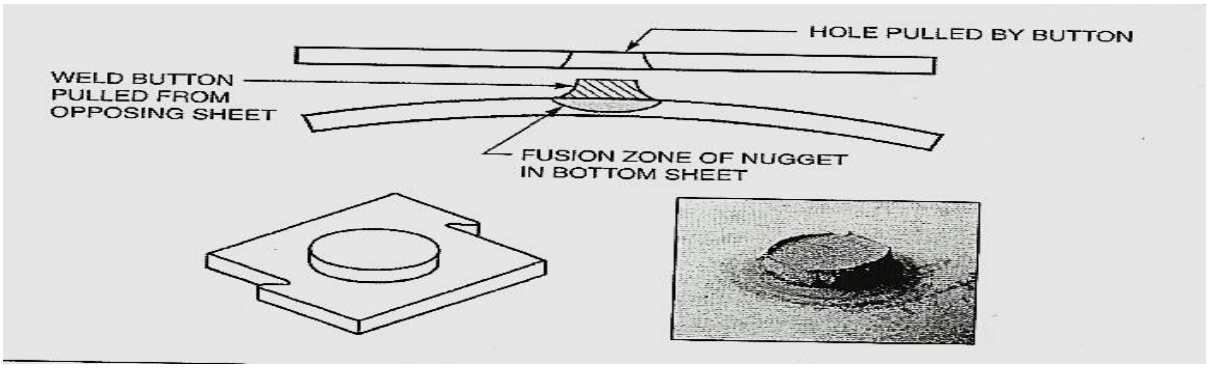

Figure (5) : (a) Button Pull Fracture[12]

1-3 Failure mode prediction

Various industrial standards have recommended a minimum weld size for a given sheet thickness, in order to ensure the PF mode as shown in fig (6).

1 - According to AWS/ANSI/AISI [12], weld button sizing to ensure that the weld size was large enough to carry the desired load, is based on the Equation (1)

$$dc = 4t^{0.5} \quad (1)$$

where, dc is critical fusion zone size in mm, t is sheet thickness in mm.

2 - According to Japanese JIS Z3140[18] and the German DVS 2923[19] standards, the required weld size is specified according to equation (2).

$$dc = 5t^{0.5} \quad (2)$$

3 - Pouranvari and Marashi[16,20] based on the failure mechanism of the spot welds in the tension shear test, proposed a simple analytical model to predict the minimum FZ size (d_c) to ensure the PF mode as shown in equation (3).

$$d_c = \frac{4t}{pF}\left(\frac{HPFL}{HFZ}\right) \quad (3)$$

where t is the sheet thickness (mm), P is the porosity factor and its value (0-1), F = (0.5) is the ratio of shear strength to tensile strength of the F_Z, H_{FZ} and H_{PFL} are hardness values (HV) of the FZ and PF location respectively.

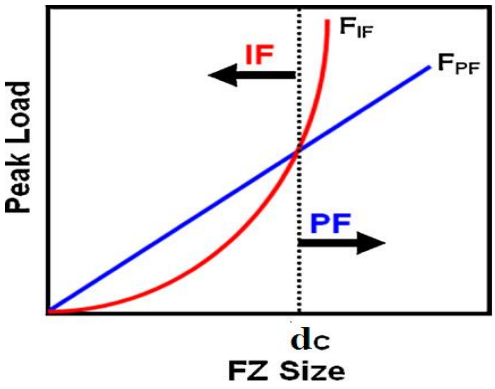

Fig (6): plot of peak load versus fusion zone size both interfacial and pullout failure modes [16]

2 - Experimental procedure

A 1.5 mm thick DP600 dual phased steel sheets were used as the base metals. The chemical composition of the base metals is presented in Table 1. The mechanical properties of the base metals were determined using a standard tensile test in accordance to ASTM E8. Fig. 7 shows the mechanical properties of the investigated steels.

Table (1) Chemical composition of DP600 steel

Element % / Steel		C	Mn	P	S	Si	Cr	Mo	V	Nb	Cu	Ni	Fe
DP600	Actual	0.07	1.52	0.008	0.011	0.048	0.1	0.02	0.01	0.005	0.03	-	Base
	Nominal	0.06-0.15	1.5-2.5	-	-	-	0.4	0.4	0.06	0.04	-	-	-

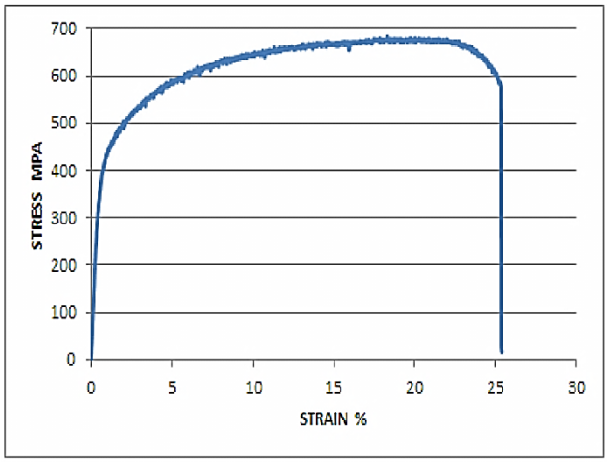

Figure (7) stress vs. strain curves for DP600.

Welding process was performed by a 120 kVA ac pedestal type resistance spot welding machine, controlled by a programmable logic controller. Welding was conducted using a 90° truncated cone Resistance Welding Manufacture Association RWMA Class two electrodes[12], with face diameter of 6 mm. The welding process was carried out with a constant electrode pressure of 4 bar. Squeeze time, welding time and holding time were kept constant at 45, 15 and 10 cycles, respectively. Experiments were done with changing the welding current from 6 to 13 kA.

The samples for the tensile-shear test were prepared according to ANSI/AWS/SAE/ D8.9-2012 standard[12] fig. (8). The tensile shear test was performed by an Instron universal testing machine at a cross head of 2 mm/min. Standard metallography procedure was conducted to examine the microstructure of fusion zone and heat affected zone by optical microscopy . The fusion zone size was measured on the metallographic cross sections and digital calliper. Vickers micro-hardness test was performed to obtain hardness profile using an indenter load of 200g.

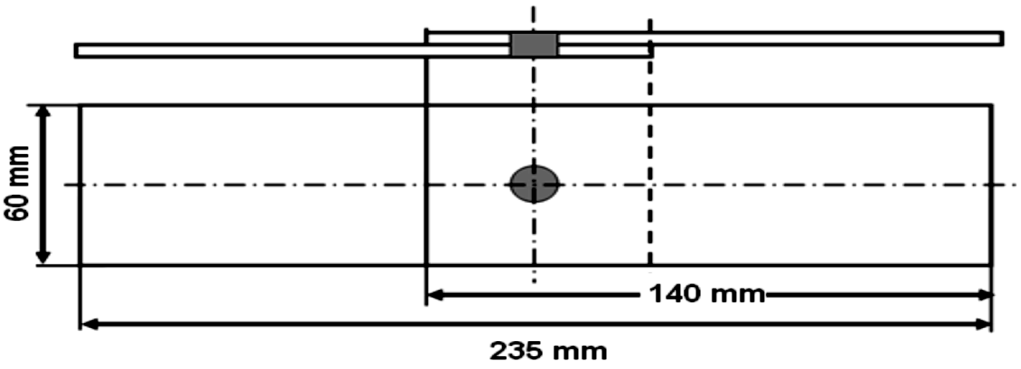

Figure (8):Test configuration and sample dimensions of tensile shear test

Peak load (measured as the peak point in the load–displacement curve) and the failure energy (measured as the area under the load–displacement curve up to the peak load)[13]fig. (9) were extracted from the load–displacement curve by using the concept of Riemann Sums equation (4). The data points for peak load and failure energy are averages of the measured values for the three specimens.

$$\int_0^{Lmax} \mathbf{Fdx} = \sum_{n=1}^{N} \mathbf{F(n).[L(n) - L(n-1)]} \qquad \mathbf{(4)}$$

where F is the load, X the displacement, L_{max} the displacement at the peak load, n the sampled data and N the peak load.

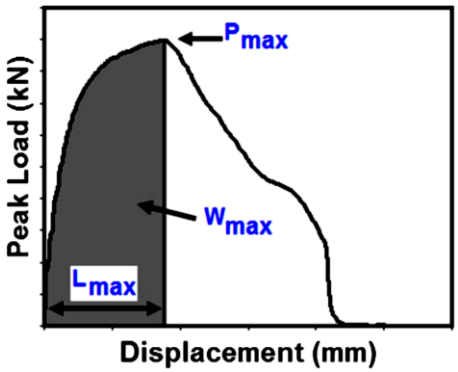

Fig. 9. Load–displacement curve of spot welds during tensile-shear test[13].

3- Results and discussions

3-1 Effect of Welding Current on Weld physical Attributes

Fig. (10a) shows the effect of welding current on the peak load of welds indicating that generally increasing welding current increases the load bearing capacity. However, at high heat input welding condition (welding current beyond 11kA), peak load is reduced due to expulsion. Fig. (10b) shows the effect of welding current on the failure energy indicating that increasing heat input caused by increasing welding current increases the energy absorption capability of the welds. However, at high heat input welding condition (welding current beyond 11kA) energy absorption is significantly reduced due to expulsion as shown in fig. (11).

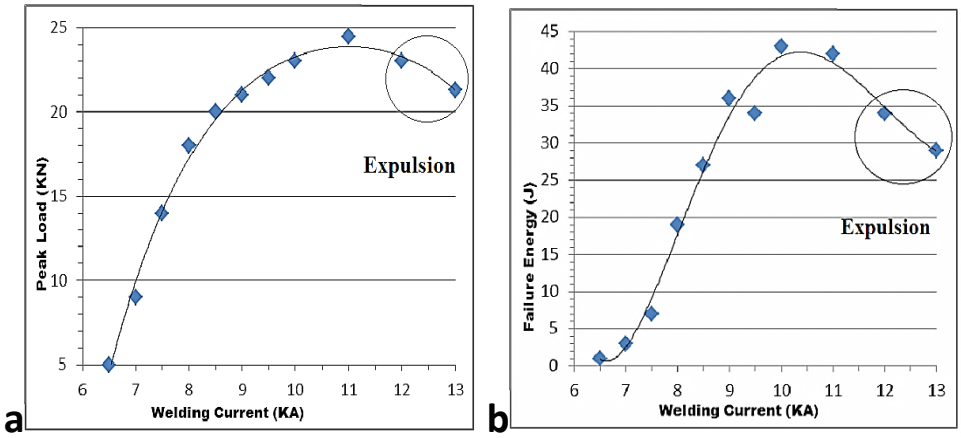

Fig (10): (a): Effect of welding current on the peak load, (b) Effect of welding current on the failure energy.

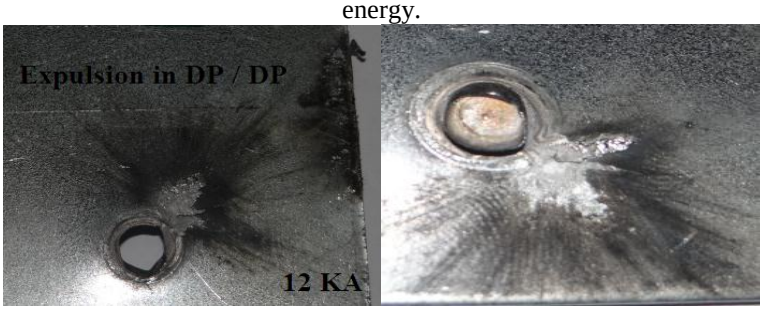

Fig (11): Expulsion traces at the faying interface of DP/DP RSW.

Fig. (12a) shows the effect of FZ size on the peak load. As can be seen, there is a direct correlation between FZ size and peak load. Fig. (12b) shows the effect of FZ size on the failure energy indicating that there is a direct correlation between FZ size and the failure energy.

According to fig. (12a, b), fusion zone size is the most important controlling parameter of peak load and energy absorption of the DP600 spot welds. Similar conclusion was obtained for galvanized low carbon steel [21], TRIP800 steel, DP800 [1]. In summary, increasing welding current results in higher heat generation at the faying interface resulting in the formation of larger fusion zone and increases overall bond area. These facts can explain increasing in peak load and energy absorption until optimal welding conditions are received.

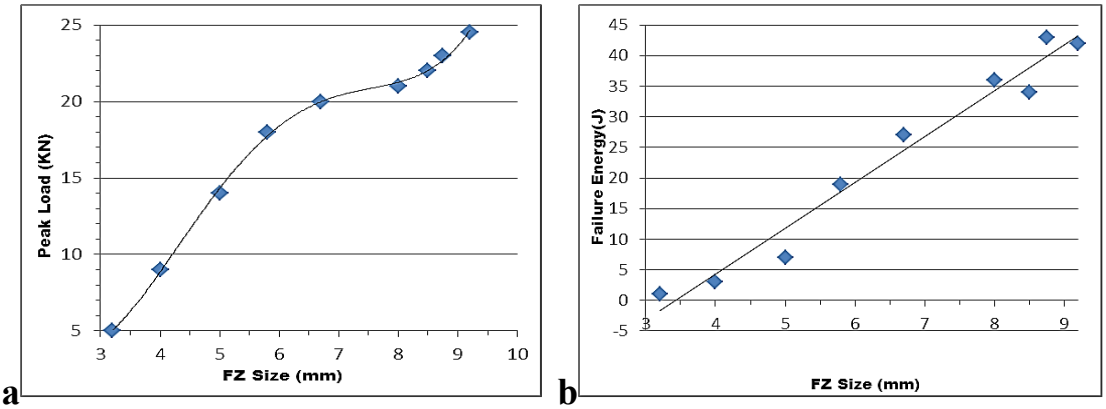

a b

Fig (12):**(a)**: Effect of fusion zone size on the peak load , **(b)**: Effect of fusion zone size on the failure energy.

3-2 Failure mode of DP/DP

Fig. (13a) shows a typical fracture surface of a spot weld which was failed in the interfacial failure mode at 8.5 KA. During interfacial mode spot weld is failed through the weld nugget centerline. As can be seen, interfacial failure mode is accompanied by little plastic deformation. Fig. (13b, c) shows a typical fracture surface of spot welds failed in the pullout failure mode(shear tearing and double pullout) at 9.5 KA and 10 KA receptively as shown in Table 2. The double pullout failure mode (DPF) fig (13c) is convert to pullout failure on expulsion as shown in table 2. Similar conclusion has been obtained on the effect of expulsion in galvanized low carbon steel [21]. In addition to the effect of expulsion on the static performance, Ma et al. [14], in their study on the failure behavior of DP600, reported that expulsion could decrease the fatigue limit of the spot weld.

Fig (13): Failure modes of DP600/DP600 RSW: (a): Interfacial Failure mode. (b): shear tearing. (c): double pullout failure .

Table 2: Effect of welding current on the fusion zone size and failure mode

Welding Current (KA)	Fusion Zone Size (mm)	Failure Mode
6.5	3.2	IF
7	4	IF
7.5	5	IF
8	5.8	IF
8.5	6.7	IF
9	8	PF+ shear tearing
9.5	8.5	PF+ shear tearing
10	8.75	DPF
11	9.2	DPF
12	6.25	PF

3-3 Microstructure of DP/DP

A typical macrostructure of DP600 RSW revealed three distinct zones, fusion zone (FZ), heat affected zone (HAZ) and base metal (BM) as shown in fig (14a). Fig. (14b) shows a typical micro-hardness profile of the DP600 steel, which exhibited a significant hardness increase from the base metal. The hardness of fusion zone is about 2.2 times more than that of the base metal, at a value of approximately 450HV. According to the temperature distribution, HAZ can be divided into two distinct metallurgical transformation zones, namely, high temperature HAZ (UCHAZ) above A_{C1}, middle temperature HAZ (ICHAZ) between A_{C1} and A_{C3}. optical microscope was used to examine the microstructural variations as shown in fig (15). Fig (15a) shows that the microstructure in the base metal basically consists of evenly distributed martensite(light brown) within the ferrite phase(white). The HAZ can be divided into two distinct regions: ICHAZ and UCHAZ. Fig. (15b) shows the boundary of ICHAZ and UCHAZ.

Fusion zone (FZ) microstructure Fig. (15c) predominately consists of full martensite phase which is responsible for the high value of measured hardness (450HV). Martensite formation in the FZ is attributed to the high cooling rate of RSW process due to the presence of water cooled copper electrodes and their quenching

effect as well as short welding cycle. For DP steels, the required critical cooling rate to achieve martensite phase in the microstructure can be estimated using the equation[20] **(**Log v = 7.42 – 3.13C – 0.71Mn – 0.37Ni – 0.34Cr – 0.45Mo), where V is the critical cooling rate in K h−1. For this steels the critical cooling rate is **407 (K s^{-1})(134C° s^{-1})**.

In RSW process, increasing sheet thickness reduces the cooling rate due to increasing the distance of liquid pool from the water cooled electrode with increasing sheet thickness. Gould et al. [22] developed a simple analytical model predicting cooling rates of resistance spot welds. According to this model, cooling rate for sheet having 1.5 mm thickness is about 4000 K s^{-1}[20]. These cooling rates are much higher than those needed to form martensite in the weld and HAZ in DP steels. Therefore, the high cooling rate during RSW, leads to the formation of martensite in the fusion zone of the DP600 steel.

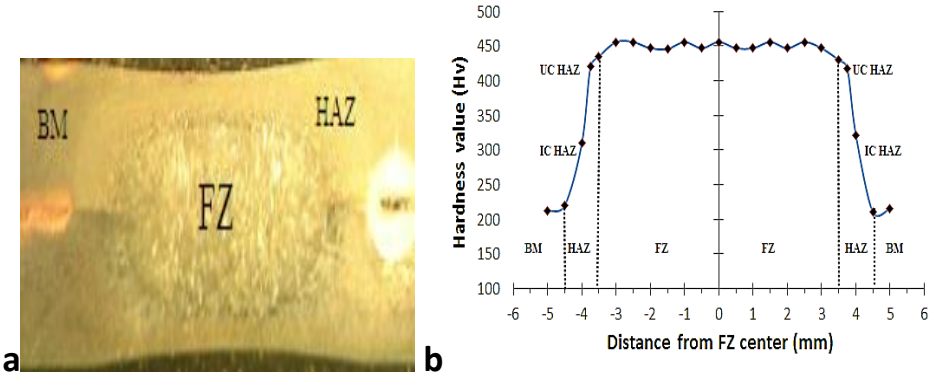

Fig (13): a: Macrograph of DP/DP and b: a typical micro-hardness profile of the DP600 steel after RSW.

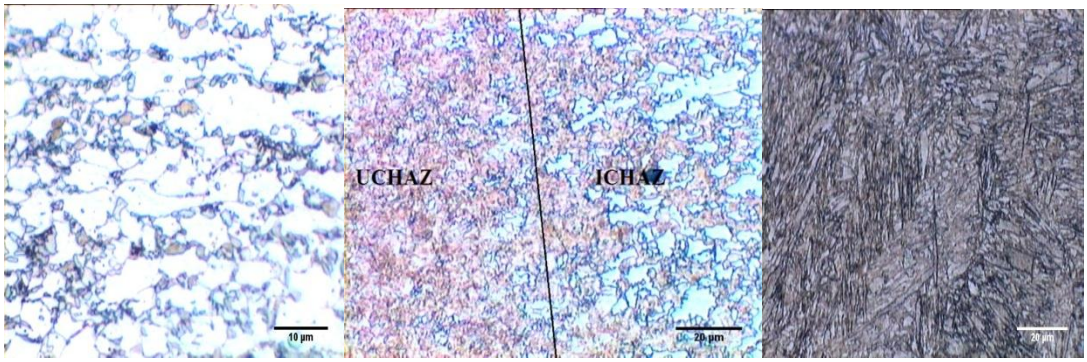

Fig (14): a: Base metal microstructure of DP600. b: ICHAZ- UCHAZ boundary. C: Fusion zone microstructure of DP600/DP600.

Table (3): summary showing materials, hardness characteristics and failure mode of dual phase steels, predicted critical fusion zone size and Experimental fusion zone size.

Material welding	t mm	H_{BM}	H_{MIN} ~ H_{FL}	H_{MAX} ~ H_{FZ}	H_{FL}/H_{FZ}	IF	PF	AWS $4t^{0.5}$	JIS, DVS $5t^{0.5}$	$\frac{4t}{pf}(\frac{HPFL}{HFZ})$	(dcr) Experimental
DP600 / DP600	1.5	212	212	452	0.47	d ≤ 7 mm	d≥ 8 mm	4.9 mm	6.124 mm	5.62 mm	8 mm

*H: Hardness, MIN: Minimum, MAX: Maximum and FL: Failure Location

4-Conclusions

1- The conventional weld size guidance of $4t^{0.5}$ and $5t^{0.5}$is not sufficient to produce nugget pullout failure mode for DP600/ DP600 spot welds.

2 - Generally, increasing welding current increases the peak load and energy absorption primarily due to increasing the overall bond area caused by FZ size enlargement and as a consequence of the transition in failure mode from interfacial to pullout.

3 - Excessive welding heat input, where expulsion occurs, the peak load and energy absorption capability significantly reduce. Significant reduction of failure energy can be attributed to the reduction of weld fusion zone at high welding current.

4 - Welds with larger fusion zone size typically generate higher peak loads and energy absorption levels. Weld fusion zone size is the most critical factor in weld quality in terms of peak load and energy absorption for DP600/DP600.

References

1 – X. Sun, E. Stephens and M. Khaleel," Effects of Fusion Zone Size on Failure Modes and Performance of Advanced High Strength Steel Spot Welds ", SAE, PAPER SERIES 2006-01-0531.

2 - International Iron and Steel Institute, " ADVANCED HIGH STRENGTH STEEL (AHSS) APPLICATION GUIDELINES", Version 4.1, June 2009.

3 – F. Hayat, "Comparing Properties of Adhesive Bonding Resistance Spot Welding and Adhesive Weld Bonding of Coated and Uncoated DP 600 Steel ", JOURNAL OF IRON AND STEEI. RESEARCH, INTERNATIONAL. 18(9): PP. 70-78, (2011).

4 - J. Galán, L. Samek, P. Verleysen, K. Verbeken and Y. Houbaert, "Advanced high strength steels for automotive industry$^{(\cdot)}$ " rEviSTa DE METalUrGia, 48 (2), MarZo-aBril, PP. 118-131, 2012.

5 - M. MARYA and X. Q. GAYDEN "Development of Requirements for Resistance Spot Welding Dual-Phase (DP600) Steels Part 1 — The Causes of Interfacial Fracture " WELDING JOURNAL, pp. 173-182, NOVEMBER 2005.

6 – Z. Xiaoyun, C. Guanlong, Z. Yansong, L. Xinmin, "Improvement of resistance spot weldability for dual-phase (DP600) steels using servo gun", journal of materials processing technology 2 0 9, PP. 2671–2675, 2 0 0 9.

7 - TUMULURU, "Resistance Spot Welding of Coated High-Strength Dual-Phase Steels ", WELDING JOURNAL, PP. 31-37, AUGUST 2006.

8 - R. KUZIAK, R. KAWALLA, S. WAENGLER, "Advanced high strength steels for automotive industry " ARCHIVES OF CIVIL AND MECHANICAL ENGINEERING, Vol. VIII, No. 2, pp103-117, 2008.

9 - H. Hofmann, D. Mattissen, T. W. Schaumann, "Advanced cold rolled steels for automotive applications", Mat.-wiss. u. Werkstofftech, 37, No. 9, PP. 716-723, 2006.

10 - F. Hayat & İ. Sevim "The effect of welding parameters on fracture toughness of resistance spot-welded galvanized DP600 automotive steel sheets" Int J Adv Manuf Technol 58, PP.1043–1050, 2012 .

11 - S.B. Behravesh, L. Liu, H. Jahed, S. Lambert, G. Glinka and Y. Zhou, "Effect of Nugget Size on Tensile and Fatigue Strength of Spot Welded AZ31 Magnesium Alloy", SAE International SAE, PAPER SERIES 2010-01-0411.

12 - ANSI/AWS/SAE, " Test Method For Evaluating The Resistance Spot Welding Behavior of Automotive Sheet Steel Materials", American Welding Society, 2012.

13 - H. Zhang and J. Senkara: "Resistance Welding: Fundamentals and Applications", (CRC Group, Boca Raton, FL, 2006).

14 - C. Ma, D.L. Chen, S.D. Bhole, G. Boudreau , A. Lee , E. Biro "Microstructure and fracture characteristics of spot-welded DP600 steel " Materials Science and Engineering A 485, PP. 334–346, (2008) .

15 - Gilvan Prada, "Correlation Study of Spot Welded Specimens'Behavior using Finite Element Method", SAE, PAPER SERIES 2008-36-0100.

16 - M. Pouranvaria, S.P.H. Marashi, "Failure mode transition in AHSS resistance spot welds. Part I. Controlling factors ", Materials Science and Engineering A 528, PP. 8337– 8343, (2011).

17- M. Goodarzia, S.P.H. Marashib, M. Pouranvari, "Dependence of overload performance on weld attributes for resistance spot welded galvanized low carbon steel", Journal of Materials Processing Technology, 209, PP. 4379–4384, (2009). .

18 - Industrial Standards Committee, Tokyo, 'Method of inspection for spot welds', JIS Z 3140, Japanese Japan, (1989).

19 - 'Resistance spot welding', DVS 2923, German Standard. Du¨ sseldorf , Germany, 1986.

20 - M. Pouranvari, S.P.H. Marashi, D.S. Safanama, "Failure mode transition in AHSS resistance spot welds. Part II: Experimental investigation and model validation ", Materials Science and Engineering A 528, PP. 8344– 8352, (2011).

21 - M. Pouranvari, S.P.H. Marashi, "On the failure of low carbon steel resistance spot welds in quasi-static tensile–shear loading ", Materials and Design 31, 3647–3652, (2010) .

22 - E. GOULD, S. P. KHURANA, T. LI, "Predictions of Microstructures when Welding Automotive Advanced High-Strength Steels ", WELDING JOURNAL, MAY 2006, pp111s-116s.

Mixed Convection Heat Transfer Inside A vented Square Enclosure with Concentric Rotation Inner Cylinder

Dr. Ahmed K. Alshara
Mechanical Engineering Department
College of Engineering
Basra University

Dr. Falah A. Abood
Mechanical Engineering Department
College of Engineering
Basra University

Huda A. Al-mayahi
Mechanical Engineering Department
College of Engineering
Basra University

ABSTRACT:

Mixed convection heat transfer for laminar air flow inside a vented square enclosure with rotation inner cylinder is studied numerically The bottom wall is heated at constant temperature (T_h) while the other walls and the surfaces of the inner cylinder are adiabatic. An external flow enters the square cavity through an opening located down the left vertical wall and exits from an opening located in the upper right wall. The conservation governing equations (continuity, momentum and energy are solved by finite element method using Flex PDE software package. Results of velocity curves, isotherms and average Nusselt number show the effect of the variables: Richardson number (Ri = 0,6,10), Reynolds number (Re = 20, 50, 100), Prandtl number (Pr = 0.7), the dimensionless angular velocity (Ω = 0 –3) and dimensionless radius of rotating cylinder (R= 0 - 0.3) on heat transfer and flow filed. The results show that, the average Nusselt number increases with increasing Ri, Re, R and decreases with increasing Ω. The results are compared with other authors in the literature and give a good agreement.

Key words: Mixed convection, Rotating cylinder, Square enclosure.

انتقال الحرارة بالحمل المختلط داخل فجوة مربعة تحوي اسطوانة داخلية متمركزة دوارة

المستخلص :

تم في هذا البحث دراسة نظرية لانتقال الحرارة بالحمل المختلط لجريان الهواء الطباقي داخل فجوة مربعة تحتوي اسطوانة داخلية دوارة. الجدار السفلي مسخن عند درجة حرارة ثابتة (T_h) أما الجدران الأخرى وكذلك سطح الاسطوانة الداخلية فتكون معزولة. الجريان الخارجي يدخل الفجوة المربعة بدرجة حرارة (T_{in}) خلال فتحة تقع أسفل الجدار الأيسر ويخرج من فتحة تقع في أعلى الجدار الأيمن. معادلات الحفظ الحاكمة (الاستمرارية ، الزخم ، الطاقة) حُلت بطريقة العناصر المحددة باستخدام الحقيبة البرمجية FlexPDE . نتائج

مخططات السرعة و خطوط ثابتة درجة الحرارة وضحت تأثير المتغيرات : رقم ريتشارد (Ri = 0,6,10)، رقم رينولدز (Re =20,50,100)، رقم براندل(Pr = 0.7), السرعة الزاوية اللابعدية (Ω=0-3) و نصف قطر الأسطوانة الدوارة اللابعدي (R=0-0.3) على انتقال الحرارة والجريان . وجد بان معدل رقم نسلت يزداد بزيادة Ri,Re ,R ويقل بزيادة Ω .النتائج قورنت مع نتائج باحثين آخرين وأظهرت نتائج جيدة.

1. Introduction:

Mixed convection occurs in many heat transfer devices, such as the cooling system of a nuclear power plant, large heat exchangers, cooling of electronic equipment and ventilation. The relative direction between the buoyancy force and the externally forced flow is important. In the case where the fluid is externally forced to flow in the same direction as the buoyancy force, the mode of heat transfer is termed assisting combined forced and natural convection. In the case where the fluid is externally forced to flow in the opposite direction to the buoyancy forced, the mode of heat transfer is termed opposing mixed convection [1]. There are many geometric configuration of enclosures filled with a convective fluids such as rectangular, triangular, elliptical and circular enclosures. Shung et. al. [2] studied numerically natural convection heat transfer in an enclosure with a rotating cylinder. A penalty finite-element method with a Net Jon-Raphson iteration algorithm is adopted to solve the governing equations with the boundary conditions. The results show that, when the value of (Gr/Re) is high, the enhancement of the heat transfer rate begins to be revealed. Khanafar et. al. [3] studied numerically mixed convection heat transfer in open ended enclosure for three different flow angles of attack. Discreization of the governing equations is achieved using a finite element scheme based on the Galerkin method of weighted residuals. The results show that thermal insulation of the cavity can be achieved through the use of high horizontal velocity flow. Lasode [4] studied numerically laminar mixed convection heat in vertical elliptic ducts containing an upward flowing fluid rotating about parallel axis. The coupled system of normalized conservation equations are solved using a power series expansion in ascending powers of rotational Rayleigh Number. The results show that, the mean Nusselt number is decreases with eccentricity for high heating rates.

Kim et. al. [5] performed numerically natural convection problem in a cooled square enclosure with an inner heated circular cylinder. The immersed boundary method was solved by finite volume method to simulate the flow and heat transfer over an inner circular cylinder in the Cartesian coordinates. The results show that, the

location of the peak and valley of the local Nusselt number along the surfaces of the inner cylinder and enclosure depends on the location of the center of these vortices. Rahman et. al. [6] studied the mixed convection in a cavity contains a heat conduction of horizontal square block located at the center. The investigations are conducted for various values of geometric size, location and thermal conductivity of the block under Pr and Re. The results indicated that the average Nu number at the heated wall is highest for the lowest value of cavity aspect ratio ,but the average temperature of the fluid in the cavity and temperature at the cylinder center are the lowest for the highest value of aspect ratio. Costa et. al. [7] studied numerical mixed convection in a square enclosure with a rotating cylinder centered within. For high values of the cylinder radius, the overall Nusselt number is small if the rotating velocity is low, and it considerably increases, in a nearly linear way, with the rotating velocity absolute value and the overall Nusselt number becomes maximum if the diameter to height ratio is small, for rotating velocities close or equal to zero. Saha et. al. [8] studied numerically mixed convective flow in a lid-driven square cavity with uniform internal sources. The top moving lid of the cavity and the bottom wall is maintained at constant temperature, while the vertical walls are thermally insulated. The results show that, the average Nusselt number becomes an increasing function of increasing Ri.

Lee et. al. [9] investigated numerically the effect of the natural convection heat transfer in a square enclosure with a circular cylinder at different horizontal and diagonal locations the effect of buoyancy-induced convection on the fluid flow and heat transfer in the enclosure increases and as a result the locations of the local minimum of Nusselt number on the cylinder surface and the local peaks of the Nusselt number on the enclosure wall are strongly depended on the origin and the inclined direction of the thermal plume. Abood et. al. [10] studied numerically mixed convection heat transfer inside a vented square cavity with inner heated cylinder by finite element method to solve the conservation of governing equations. The results show that with increases of Re and Ri numbers the convective heat transfer becomes predominated over the conduction heat transfer. Alshara [11] studied numerically the effect of rotating horizontal single or multi cylinders on mixed convection heat transfer in an equilateral triangular enclosure filled with air. Three cases are performed: single rotating cylinder, three rotating cylinders at the same direction and three rotating cylinders at different directions. It was found that the average Nusselt number for the single or multi rotating cylinder is increased with increasing Ra, R and Ω for all cases.

The main aims of the present study are to show the effect of rotation inner cylinder on the mixed convection and to show the effect of the parameters: radius of cylinder, Reynolds number and Richardson number on Nusselt number, velocities, isotherms and average temperature.

2. Theoretical Analysis:

Figure 1. shows a schematic illustration of the problem under consideration. It is a two- dimensional vented square enclosure with height H and base L and centered rotating solid cylinder at angular velocity ω (clock wise is positive direction). The bottom wall is heated at constant temperature T_h while the other walls are assumed to be adiabatic. The inflow opening located on the bottom of the left vertical wall of the enclosure and exit from the opening located on the top right wall. The viscous dissipation term in the energy equation and radiation are neglected. The governing equations for the steady, laminar, two dimensional, incompressible flow with Boussinseq approximation and constant fluid properties can be written in non-dimensional form as follows [10]:

Continuity equation

$$\frac{\partial U}{\partial X}+\frac{\partial V}{\partial Y}=0 \quad (1)$$

Momentum equation in x-direction

$$U\frac{\partial U}{\partial X}+V\frac{\partial U}{\partial Y}=-\frac{\partial P^{*}}{\partial X}+\frac{1}{\mathrm{Re}}\left(\frac{\partial^2 U}{\partial X^2}+\frac{\partial^2 U}{\partial Y^2}\right) \quad (2)$$

Momentum equation in y-direction

$$U\frac{\partial V}{\partial X}+V\frac{\partial V}{\partial Y}=-\frac{\partial P^{*}}{\partial Y}+\frac{1}{\mathrm{Re}}\left(\frac{\partial^2 V}{\partial X^2}+\frac{\partial^2 V}{\partial Y^2}\right)+Ri\,\theta \quad (3)$$

Energy equation

$$U\frac{\partial \theta}{\partial X}+V\frac{\partial \theta}{\partial Y}=\frac{1}{\mathrm{Re}\,\mathrm{Pr}}\left[\frac{\partial^2 \theta}{\partial X^2}+\frac{\partial^2 \theta}{\partial Y^2}\right] \quad (4)$$

Where the dimensionless variables are defined as:

$$X=\frac{x}{L},\ Y=\frac{y}{L},\ U=\frac{u}{u_{in}},\ V=\frac{v}{u_{in}},\ \theta=\frac{T-T_{in}}{T_h-T_{in}}$$

$$P^*=\frac{p}{\rho u_{in}^2},\ \Pr=\frac{\nu}{\alpha},\ Ri=\frac{Gr}{\mathrm{Re}^2},Gr=\frac{g\beta(T_h-T_{in})L^3}{\nu^2},and\ \ \Omega=\frac{\omega(D/2)}{u_{in}}$$

The B**oundary Conditions are :**

U =1 , V= 0 and θ = 0 at the inlet

U=V= 0 and θ=1 at bottom wall

U=V=0 and $\frac{\partial\theta}{\partial N}=0$ at the other walls of enclosure

V=0 , $P^*=0$, $\frac{\partial U}{\partial X}=0$ and $\frac{\partial\theta}{\partial X}=0$ at the outlet

$U=\Omega(Y-Y_o)$, $V=-\Omega(X-X_o)$ and $\frac{\partial\theta}{\partial N}=0$ at the surface of rotating solid cylinder

Where $N=\frac{n}{L}$, (X_o,Y_o) : the center of cylinder.

The average Nusselt number at the heated wall is calculated by[11]:

$$Nu_{av}=\int_0^1-\left(\frac{\partial\theta}{\partial Y}\right)_{Y=0}dX$$

(5)

And the bulk average temperature is defined as:

$$\theta_{av}=\int\frac{\theta\,d\overline{V}}{\overline{V}}$$

(6)

Where $\overline{V}$: the volume of occupying fluid in square enclosure.

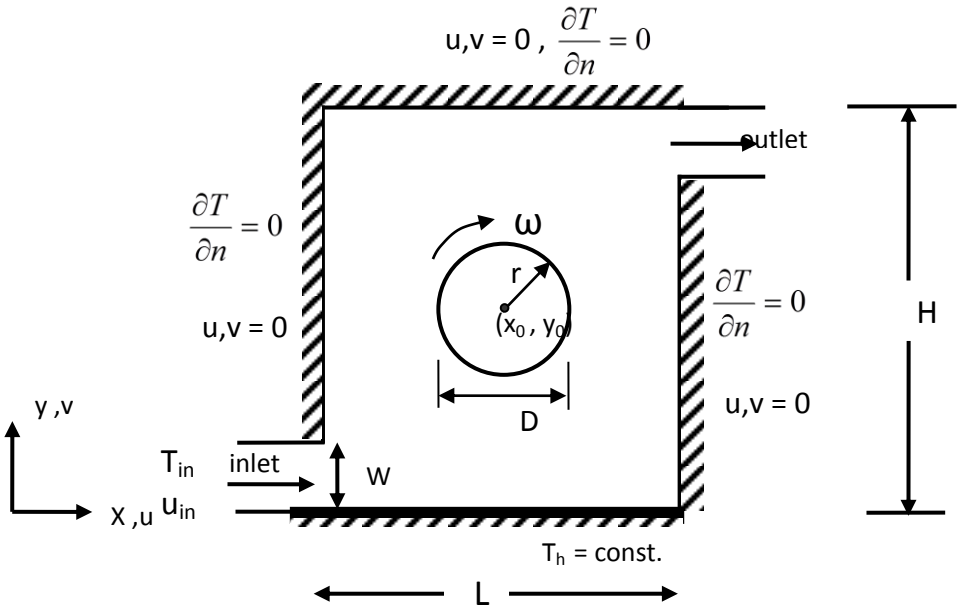

Fig.1: Sketch of the physical model and boundary condition

3. Numerical Solution :

The governing equations (1) to (4) and the associated boundary conditions are solved numerically by finite element method using software package Flex PDE [12]. The continuity equation (1) is to be used as a constraint due to mass conservation and this constraint may be used to obtain the pressure distribution [13]. In order to solve the equations (2) to (4), we use a penalty parameter and the compressibility criterion by equation (1) which results in:

$$\nabla^2 P = \gamma\left(\frac{\partial U}{\partial X} + \frac{\partial V}{\partial Y}\right) \quad (7)$$

γ is a penalty parameter that should be chosen either from physical knowledge or by other means [14]. A most convenient value for γ was attained in this study to be (10^{11} μ / L^2). The numerical solutions are obtained in terms of U- velocity, V- velocity and isotherms lines. The heat transfer coefficient in terms of average nusselt number along the heated surface (bottom wall) is obtained $Nu_{av} = = \int_0^1 -\left(\frac{\partial \theta}{\partial Y}\right)_{Y=0} dX$. Also, the bulk temperature is calculated from the relation $\theta_{av} = \int \frac{\theta \, d\bar{V}}{\bar{V}}$.

4. Validation and Comparison of The Study :

Geometry studied in this paper is an obstructed ventilated cavity; therefore several grid size sensitivity tests together with continuity equation ($\frac{\partial U}{\partial X}+\frac{\partial V}{\partial Y}=0$) and obtained results showed an exactly validation of the velocity distribution for grid size obtained by imposing an accuracy of 10^{-3}. This accuracy is a compromised value between the result accuracy and the time consumed in each run. The grid domain for Ri = 1, Re = 50 is shown in (**Fig. 2-a**) and the distribution of $(\frac{\partial U}{\partial X}+\frac{\partial V}{\partial Y})$ over the domain is presented in (**Fig. 2-b**) .

.

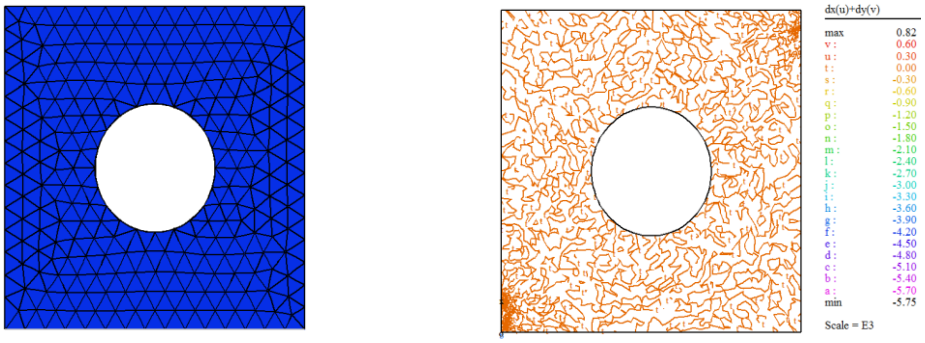

(a) **(b)**

Fig.2: (a) grid distribution over the domain (b) validation of continuity equation.

From the previous researches in the review, we could not be found research for mixed convection with rotating inner cylinder, therefore, to satisfy this a some reported data of Nu_{av} for the present work of mixed convection in square enclosure with stationary heated concentric cylinder are compared with work [10] as shown in table -1 which referred to the comparison of the present values of θ_{av} (second column) with the values of reference [10] (third column) at difference values of Ri. It is obvious that good agreement is obtained. As a result, the confidence in the present numerical solution is enhanced.

5. Results and Discussion :

The numerical results are represented by the isotherms lines , V-velocity, U-velocity, Nu_{av} and average temperature. The working fluid is air at Pr = 0.7. The

ranges of the studied parameters are: Ri = 0-10 , Re = 20-100 , R = 0-0.3 and Ω = 0-3. **Fig. 3.** shows the effect of variation of radius of the rotational cylinder on V-velocity (left), U-velocity (middle) and isotherms (right) for Re = 50, Ri = 1, Pr = 0.7 and Ω = 1. The values of V-velocity and U-velocity are increased with increasing of R this is because of dominant the forced convection with reducing the region of the flow. It can be seen from the isotherms curves at R = 0 the growth of the thermal boundary layer is increased in the flow direction near the heated wall. As the radius of the inner cylinder is increased, this make a parallel lines of the isotherms which are covered the space between the inner cylinder wall and the surface of the vertical right wall of the enclosure. **Fig. 4.** shows the effect of the variation of rotational velocity Ω on V-velocity (left), U-velocity (middle) and isotherms (right) for Re = 50, Ri = 1, Pr = 0.7 and R = 0.2. The magnitude of V-velocity and U-velocity increases with increasing Ω because of the effect of the flow circulation. Also, this figure shows that the decrease in the growth of thermal boundary layer in the space between the cylinder and variation right wall increasing Ω. **Fig. 5.** shows the influence of Re number on V-velocity (left), U-velocity (middle) and isotherms (right) for Ri = 1, Pr = 0.7, Ω = 1 and R = 0.2. Both U- and V- velocities are increased with increasing Re number. From this figure, it can be seen that the growth of the thermal boundary layer is increased along the bottom wall of the enclosure. **Fig. 6.** shows the effect of variation of Ri number on V-velocity, U-velocity and isotherms for Re = 50, Ω = 1, Pr = 0.7 and R=0.2. This figure shows a plum like distribution of U- velocity & V-velocity at the inlet of the enclosure, it can be seen that the increase in Ri lead to increasing the values of U&V velocities. The temperature difference in the enclosure is increased with increasing of Ri due to the effect of the bouncy.

Fig. 7. (a) shows the effect of Ri number variation on Nu_{av} for Re = 50, Pr = 0.7, Ω = 1 and R = 0.2. As can be show the Nu_{av} is increased gradually with increasing of Ri number. This increments approximately linear due to the buoyancy effect. **Fig. 7. (b)** show the variation effect of Ri number on the average non dimensional temperature θ_{av} . Also, the value of θ_{av} is increased with increasing of Ri and the trend of the curve is the same as that in Fig. 7.(a). The effect of cylinder radius on Nu_{av} for Ri=1, Pr = 0.7, Ω = 1 and Re = 50 is shown in **Fig. 8. (a)**. It can be seen that, Nu_{av} increases linearly with increasing of cylinder radius due to the dominate of mixed convection with decreasing the cavity cross area. **Fig. 8. (b)** illustrate the

variation of θ_{av} with cylinder radius for Ri = 1, Pr = 0.7, Ω = 1 and Re = 50. It can be observed that a small increases of θ_{av} with increasing of cylinder radius value from 0 to 0.15, this is may be attributed to the small effect of the secondary flow. When R > 0.15, it can be seen a deep variation of θ_{av} with R due to the decreases of the cavity cross section area which lead to increases the heat transfer process. **Fig. 9. (a)** shows the variation of Nu_{av} with rotational, it observed that the maximum value of Nu_{av} occurs at the range of Ω from 0 to 0.7 and then decreasing with increasing of rotational speed Ω. This is because of reducing the effect of the secondary flow on the heat transfer process with increasing of Ω. **Fig. 9. (b)** indicates the increasing of θ_{av} with increasing of Ω. **Fig. 10. (a)** shows the variation of Nu_{av} with Re. It can be seen that the value of Nu_{av} is increased with increasing of Re number due to dominate of forced convection. **Fig. 10. (b)** show the effect of Re on θ_{av}**.** The increment of Re number gives increment in the mass and final decreasing in the temperature.

6. Conclusions :

The governing equations (mass, momentum and energy) for the steady, laminar, two dimensional, incompressible flow with Boussinseq approximation and constant fluid properties for rotating single cylinder in vented square enclosure are solved numerically using finite element method with FlexPDE soft package. The main conclusions:

1-The average Nusselt number is increased with increasing Re, Ri and R and decreasing with increasing of the rotational velocity Ω.

2-When the angular rotating velocity equal to zero the behavior becomes of natural convection only.

3- The average temperature increases with Ri , R and Ω and decreases with Re.

Table -1. Comparison of the average temperature at different value of Ri with Abood et al. [10] at Pr = 0.71, Re = 100 and without rotation .

Ri	$\theta_{av.}$ present	$\theta_{av.}$ Ref.[10]
0	0.528	0.527
2	0.584	0.585
6	0.601	0.601
10	0.612	0.612
12	0.615	0.616

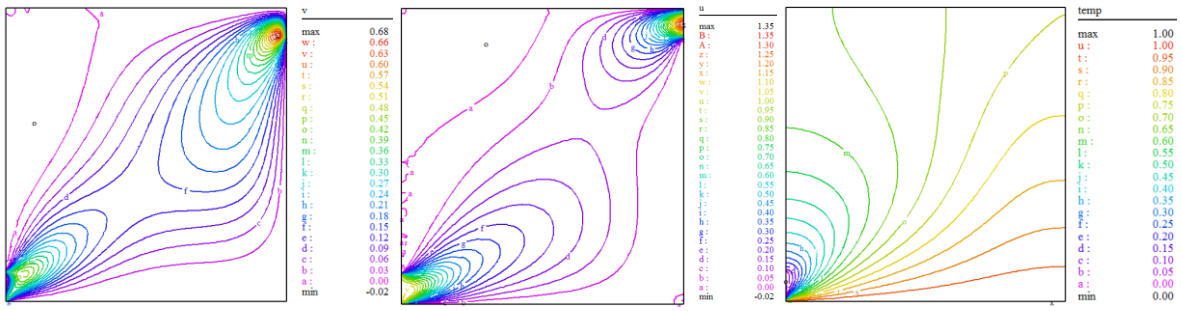

(a)

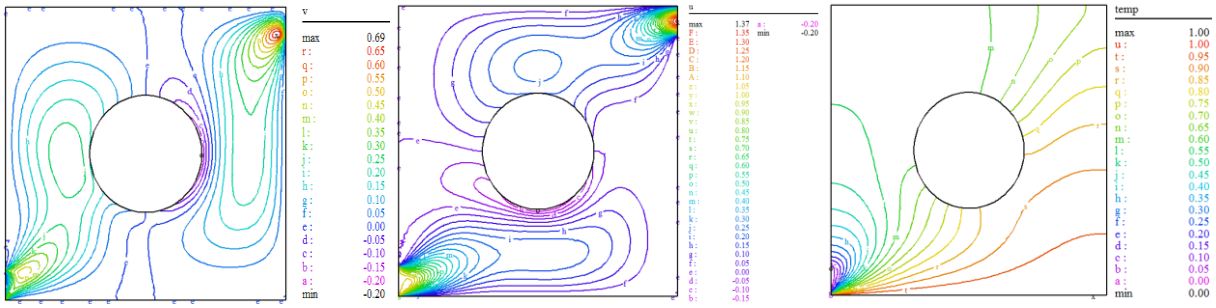

(b)

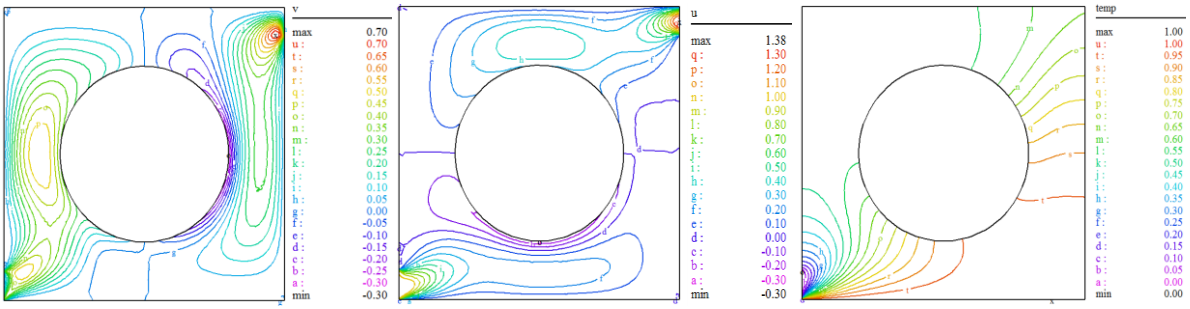

(c)

Fig.3. V-velocity (left), U-velocity (middle) and isotherms (right) for Ri=1, Re=50 and Ω=1 at (a) R=0 (b) R= 0.2 (c) R=0.3.

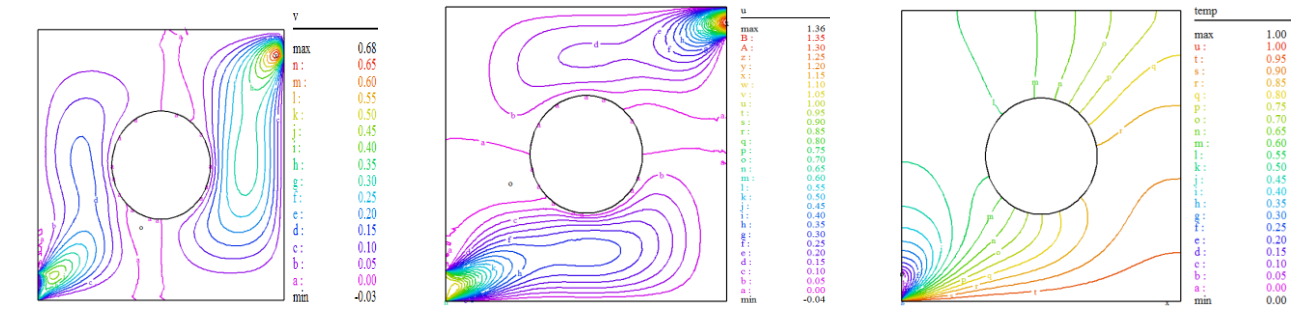

(a)

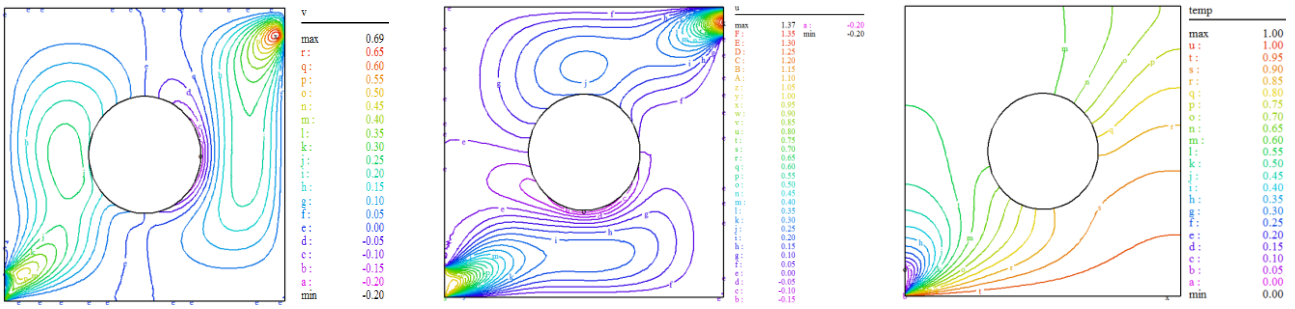

(b)

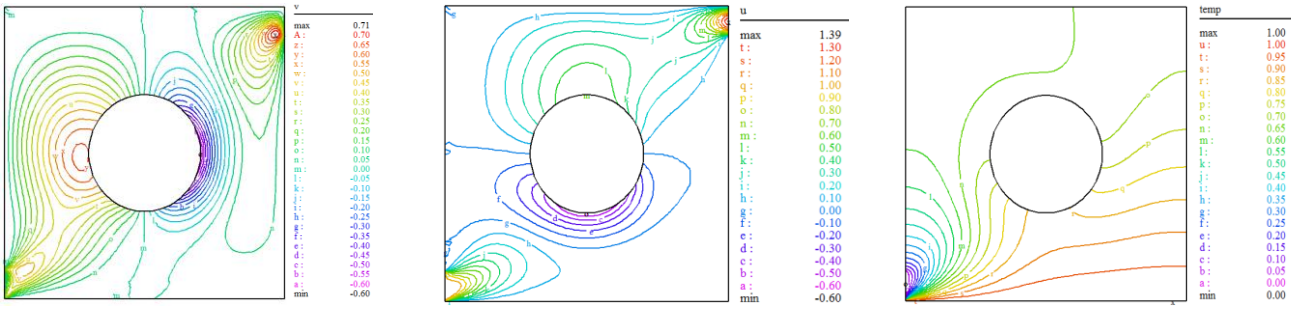

(c) Fig.4. V-velocity (left), U-velocity (middle) and isotherms (right) for Ri=1, Re=50 and R=0.2 at (a) Ω=0 (b) Ω=1 (c) Ω=3.

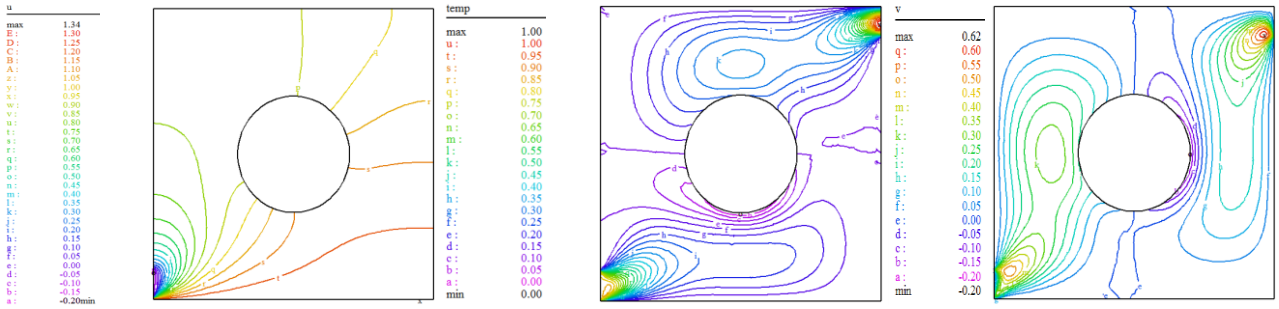

(a)

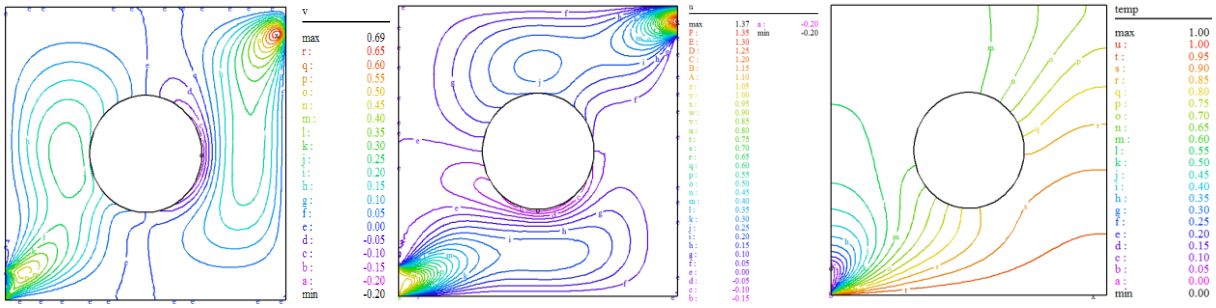

(b)

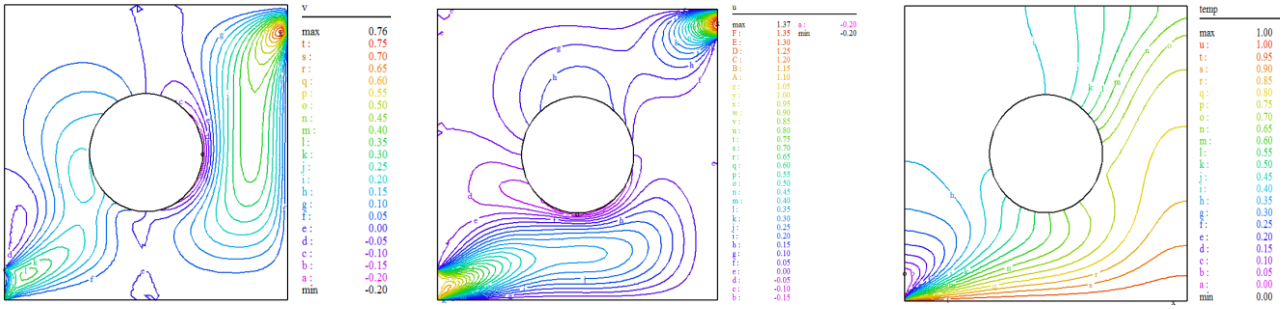

(c)

Fig.5. V-velocity (left), U-velocity (middle) and isotherms (right) for Ri=1, Ω=1 and R=0.2 at (a) Re=20 (b) Re=50 (c) Re=100.

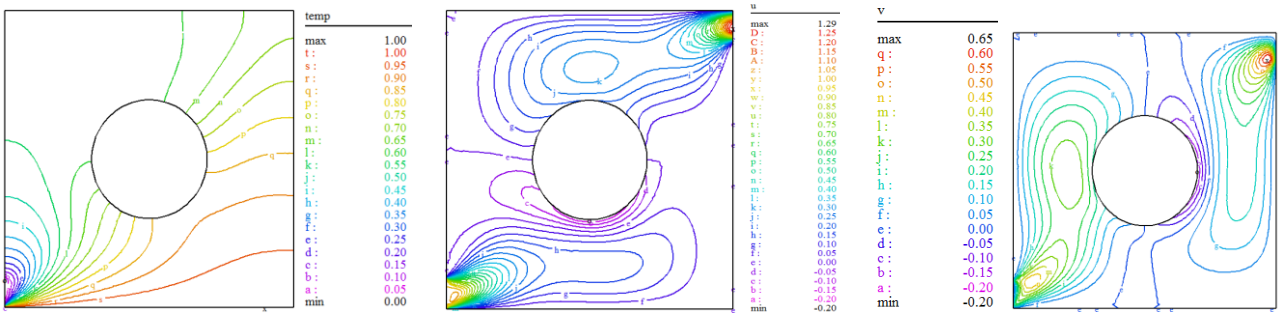

(a)

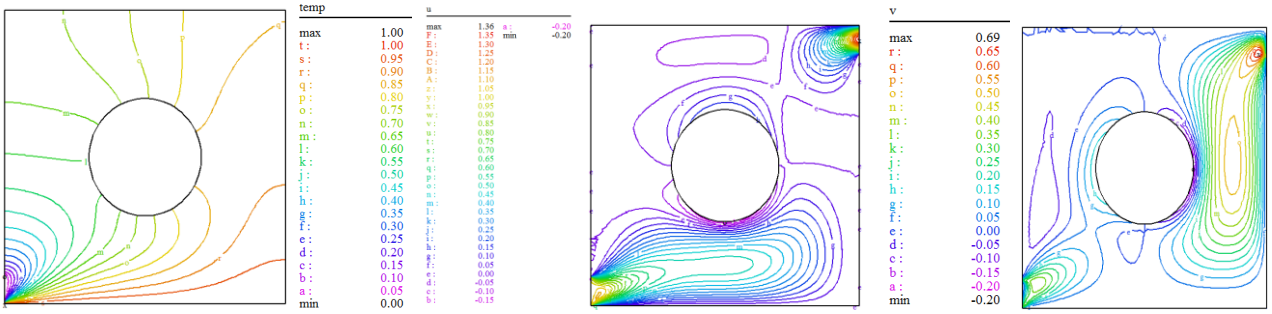

(b)

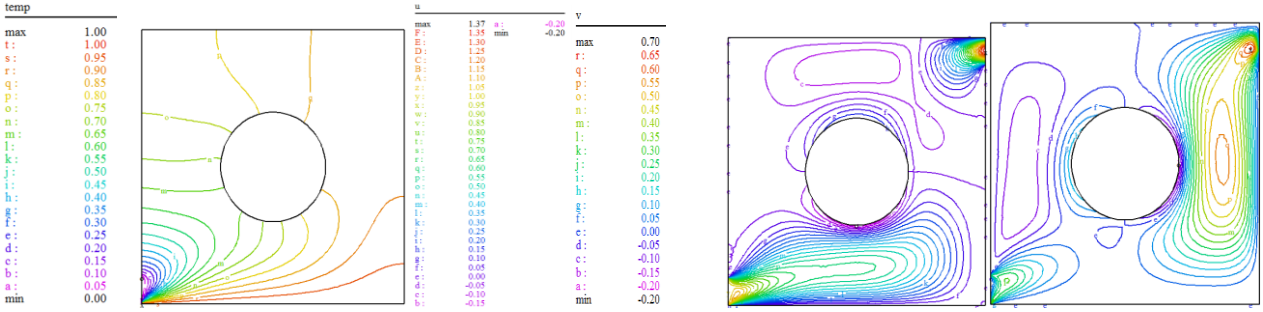

(c)

Fig.6. V-velocity (left), U-velocity (middle) and isotherms (right) for Re=50,Ω=1 and R=0.2 at (a) Ri=0 (b) Ri=6 (c) Ri=10.

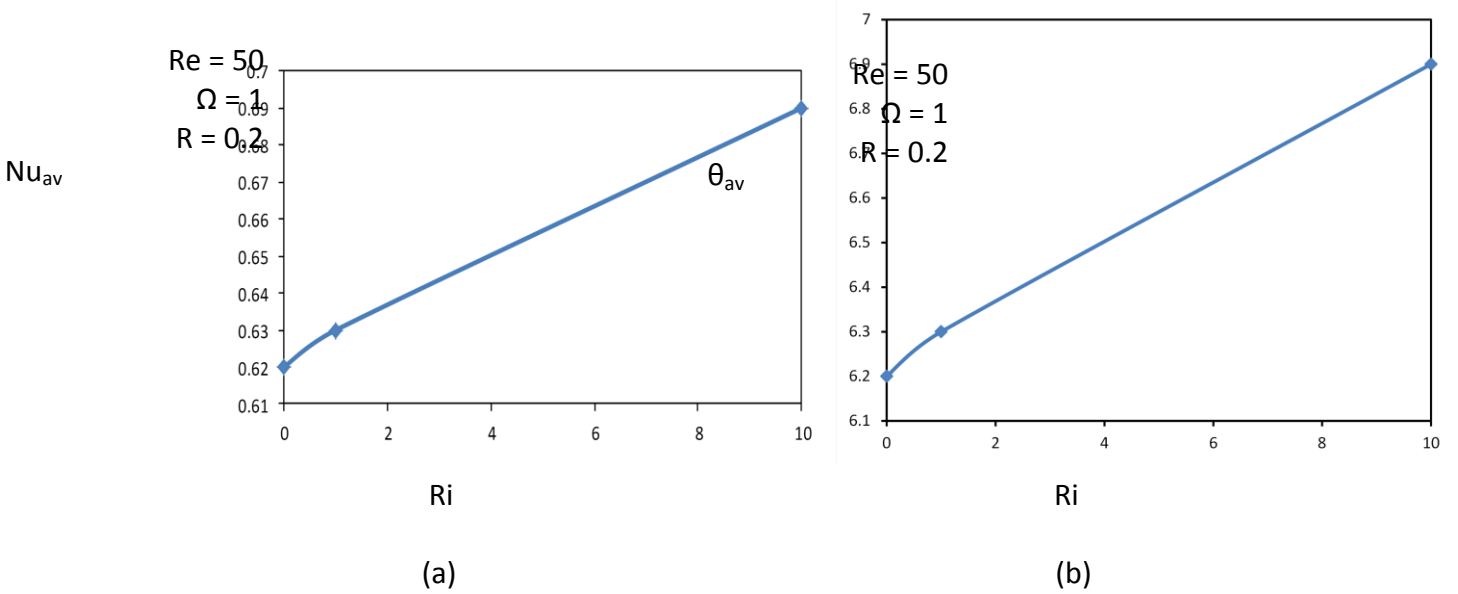

(a) (b)

Fig. 7. (a) Variation of the Nusselt number with Richardson number (b) Variation of the average dimensionless temperature with Richardson number.

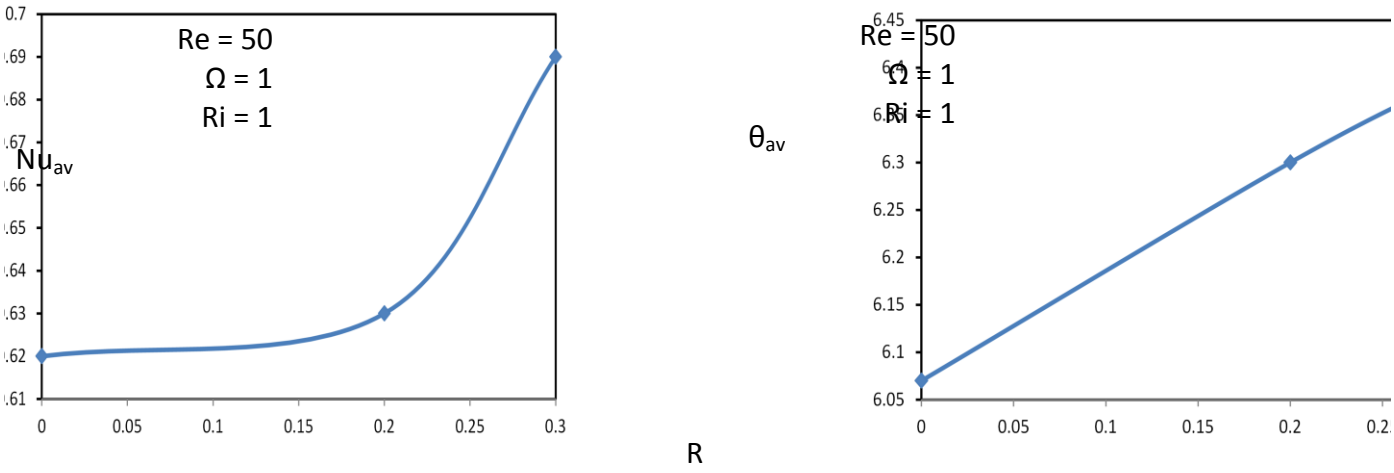

(a) (b)

Fig. 8. (a) Variation of the Nusselt number with radius cylinder (b) Variation of the average dimensionless temperature with radius of cylinder.

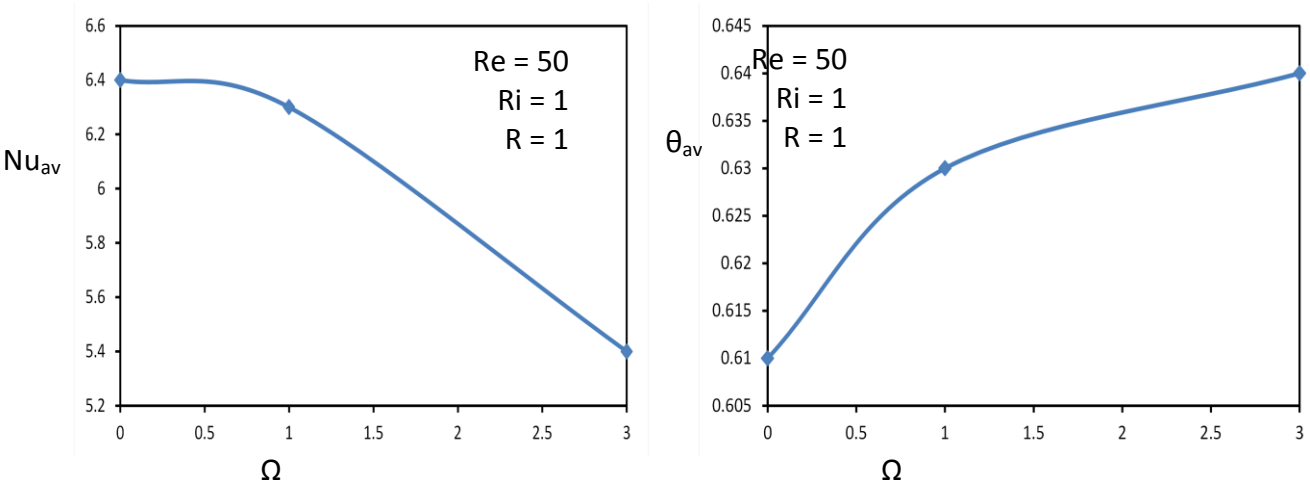

(a) (b)

Fig. 9. (a) Variation of the Nusselt number with rotational velocity (b) Variation of the average dimensionless temperature with rotational velocity.

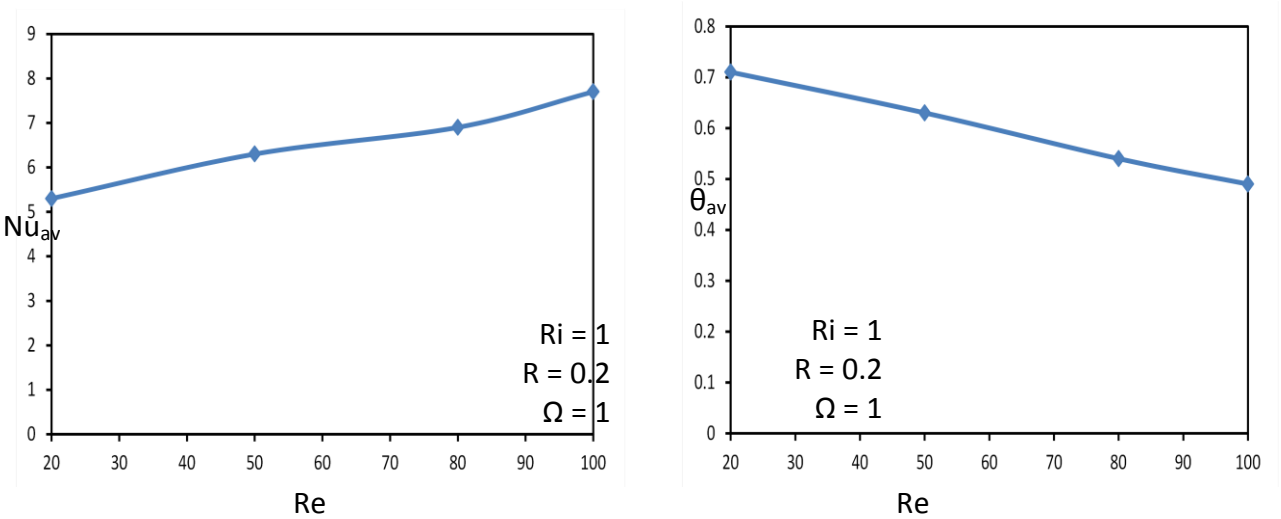

(a) (b)

Fig. 10. (a) Variation of the Nusselt number with Reynolds number (b) Variation of the average dimensionless temperature with Reynolds number.

7. References:

[1] Rahman, M. M., Alim, M. A., Mamun, M. A. H., Chowdhury M. K. and Islam A. K. M. S., 2007, "Numerical study of opposing mixed convection in a vented enclosure", ARBN Journal of engineering and Applied Sciences, Vol. 2, No.2, PP. 25-36.

[2] Shung Fu , Cheng S.H. and Shine W. J., 1994, " Enhancement of natural convection heat transfer of an enclosure by a rotating circular cylinder ",Int. J.Heat and Mass Transfer, Vol. 37, No.13, PP. 1885-1897.

[3] Khanafar K., Vafai K. and Lightstone M., 2002 " Mixed convection heat transfer in teo - dimenshonal open-ended enclosures" , Int. J. Heat and Mass Transfer, 45,PP.5171-5190.

[4] Lasode A. O. 2007, " Mixed convection heat transfer in rotating vertical elliptic ducts" ABCM J. of the Braz. Soc. Mech. Sci. & Eng. Vol. XXIX, No.2, PP. 142-151.

[5] Kim, B. S., Lee, D. S., Ha, M. Y., Yoon, H. S., 2008, " A numerical study of natural convection in a square enclosure with a circular cylinder at different vertical locations" Int. J. Heat and Mass Transfer, 51, PP. 1888-1906.

[6] Rahman, M. M., Elias M. and Ali M. A., 2009, " Mixed convection flow in a rectangular vented cavity with a heat conducting square cylinder at the center " ARBN Journal of engineering and Applied Sciences, Vol. 4, No.5, PP. 1819-6608.

[7] Costa V. A.F., Raimundo, A.M., 2010, " Steady mixed convection in a differentially heated square enclosure with an active rotating circular cylinder" Int. J. Heat and Mass Transfer, 53, PP. 1208-1219.

[8] Saha S., Saha G. and Hasan N. , 2010, " Mixed convection in a lid-driven cavity with internal heat source " Annual Paper Meet,13, PP.1-6.

[9] Lee J. M. , Ha M. Y. and Yoon H.S. , 2010, " Natural convection in a square enclosure with cylinder at different horizontal and diagonal locations" Int. J. Heat and Mass Transfer, 35, PP.5905-5919.

[10] Abood F. A., Shrama S. M. and Radhi Z. K., 2011, "Study of mixed convection heat transfer inside a vented square cavity with inner heated cylinder "Thi-Qar university Journal for engineering Sciences ,Vol. 2,No.3, PP. 113-130.

[11] Alshara A. K.M. , 2012, " Effect of single or multi rotating horizntal cylinder on the mixed convection heat transfer inside a triangular enclosure" Al-Qadisiya Journal for Engineering Sciences, Vol. 5, No. 1, PP. 95-110.

[12] Gunor Backstrom, 2005, "Field of physics by finite element analysis using Flex PDE " GB Publishing and Gunner Backstrom Malmo, Sweedn.

[13] Roy S. and Basak T., 2005, " Finite element analysis of natural convection flows in square cavity with non uniformly heated wall" Int. J. Eng. Sci., 43, 668-680.

[14] Wu W. and Ching C. Y. , 2009, " The effect of the top wall temperature on the laminar natural convection in rectangular cavities with different aspect ratio " J. Heat transfer ",131, 1-11.

8. Nomenclature

D	Diameter of rotating cylinder, m
g	Acceleration due to gravity, m/s^2
H	Height of square enclosure , m
k	Thermal conductivity , $W/m^2.K$
L	Length of the heated wall , m
N	Non-dimensional normal distance
Nu	Nusselt number
Nu_{av}	Average Nusselt number
P^*	Dimensionless pressure, $p/\rho u_{in}^2$
Pr	Prandtl number, υ/α
R	Dimensionless radius of the rotating cylinder, r/L
Ri	Richardson number,Gr/Re^2
Re	Reynolds number, $u_{in} L/\upsilon$
T	Temperature of the fluid in the enclosure, K
U,V	Non-dimensional velocity components , u/u_{in} , v/u_{in}
w	Height of inlet opening, 0.1 L
W	Non-dimensional height of inlet opening, w/L
X,Y	Non-dimensional coordinates, X=x/L, Y=y/L
Greek Symbols	
α	Thermal diffusivity of fluid, m^2/s
β	Thermal expansion coefficient, K^{-1}
θ	Dimensionless temperature, $\theta=(T-T_{in})/(T_h-T_{in})$

υ	Kinematics viscosity, m^2/s
ρ	Density , kg/m^3
ω	Angular rotational velocity of solid cylinder , rad/s
Ω	dimensionless angular rotational velocity, $\omega R/u_{in}$
Subscripts	
h	Hot
in	Inlet

Interface of Microcontroller Implementation of Voice Recognition for Person Authentication

Asst. Lecturer Wail Ibrahim Khalil

الخلاصة

تم استخدام النبرات الصوتية في بحثنا هذا لغرض إعطاء التخويل. والسبب في استخدام نبرة الصوت ذلك لان خصائص صوت الانسان ممكن تحليلها والتعرف عليها بشكل سهل، بالاضافة الى ذلك استخدام نبرة الصوت تعطي المرونة في استخدامها في انظمة السيطرة وغيرها. في هذا البحث استخدم برنامج التعرف على نبرات الصوتية وكذلك تم تصميم دائرة الكترونية تحتوي على مسيطر دقيق لغرض عرض النتائج عن عملية التطابق على الشاشة. وهذا النوع من العمل قادر على تشخيص النبرات الصوتية بعد عملية التعليم للشخص الجديد وحفظ هذه النبرات الصوتية في قاعدة بياناته وبالتالي تنفذ لتعطي رسالة الى منفذ الاخراج ومنه يمكن ايضاً السيطرة على فتح الابواب لغرض اعطاء صلاحية الولوج للشخص المخول بالدخول وبنفس الوقت اشعار المراقب بمعلومات الشخص المخول. تم تصميم نظام يحتوي على برنامج تشخيص الصوت وكذلك دائرة الكترونية تحتوي على مسيطرة AT89S52 مع شاشة عرض LCD، وتم تدريب الايعازات للاشخاص لغرض التعرف واعطاء الاخراج الصحيح.

Abstract

Voice is used in this proposed for the authentication and display information of registered person and find whom is authorized to be access or not. The reason for choosing voice of human because is considered part of biometric system method and is easily being reproduced by human. Besides that, usage of voice gives control system that be effective and convenient to be used. This proposed involve a simple system that consists of voice recognition software and AT89S52 microcontroller with LCD to build up the system. This work is able to recognize the command trained by the user and successfully gives the correct output.

Keywords: voice recognition, Fourier Transform, Microcontroller AT89S52

1.Introduction

The data generated from voice signals are captured by a microphone attached to a PC. Signal generated by speech is an analogue signal, which must be digitized at a certain frequency. Typically, most moderate grade microphones employed have a sampling rate of approximately 32 kHz. So a 32 kHz sampling rate is generally more than sufficient for human voice patterns [1].

For reliable signal acquisition of voice data, the frequency and amplitude of the signal must be acquired with high fidelity. This is an issue with speakers with a

large high frequency component, such as women and children. Typically, most modern recording devices are capable of digitizing voice data at 16 bits or more, providing more than sufficient dynamic range to cover human speech patterns [1].

In a speaker-independent system, the user's voice pattern is analyzed and compared to all other voice samples in the user database. There are a number of ways this comparison is made regarding the voice samples and these details are provided via closest match to the voice data presented for identification of the speaker. There are three possible outcomes: i) The speaker is correctly identified; ii) the speaker is incorrectly identified as another speaker; or iii) the speaker is not identified as being a member of the system. Clearly, the last two possibilities will avoid, which reflect the false acceptance rate (FAR) (type II error) and the False Rejection Rate (FRR) as much as possible [8]. When speakers attempt an authentication task, the speakers have provided some evidence of their identity, and the purpose of the voice recognition process is to verify that these persons have a legitimate claim to that identity. The result of this approach is a binary decision: either the person is verified as the claimed identity or not, and when be verified a message from voice software will be managed and sent to device plugged to PC via serial port and this device contains the microcontroller and LCD which shows the name of person whom authorized to access or any other issues could be implemented of this work [9].

As shown in figure (1) the block diagram of the proposed system, the first step is the capture the voice signal via microphone and this signal is an analogue form which need to be converted to a digital form by using Fourier Transform used to denoising a signal[5].

The frequency domain is used for noise reduction and echo cancellation of the voice signal. The system implemented in frequency domain and fourier transform to split frequency sampling[6].

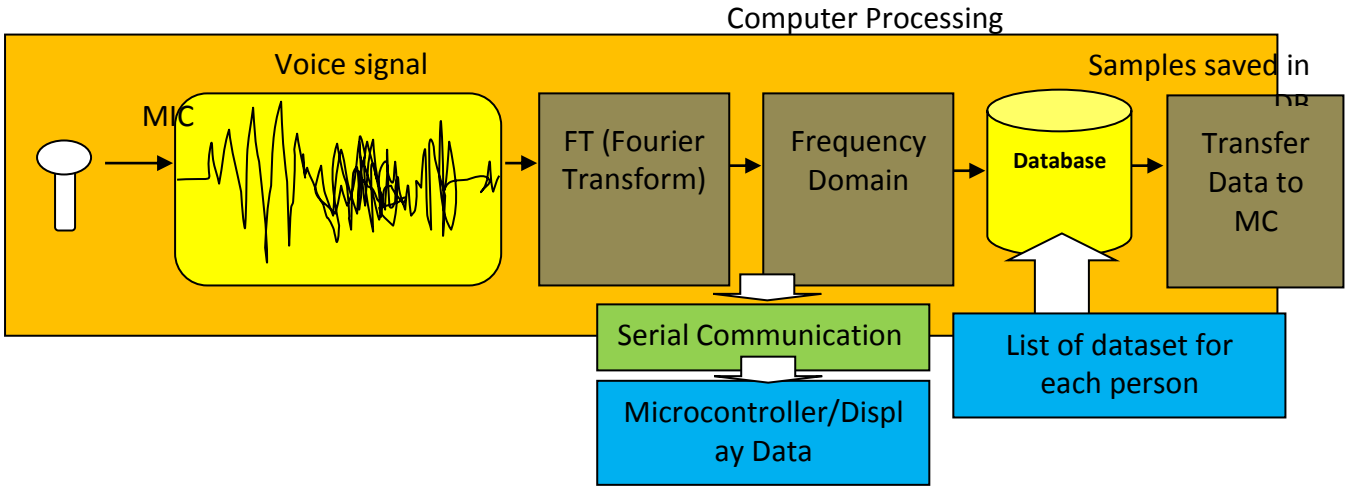

Figure 1. Block diagram of proposed work

2.Feature Extraction

The basis of most feature extraction approaches is the observation, that the speech spectrum shape encodes significant information about the speaker's vocal tract. This appears to be mainly the case due to two reasons[2].

First, the human vocal tract forms a resonator and second, the glottis is a source of pitch harmonics. Consequently, most feature extraction approaches aim at extracting spectrum-based features and typical method for extracting first-order features is Fourier Transformation (FT). Based on these first-order spectra, many approaches compute higher order cepstral features, such as Mel-Frequency Cepstral Coefficients (MFCC). Cepstral analysis is based on the idea of inverse transforming the logarithmic spectrum from frequency to temporal domain, thus the cepstrum of a signal can be defined as the Inverse FT (IFT) of the logarithm of the FT of the original signal[2].

Spectral or cepstrum features are extracted for temporal subsections of the entire audio signal, called windows. These windows are usually shifted sequentially over the entire signal and are characterized by a window size (in milliseconds, ms) and a window-to-window offset in milliseconds. Figure 1., illustrates this typical feature extraction process for voice biometrics which proposed work, starting from the output signal on the left and leading to the person displayed name on LCD representation on the right.

Note that in this illustration, no preprocessing is included. However, in many practical systems, such preprocessing includes techniques like filters for reducing

background noises or other methods for emphasizing those signals that are relevant for biometric features. These filters are typically implemented as transfer functions in frequency domain[2].

3.Comparison and Classifications

The feature factor has extracted from phase of feature extraction of both stages (trained and recognition), mainly two different models are used in speech biometrics: template models and stochastic models. In the first category, cumulated distances are calculated between the features of the actual test sample and the stored reference features in database as stream with the name of person. Based on such distance values, the verification process can be implemented, for example, simply as a threshold-based decision function whereby the distance between reference and sample may not exceed a given threshold value. For that in this research the threshold value range is +/-10 has been chosen[2].

4.Voice Authentication

The voice authentication recognized the user's particular word or phrase. The voice scanners can have a problem with false non-matching, failing to authenticate a known user, but they tend to be resistant to false matching, so impostors are unlikely to be authenticated. Voice biometrics are a numerical model of the sound, pattern and rhythm of an individual's voice. A voice biometric or 'voice print' is unique to an individual [3].

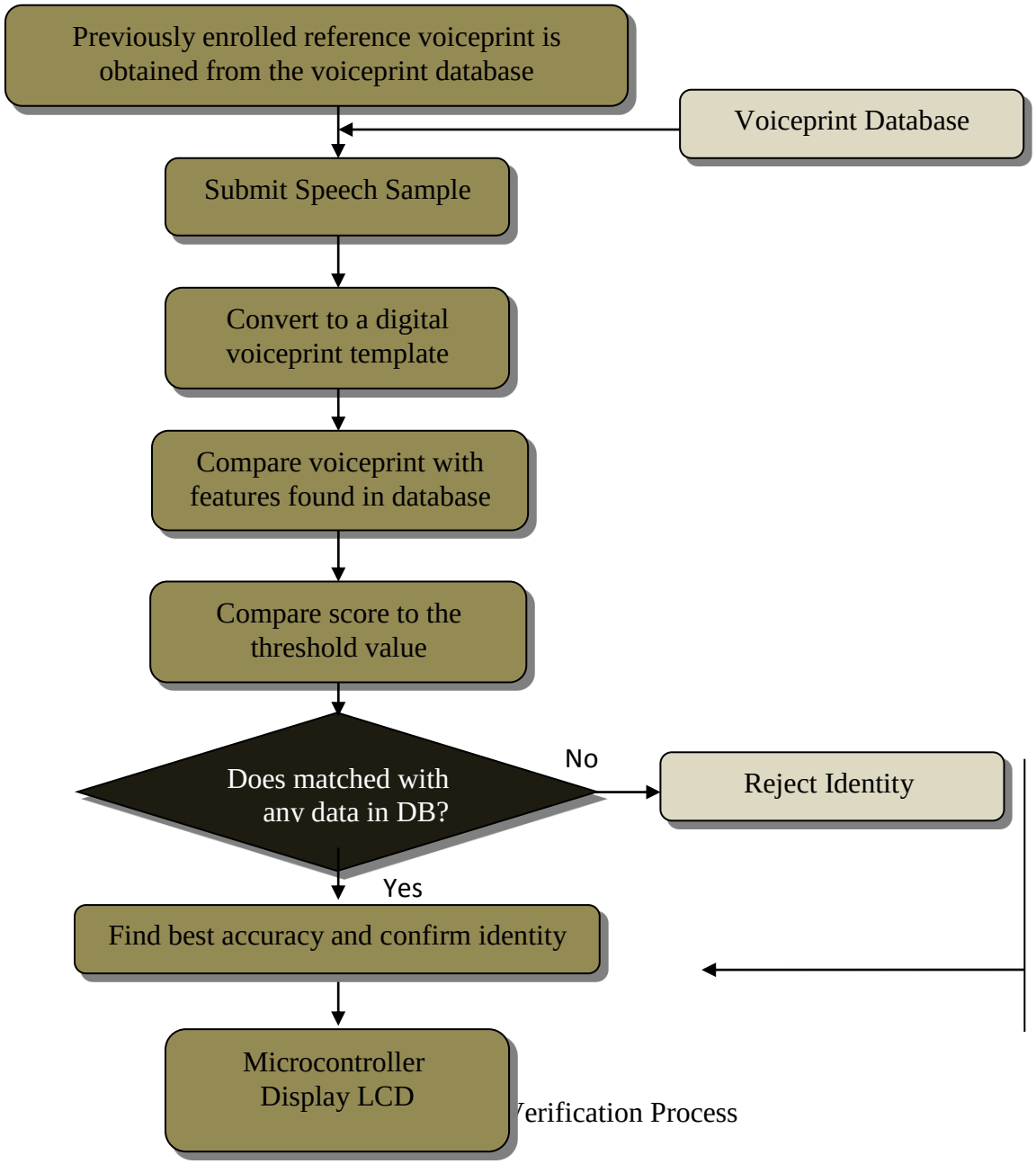

erification Process

5.Frequency Domain Interpretation of the Short-Time Fourier Transform

The short-time Fourier transform of the sequence s(m) is defined as

$$S_n(e^{jw_i}) = \sum_m s(m)w(n-m)e^{-jw_i m} \dots\dots (1)$$

if take the point of view that are evaluating$S_n(e^{jw_i})$ for a fixed n=n_0, then we can interpret eq.1

$$S_n(e^{jw_i}) = FT[s(m)w(n_0-m)]|_{w=w_i} \dots\dots (2)$$

where FT denotes the Fourier Transform. Thus $S_n(e^{jw_i})$ is the conventional Fourier transform of the windowed signal, $s(m)w(n_0-m)$, evaluated at the frequency w=w_i. Figure (3).illustrates the singals s(m) and w(n-m), at times n=n_0=50, 100, and 200 to show which parts of s(m) are used in the computation of the short-time Fourier transform. Since w(m) is an FIR filter, if we demote that size by L, then using the conventional Fourier transform interpretation of $S_n(e^{jw_i})$, then can state the following[4]:

1. If L is large, relative to the signal periodicity (pitch), then $S_n(e^{jw_i})$ gives good frequency resolution. That is, then can resolve individual pitch harmonics but only roughly see the overall spectral envelope of the section of speech within the window[4].

2. If L is small relative to the signal periodicity, then $S_n(e^{jw_i})$gives poor freuqency resolution (i.e., no pitch harmonics are resolved), but a good estimate of the gross spectral shape is obtained[4].

To illustrate these points, Figure (4) show examples of windows signals, $s(m)w(n_0-m)$, (part a of each figure) and the resulting log magnitude short time spectra, 20 $\log_{10}|S_n(e^{jw_i})|$ (part b of each figure). Figure 4 shows result for an L =500 point Hamming window applied to a section of voiced speech. The periodicity of the singal is clearly seen in the windows time waveform, as well as in the short-time spectrum in which the fundamental frequency and its harmonics show up as narrow peaks at equally spaced frequencies. Figure 5 shows a similar set of comparisons for an L=50 point Hamming window. For each short windows, the time sequences$(m)w(n_0-m)$ does not show the signal peridicity, nor does the signal

spectrum. In fact, what we see in the short-time Fourier transform log magnitude is a few rather broad peaks in freuqency corresponding roughly to the speech formants[4].

Figures (3) and (4) show the effect of using windows on a section of unvoiced speech (corresponding to the fricative /sh/) for an L=500 sample window (Figure 3) and L=50 sample window (figure 4). Since there is no periodicity in the signal, the resulting short-time spectral magnitude of Figure 4, for the L=500 sample window shows a ragged series of local peaks and valleys due to the random nature of the unvoiced speech. Using the shorter window smoothes out the random fluctuations in the short-time spectral magnitude and again shows the broad spectral envelope very well.

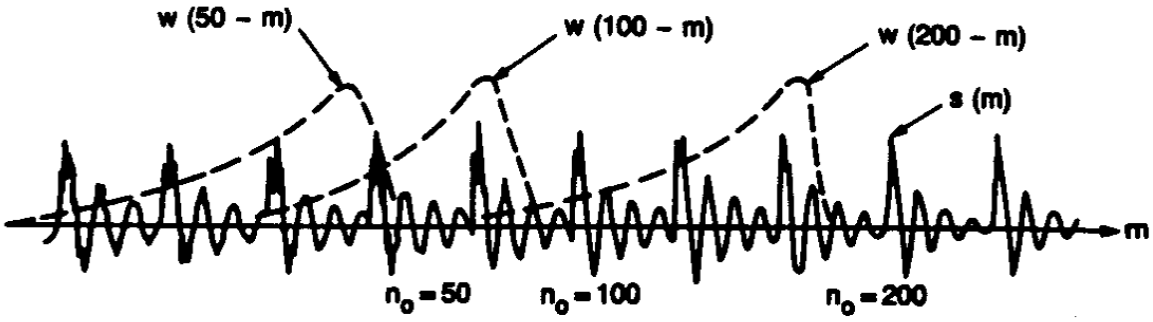

Figure (3) The signals s(m) and w(n-m) used in evaluation of the short-time Fourier transform [4]

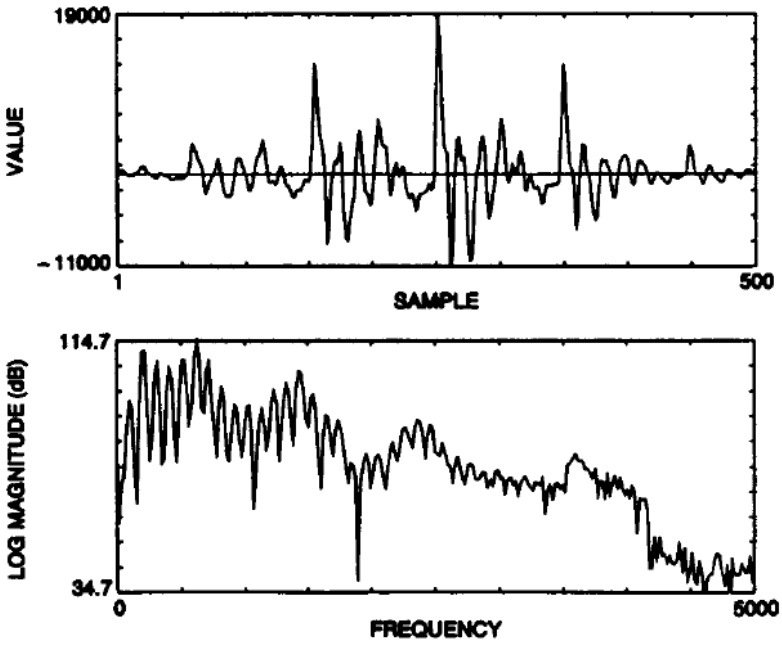

Figure (4) Short-time Fourier transform using a long (500 points or 50 msec) Hamming window on a section of voiced speech[4]

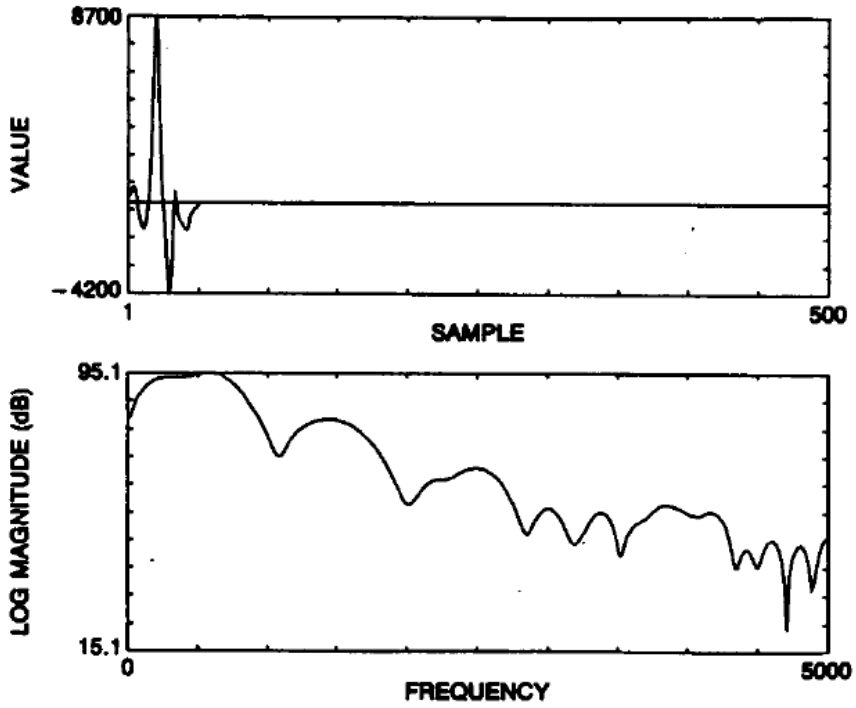

Figure (5) Short-time Fourier transform using a long (50 points or 5 msec) Hamming window on a section of voiced speech[4]

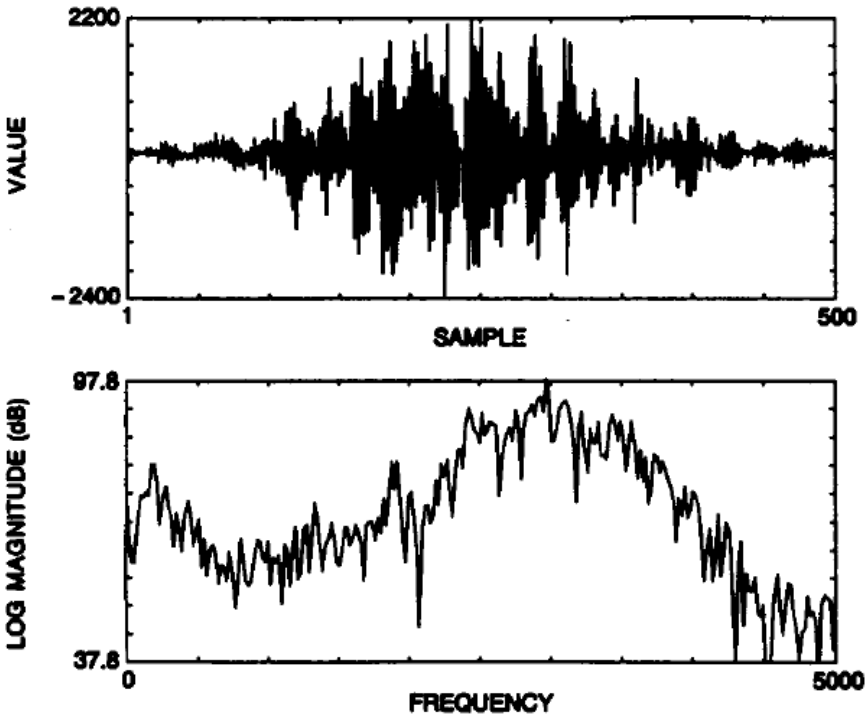

Figure (6) Short-time Fourier transform using a long (500 points or 50 msec) Hamming window on a section of unvoiced speech[4]

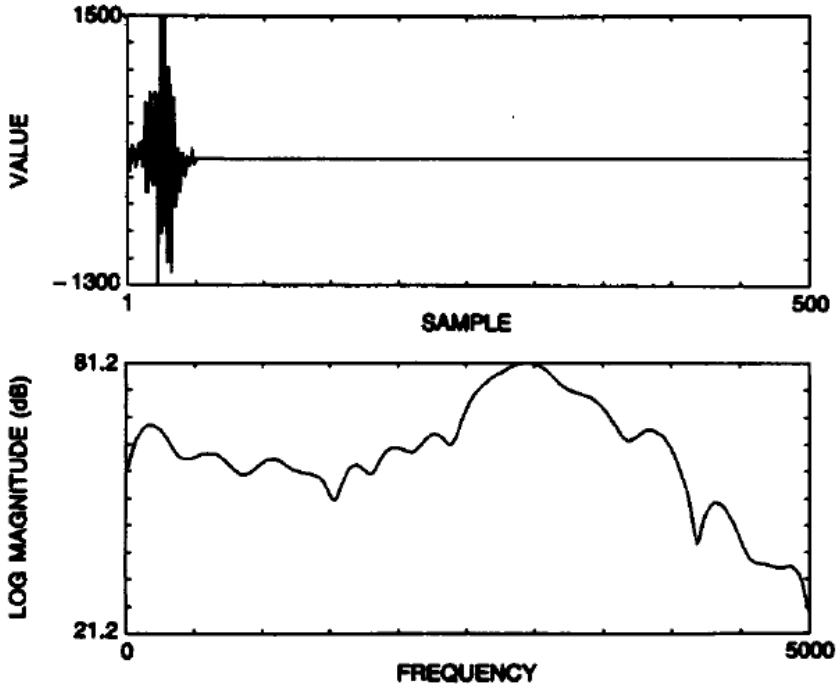

Figure (7) Short-time Fourier transform using a long (50 points or 5 msec) Hamming window on a section of unvoiced speech[4]

6.Hardware

In this work, after the voice recognized and matched with one found in database, the data will get from this database (Microsoft Access file) the name and send this data to microcontroller via RS232 port, and will display the information on LCD. The design of hardware is contains the main part which is microcontroller 8051 family (AT89s52), and the LCD 16*2 to display the name of person whom just record his/her voice, when then the system will allowed to an authenticator whom just sign in by his/her voice to be allowed to access. The purposed of using microcontroller gives benefits in many fields such security access in government and private sectors, controlling devices based on authorized person, person identification system, and in communication purposes. The database which has been used in this system is MS Office Access has limited of records reach to 32,600. The schematic circuit of the design hardware is shown in Figure (8).

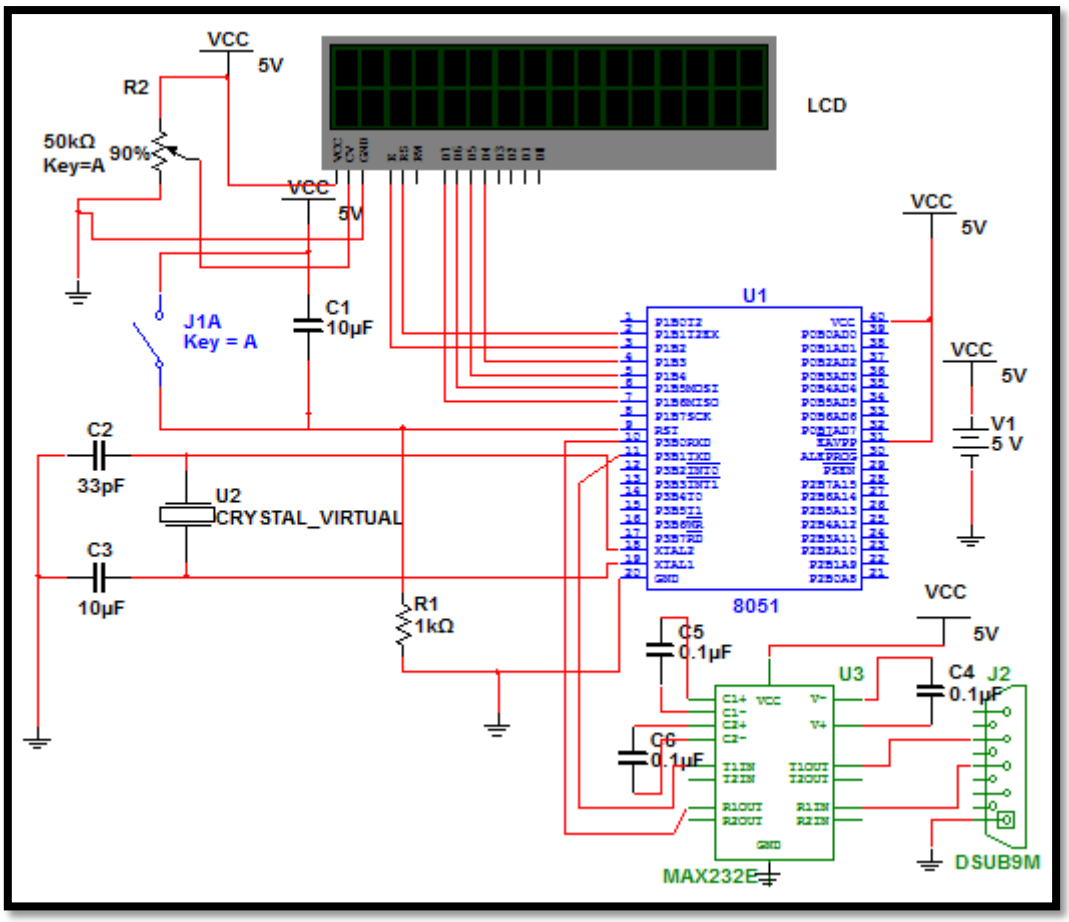

Figure (8) Schematic Circuit Design of Proposed System

7.Results

The proposed work includes software and hardware, and in the section below will be discussed in the procedure of the work.

Each person can be registered with his voice, and for each person has a number of samples found in database which gives more accuracy in recognition phase. In our system we've suggested a number of samples are (5) for each person. The word used to recognized is “alsalamelekum”. The training and recognition of voice signal has using Microsoft Visual Studio Visual Basic 6, besides that, using the SDK (Software Development Kit) of ASR (Automatic Speech Recognition) from Microsoft and we’ve developed the database of this SDK by applying Arabic isolated words. This work, is give an authority for persons whom has a registration then give an access after recognition get done.

For register step in voice recognition, the person needs to record his/her voice for 5 times, and save same name, and in case of login, the user need to record his/her voice to find the out the data in database for matched one, as shown in Figure (9).

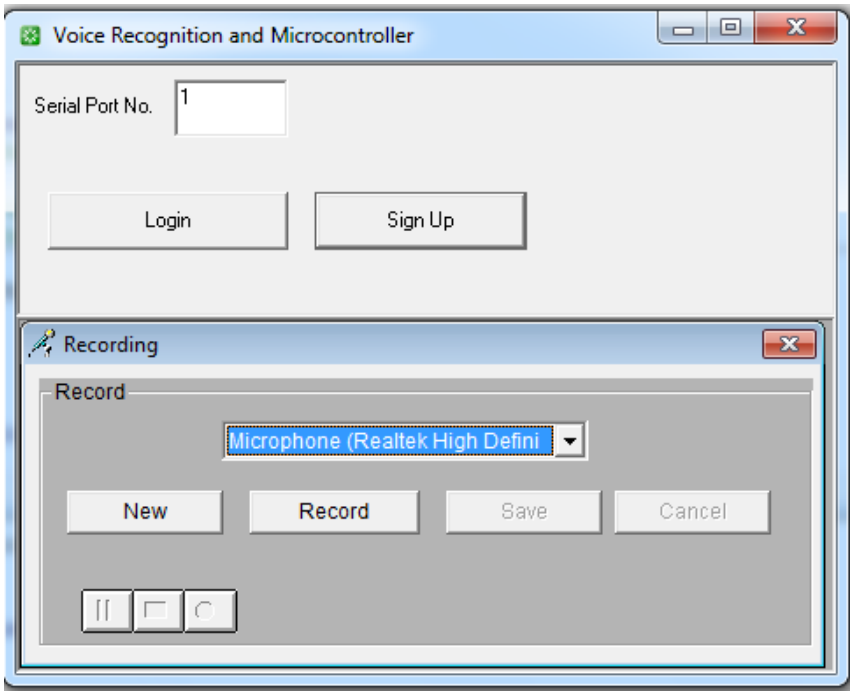

Figure (9)Login/Register form

After the matched of pitched of voice with one found in database, the message will send via serial port to circuit contain a microcontroller (AT89S52) which has been programmed to display the data that received from serial port of PC, as shown in Figure (10).

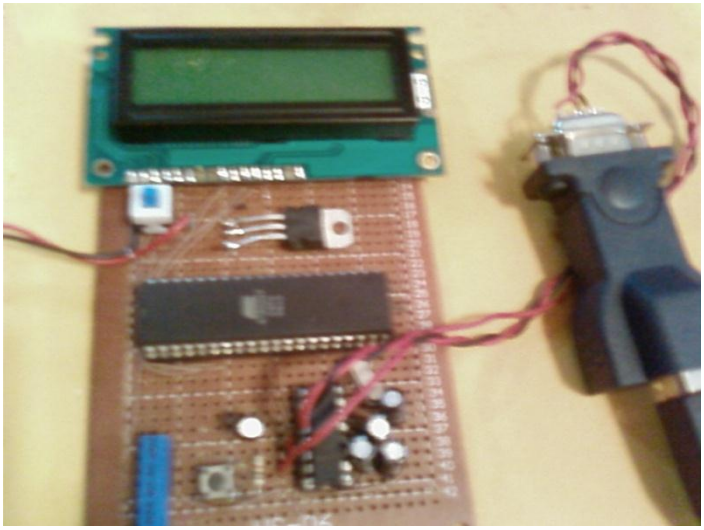

Figure (10) Proposed Circuit

Once the software starting, and the circuit powered up, LCD will show a statement “Voice Recognition” and kept show for a while, and this mean the circuit working well, and the connection to PC also working in right way as shown in Figure (11).

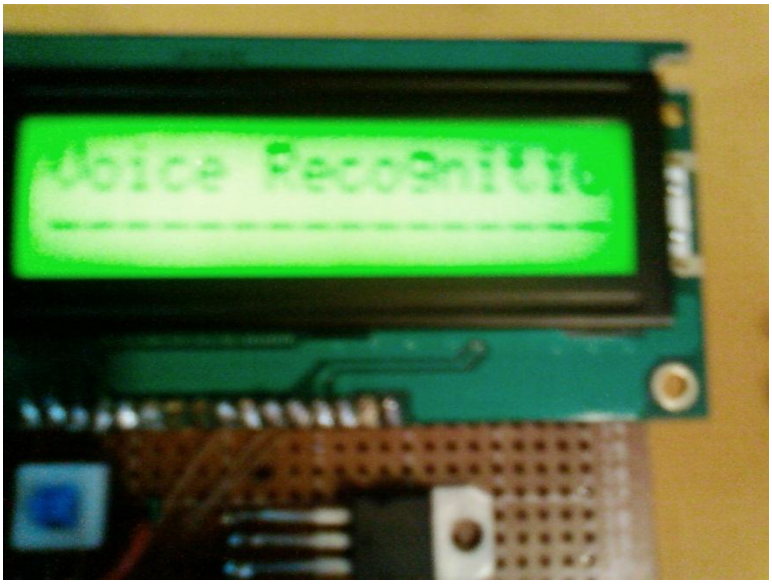

Figure (11) starting statement

When user/person starts recording his/her voice in application, if not recognized found, and matched not done, then the application will tell microcontroller that the person/user not recognized which in same time mean the person/user not authorized (not found his/her data of his/her voice in database), then microcontroller will show a message on LCD for this case as in Figure (12), and the person whom has been signed by his voice will be allowed to access which is method is the main goal of this research.

Figure (12) “not recognized” message on LCD

Otherwise, the recognized of user’s voice matched with once found in database, in this point, the stream of voice will capture by taking the pitches of voice, and then

looking for best accuracy found in database, after this data found, the application will send a stream a name of person to microcontroller via serial port, and microcontroller will send the information to LCD, as shown in Figures (13,14 and 15). And these figures showing the names, which also proposed in our work, beside that, the person whom just signed in by the voice recognition software, has a authentication to be right to access the private or secured places and sectors.

Figure (13) “safaa” name show on LCD

Figure (14) “NOOR” name show on LCD

Figure (15) “mohammed” name show on LCD

The samples was captured are 5-6 samples per person, and give good accuracy for each one be using feature factor with one has been trained. Elapsed time measurement is suspended for typically 300 ms during serial via baud rate 9600b/s and data bit is 8.

8.Conclusion

This proposed work discussed the development of the voice recognition authentication system which can be used to display an authorized person information (name) on microcontroller circuit which is here the LCD, including the system could be used to unlock the door access or any locked system and allowed the authenticator to used his/her voice as an authentication system as an advanced security especially in biometric system.

In addition to display the name of authenticator and controlling the devices connected to output port of microcontroller, the design can be developed to send the information of persons (registered) to other security or location and department via different medium transfer (Bluetooth, Ethernet, web, and network), This work could be benefits for many security department which needs an authentication devices depend on biometric systems and one of them is a voice recognition. This system consists of voice recognition software and a microcontroller circuit that used AT89s52 with LCD 16*2, and the memory of the microcontroller is 8k byte.

Besides the achieving of the main objective, by using this system, it can help reduce any occurrence of getting access to whom not authorized to sensitive places and it offer a more safety way to access. Moreover this system could be fully equipped in a government offices especially in offices not anyone just an authorized need to get in.

9. References

1. Kenneth Revett; "Behavioral Biometrics, A Remote Access Approach"; John Wiley & Sons Ltd, 2008.
2. Sushil Jajodia; "Biometric User Authemtication for IT Security"; 2006.
3. Charles A. Shoniregun, Stephen Crosier;"Securing Biometrics Applications"; Springer Science+Busines Media,LLC. 2008.
4. Lawrence Rabiner, Biing-Hwang Juang; "Fundamentals of Speech Recognition"; 1993.
5. Slavy G. Mihov, Ratcho M. Ivanov, Angel N. Popov; "Denoising Speech Signals by Wavelet Transform"; ANNUAL JOURNAL OF ELECTRONICS, 2009.

6. Kuo, S.M.; Gan, W.S.; Asthana, P.; "Integrated noise reduction and acoustic echo cancellation in hands-free systems"; Intelligent Signal Processing and Communication Systems, 2005. ISPACS 2005. Proceedings of 2005 International Symposium..; 2005
7. Chris Braithwaite, Fred Cowan, Hassan parchizadeh; "8051 Microcontroller, An Application Based Introduction"; Elsevier Publication, 2004.
8. Tobias Scheidat, Marcus Leich, Mark Alexander, and Claus Vielhauer; "Support Vector Machines for Dynamic Biometric Handwriting Classification"; University of Magdeburg, Department of Computer Science, Advanced Multimedia and Security Lab, Universit¨ atsplatz 2, D-39106 Magdeburg, Germany, 2009.
9. Hamid Jahankhani, David Lilburn Watson, Gianluigi Me; "Handbook of Electronic Security and Digital Forensics"; World Scientific; 2010.

Active Vibration Control of Linear and Nonlinear Quarter Car Suspension System Using PID and Fuzzy Logic Controllers

Duna Tariq Yaseen[1] Dr. Qussi Thalib Abdul-Wahab[2]

1. Engineer, Machines and Tools Department, Basrah Technical Institute.

2. Lecturer, Department of Mechanical Engineering, College of Engineering, University of Basrah.

Abstract

A quarter car suspension linear and nonlinear models are considered for the investigation of active vibration control using PID (Proportional-Integral-Derivative) and Fuzzy logic controllers. Simulation of the models using matlab-simulink have been built in this work for passive and active vibration control. The Fuzzy rules and memberships were taken from the literature based on practical experience. A comparison between the linear and nonlinear models using different type of control methods have been carried out. Results shows that the Fuzzy-PID control method is the best among other methods, and the nonlinear model gives better results than the linear model for active control.

Key words: Active, Vibration, Control, Car Suspension, Linear, Non-Linear, PID, Fuzzy Logic

السيطرة الفعالة على الاهتزاز لربع منظومة تعليق سيارة خطية وغير خطية باستخدام مسيطرات (بي آي دي) والمنطق الضبابي

الملخص

نماذج خطية وغير خطية لربع منظومة تعليق سيارة تم اعتبارها لغرض التحري عن سيطرة الاهتزاز الفعالة باستخدام مسيطرات (PID)(بي آي دي) والمنطق الضبابي. محاكاة للنماذج باستخدام برنامج الماتلاب بنيت في هذا العمل لغرض السيطرة على للاهتزاز الاعتيادية والفعالة. القواعد الضبابية والعلاقات تم اخذها من البحوث اعتمادا على الخبرة العملية. مقارنة بين النماذج الخطية والاخطية باستخدام طرق سيطرة مختلفة تم اجراءها. النتائج بينت ان طريقة السيطرة

المسماة (Fuzzy-PID)(بي آي دي- الضبابية) هي الافضل من بين الطرق الاخرى، وان النموذج الغير خطي اعطى نتائج افضل من النموذج الخطي للسيطرة الفعالة.

كلمات مرشدة : فعالة،اهتزاز ،سيطرة،منظومة تعليق سيارة ،خطية، غير خطية، تناظري ،تكاملي،تفاضلي،المنطق الضبابي

1-Introduction

Modeling and control of car suspension system are an essential part of automotive engineering. Passive suspension systems are widely used in passenger vehicles but cannot effectively suppress vehicle vibrations under different road conditions. Active controlled suspension systems are more reliable and efficient than other methods. The success of vibration control for improving the ride comfort is determined by two stages. In particular, the accurate modeling and designing of an appropriate controller have great importance in reduction of vehicle vibrations [1]. Car suspension systems are often modeled as linear characteristic for mathematical simplicity. Nevertheless, real suspension system behavior is nonlinear. In order to account for the nonlinear behavior of car suspension systems, several studies have been found in the literature. Duyn [2] developed a nonlinear damper model , and Yung et al. [3] validated this model for frequencies up to 500 Hz. Dry friction forces that arise from damper have been also studied in the literature. Stein et al. [4] focused on the dry friction modeling and simulation of single degree of freedom.

vibration systems. Also Guclu [5] investigate the the dynamic behavior of a car model which includes the nonlinearities that arise from the dry friction on the dampers. Yagiz et al. [6] presented a nonlinear model of half car system which includes a nonlinear spring and a piecewise linear damper with dry friction. Saban and Ozgur [7] presented a two degree of freedom nonlinear quarter car model. The nonlinearities that were studied in the paper were cubic stiffness, nonlinear damping, and coulomb friction damping in the suspension.

Controlling active suspension systems have considerable effect on the ride comfortability. Control techniques such as PID, Fuzzy, and Fuzzy-PID are employed to increase the overall performance of suspension systems by adjusting the actuator force. Several studies published in the literature related with the control of nonlinear car suspension models such as References [1,5,6,7]. Salem and Aly [8] illustrated the application of fuzzy logic technique to the control of quarter car suspension model. The paper also shows a comparison of active suspension fuzzy control and

PID control using Matlab. Yaujung et al. [9] focuses on the analysis and control of a semi-active suspension system for light vehicles. Models of a quarter-car suspension with air spring and magneto rheological damper were built. Because components in the system involve nonlinear dynamic characteristics, a self-tuning Fuzzy logic controller was designed to the semi-active suspension system. The simulation results showed that the designed suspension system and its controller had good performance for vibration suppression. Pekgokgoz et al. [10], used the fuzzy logic and proportional, integral, derivative (PID) controller methods, the vehicle body deflections and the control force have been obtained and compared with each other. The comparisons displayed the efficiency and convenience of the fuzzy logic controller (FLC) method. Goegoes et al. [11] presented state feedback controller of a quarter-car active suspension system. The controller structure of the active suspension system was decomposed into two loops namely outer loop and inner loop controllers. Outer loop controller is used to calculate the optimum target force to eliminate the effect of road disturbances, while, the inner loop controller is used to keep the actual force close to this desired force. The performance of outer loop controller also shows significant improvement in terms of body acceleration, displacement and suspension displacement as compared to the passive suspension system. Nemat et al. [12], illustrated the application of fuzzy logic technique to the control of continuously damping car suspension system. The paper also described the model and controller used in the study and discussed the response obtained from a range of different input simulations. Choudhury et al. [13] studied the performance of two basic suspension systems with a different approach, passive and active suspension system. Quarter car model was used for simulation of the system. To analyze the model Matlab/Simulink was used and the results show that active suspension system has better ability to reduce the disturbance and also provides better damping quality than passive suspension system. Sawant et al. [14] presented a comparison between simulation results obtained for passive and semi-active linear systems with nonlinear mass, spring, and damper controller. The excitation was taken as actual random road excitation to achieve improved performance. Ebrahimi et al. [15] presented an optimal fuzzy controller developed to improve the performance of active suspension system. Fuzzy logic was used to tune each parameter of the PID controller. They also show that the performance of active suspension system has improved significantly compare to conventional PID

controller. Abdolvahab et al. [16] obtained a mathematical model for the passive and active suspension systems for quarter car model subjected to excitation from road profile. The active suspension system was synthesized by a Linear Quadratic Regulator (LQR) control technique for a quarter car model. The performance of the controller was determined by computer simulation using Matlab/Simulink toolbox.

In this study, simulations and comparisons of different control methods for linear and nonlinear quarter car suspension systems will be carried out using Matlab/Simulink, since there was no such a study or investigation were found in the literature.

2- Mathematical Model of Quarter Nonlinear Car Suspension System

Car suspension systems are often modeled as ideal linear systems despite that real suspension systems have nonlinear characteristics. The first step on setting up a mathematical model for vibration control of a car suspension is to define the nonlinearities in the system. The analysis of nonlinearities in car suspension system is well documented in the literature. A two degree of freedom nonlinear quarter car suspension model, given in reference [7], which is shown in Fig. 1 is considered for this study.

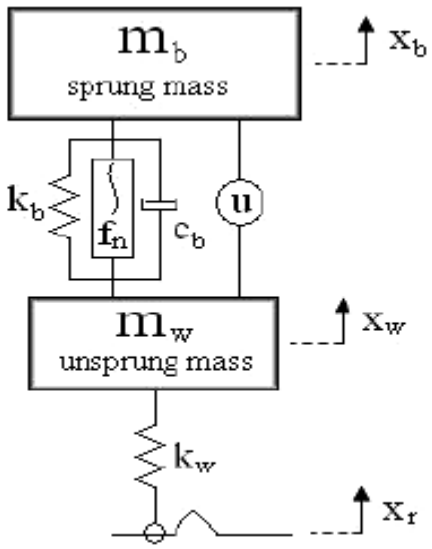

Fig. 1 Nonlinear quarter-car model

The model consists of a quarter car body and a wheel which are connected with a suspension system. The suspension system is consisted of spring, damper, and nonlinear elements. The nonlinearities considered in this model are cubic stiffness, nonlinear damping, and couloumb friction damping in the suspension. An actuator is also connected between the car body and the wheel, and the wheel spring is in contact with the road profile. The dynamical differential equations of this model can be written as follows:

$$m_b * \ddot{x}_b + c_b(\dot{x}_b - \dot{x}_w) + k_b(x_b - x_w) + c_b^n(\dot{x}_b - \dot{x}_w).sgn(\dot{x}_b - \dot{x}_w)$$
$$+k_b^n(x_b - x_w) + \mu.f_{susp}.Sgn(\dot{x}_b - \dot{x}_w) = u \quad (1)$$

$$m_w.\ddot{x}_w - c_b(\dot{x}_b - \dot{x}_w) - k_b(x_b - x_w) - c_b^n(\dot{x}_b - \dot{x}_w)$$
$$-k_b^n(x_b - x_w) + k_w(x_w - x_r) - \mu.f_{susp}.Sgn(\dot{x}_b - \dot{x}_w) = -u$$

where m_b represent 1/4 car body mass, and m_w is the wheel mass. k_b and k_w are the linear stiffness of the suspension car body and the car tire respectively. c_b is the linear damping constant, k_b^n and c_b^n are the nonlinear elements of the suspension system. μ is the friction coefficient and the suspension normal force for Coulomb damping is $f_{susp} = 0.1m_b.g$ [17]. x_b, x_w, and x_r are the vertical displacements of the car body, wheel displacement, and road profile displacement respectively, and u is the actuator control force.

3- Control Methods of Quarter Car Suspension Systems

The aim of control of car suspension systems is to minimize the vibration level of vehicle body as much as possible. Classical PID controllers are widely used and appropriate for car suspension control. Nevertheless, because of its linear characteristics, classical PID controllers are not preferred to control nonlinear systems[1]. In order to cope with nonlinearities a fuzzy logic controllers (FLC) is used in this study to reduce the vibration level of the car body. In addition, the hybrid-type control combining fuzzy logic and PID is also investigated.

3.1 Classical PID Controller

The Conventional PID controllers which combine Proportional, Integral, and Derivative actions linearly are most common controllers applied in industry. The typical PID control law is given by

$$U(t) = K_P.e(t) + K_I.o\int_0^t e(\tau)d\tau + K_D.e^o(t)$$

where $e(t)$ is the error defined as $e(t) = x_{ref} - x_b$.$U(t)$ is a control variable, K_P is a proportional gain, K_I is an integral gain, and K_D is a derivative gain.

3.2 Fuzzy Logic Controller

Fuzzy logic has been widely used for active control problems. Its theory based on linguistic synthesis and does not need an exact mathematical model while designing the control system. Thus, the controller performance is independent from the accuracy of the mathematical model. The classical fuzzy logic controller based on an expert's knowledge or experience has two inputs and one output. The error (e) and change of the error (de) are used for producing a control output (u). In this work the error is taken as the relative displacement (x_b-x_w) and the change of error is the relative velocity (x_b^o-x_w^o). Using the matlab fuzzy logic toolbox shown below:

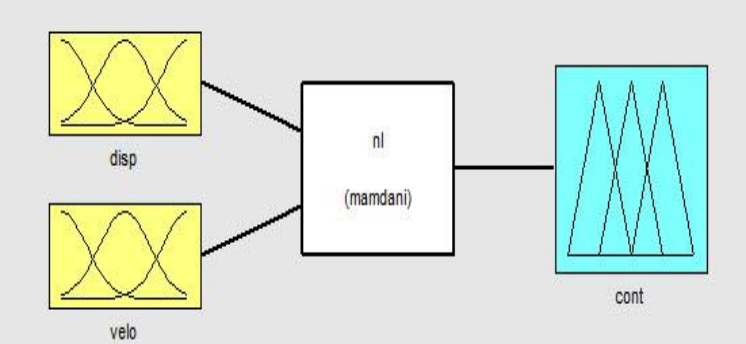

The abbreviation correspond to linguistic variables have been classified as: **NB** (Negative Big), **NM** (Negative Medium), **NS** (Negative Small), **ZE** (Zero), **PS** (Positive Small), **PM** (Positive Medium), and **PB** (Positive Big). Trapeze and triangular membership functions are utilized. All the member ship functions of input and output functions are depicted below:

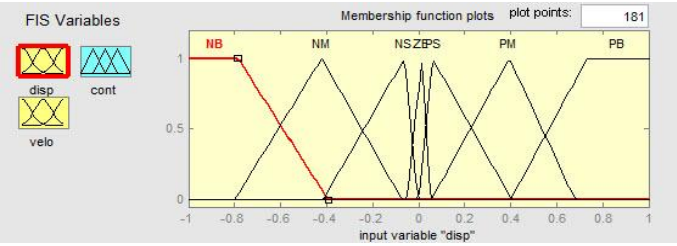

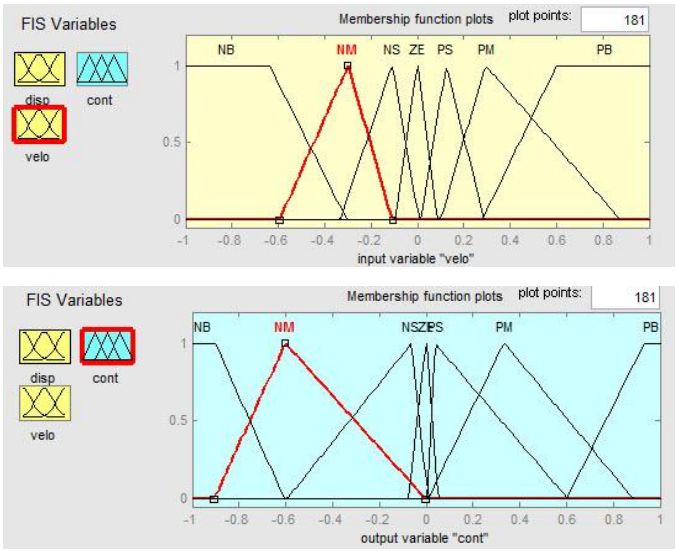

.

A rules based on fundamental knowledge and experience of the system and cover the input-output relations that define the fuzzy control strategy are given in reference [7] in table form as follows:

TABLE I
EXAMPLE OF DECISION TABLE

de/e	NB	NM	NS	Z	PS	PM	PB
NB	NB	NB	NB	NM	NM	NS	ZE
NM	NB	NB	NM	NS	NS	ZE	PS
NS	NB	NM	NS	NS	ZE	PS	PM
Z	NM	NS	NS	ZE	PS	PS	PM
PS	NM	NS	ZE	PS	PS	PM	PB
PM	NS	ZE	PS	PS	PM	PB	PB
PB	ZE	PS	PM	PM	PB	PB	PB

3.3 Fuzzy Logic PID Controller

A combination of the fuzzy logic controller and the PID controller is presented in this work. The structure of the **FLPID** (Fuzzy Logic PID) controller consists of two parts, the classical fuzzy logic controller and PID. The block diagram of the above controller are given in [7] as shown below:

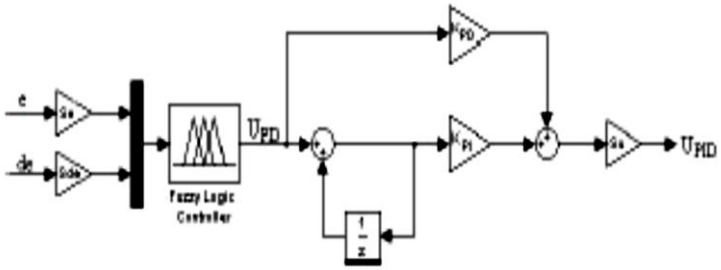

Fig. 2 Block diagram of the two input Fuzzy PID structure

4- Simulation and Results

In this study, simulation are conducted by using the Simulink package in Matlab environment for investigating the performance of the passive and active control of linear and nonlinear quarter car model. The simulink block diagram of a two degrees of freedom nonlinear quarter car model simulated for the purpose of the current investigation is shown in Fig.(3). While the simulink block diagram of the linear model is given in Fig.(4). In order to verify the effectiveness of the simulations, the numerical values of the system parameters are listed in Table II [7].

TABLE II
PARAMETERS OF THE MODEL

Body mass - m_b	295 kg	Damping of suspension - c_b	1000 N.s/m
Wheel mass - m_w	45 kg	Nonlinear stiffness constant - k_b^a	16×10^5 N/m^3
Stiffness of the body - k_b	16 000 N/m	Nonlinear damping constant - c_b^a	600 $N.(s/m)^3$
Stiffness of the tire - k_w	160 000 N/m	Friction coefficient - μ	1

The block diagram of the linear and nonlinear passive control model is shown in Fig.(5). The simulation results of passive control of the linear and nonlinear models are shown in Fig.(6). The figure presented the behavior of each model separately. Although the behavior of the nonlinear model showed more oscillations than the linear model, this is expected because the effect of the coulomb friction, but comparing the maximum amplitudes of the two models, it is clear that the nonlinear model gives 10 times less amplitude than the linear model. The block diagrams of the linear and nonlinear active PID control model is shown in Fig.(7). The simulation results of this model are shown in Fig.(8). It is clear from this figure that the

amplitude and time of the nonlinear PID model is less than that of the linear PID model, and that mean the nonlinear model is better controlled by PID than the linear model. Fig.(9) shows the block diagram of linear and nonlinear active Fuzzy control model. The simulation results of this model are presented in Fig.(10). It clear from this figure that the nonlinear model response is more controllable using this controller than the linear model. The active Fuzzy logic PID control model block diagram is illustrated in Fig.(11). The response of the models for the above control method are shown in Fig.(12). It clear from this figure that the behavior of the nonlinear model is much better than the behavior of the linear model. Finally model comparisons is carried out in this study to show the responses of the linear and the nonlinear car suspension to the different control methods. Figures (13) and (14) illustrated these responses for linear and nonlinear models respectively. The figures shows that the fuzzy-PID control method is more efficient in controlling the car suspension system.

5-Conclusions

From the above investigation, the following conclusions can be drawn:

1- The nonlinear model is more capable in describing the response of the quarter car suspension system for passive and active control methods.

- The fuzzy-PID control method is more stable for controlling the car suspension system than other investigated methods.

3- Finally the comparison between the linear and nonlinear models is the first to be carried out in this research and no such a comparison was found in the literature.

6- References

[1] Ozgur Demir, Ilknur Keskin, Saban Cetin,"Modeling and control of a nonlinear half-vehicle suspension system: a hybrid fuzzy logic approach", Nonlinear Dyn (2012).

[2] Duym,S., Stiens, R., Reybrouck, K., "Evaluation of shock absorber models", Veh. Syst. Dyn. 27(2) (1997).

[3] Yung, V.Y., Cole, D.J., "Modeling high frequency force behavior of hydraulic automotive dampers", Veh. Syst. Dyn. 44(1), (2006)

[4] Stein, G.J., Zahoransky, R., Mucka, P., "On dry friction modeling and simulation in kinematically exited oscillatory systems", J. Sound Vib. 311(1), (2008).

[5] Guclu, R., " Fuzzy logic control of seat vibration of a nonlinear full vehicle model", Nonlinear Dyn. 40, (2005).

[6] Yagiz, N., Hacioglu, Y., Taskin, Y., "Fuzzy sliding-mode control of active suspension", IEEE Trans. Ind. Electron. 55(11), (2008).

[7] Saban Cetin, Ozgur Demir, " Fuzzy PID Controller with coupled Rules for a Nonlinear Quarter Car Model", PWASET Vol. 13, (2008).

[8] Salem M., Aly A., "Fuzzy Control of a Quarter-Car Suspension System", WASET (53), (2009).

[9] Yaojung, S., Chun-Chi L., Quang-Anh N.,"The Analysis of a Semi-Active Suspension System", SICE Annual Conference (2010).

[10] Pekgokgoz R.K., Gurel M.A., Bilgehan M.K., "Active Suspension of Cars Using Fuzzy Logic Controller Optimized by Genetic Algorithm", IJEAS Vol. 12 Issue 4 (2010).

[11] Goegoes D., Gigih P., " PID State Feedback Controller of a Quarter Car Active Suspension System", J. Basic Appl. Sci. Res. 1(11), 2011.

[12] Nemat C., Modjtaba R., "Comparing PID and Fuzzy Logic Control a Quarter Car Suspension System", TJMCS Vol .2 No.3 (2011).

[13] Choudhury S. F., Sarkar M. A.," An Approach on Performance Comparison Between Automotive Passive Suspension and Active Suspension System (PID Controller) Using Matlab/Simulink", JATIT, Vol.43 No.2 (2012).

[14] Sawant S., Tamboli J., "Analysis and Comparsion of Vehicle Dynamic System with Nonlinear Parameters Subjected to Actual Random Excitation", IJMET, Vol. 3 Issue 2 (2012).

[15] Ebrahimi N., Gharaveisi A., "Optimal Supervisor Controller for An Active Suspension System", IJSCE, Vol. 2 Issue 4 (2012).

[16] Abdolvahab A., Chavan U., Phvithran S., "Simulation and Analysis of Passive And Active Suspensin Quarter Car Model For Non Uniform Road Profile", IJERA, Vol. 2, Issue 5, (2012).

[17] McGee C.G., Haroon M., Adams D.E., Luk Y.W., "A frequency Domain Technique for Characterizing Nonlinearities in a Tire-Vehicle Suspension System", Journal of Vibration and Acoustics, Vol. 127, (2005).

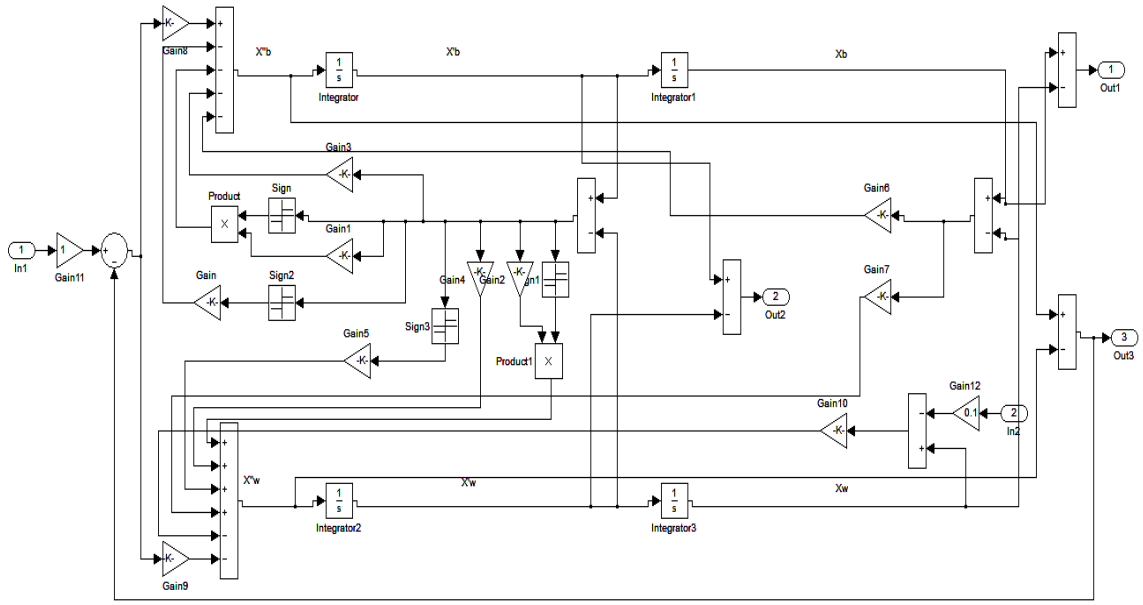

Fig.(3) Simulink block diagram of nonlinear quarter car passive model.

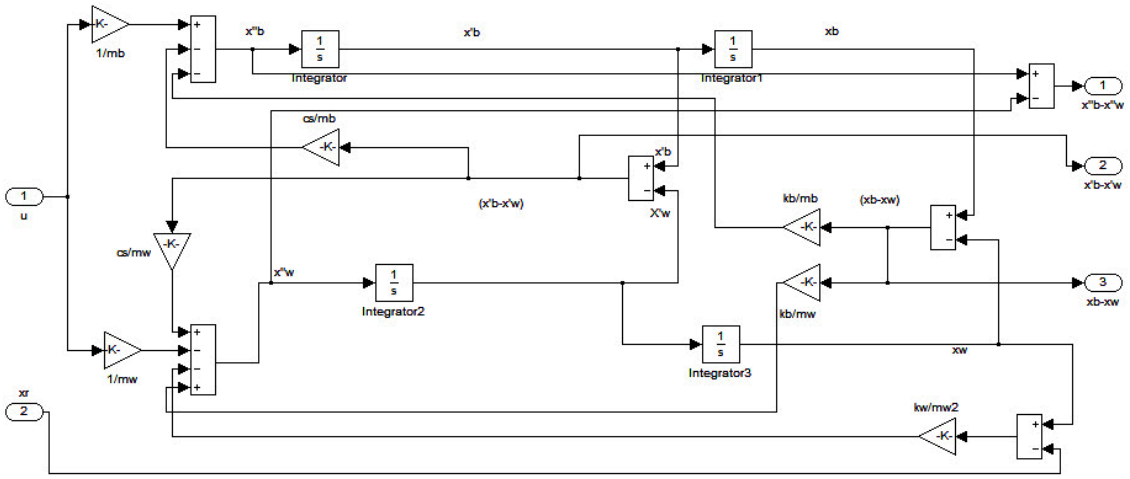

Fig.(4) Simulink block diagram of linear quarter car passive model.

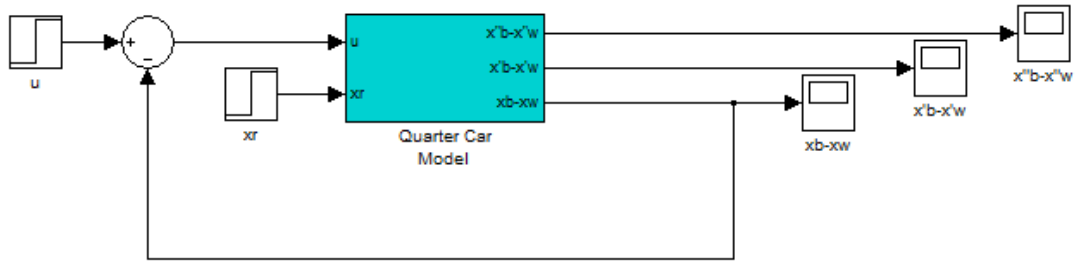

Fig.(5) Simulink Block Diagram of linear and nonlinear quarter car Passive models.

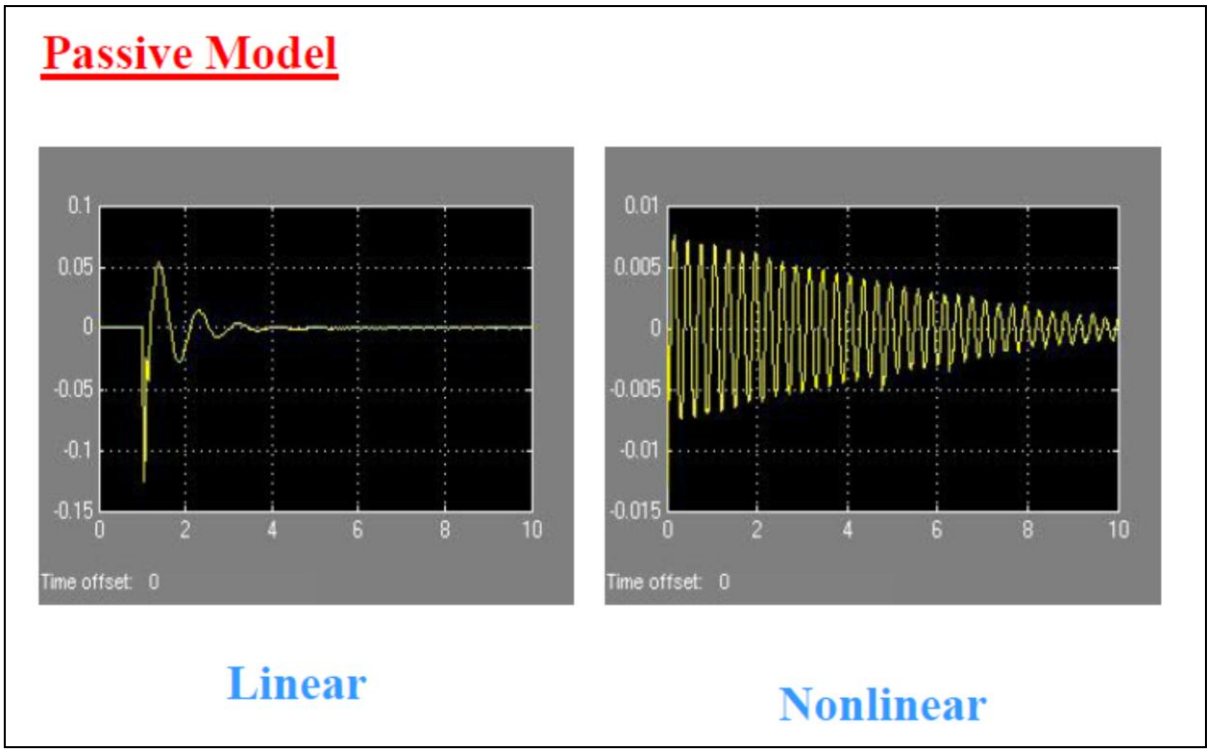

Fig.(6) Model Response of linear and nonlinear quarter car passive models.

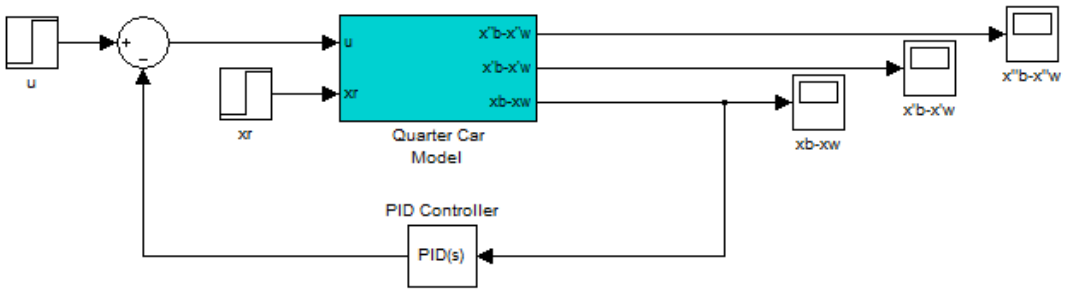

Fig.(7) Simulink Block Diagram of linear and nonlinear quarter car active PID models.

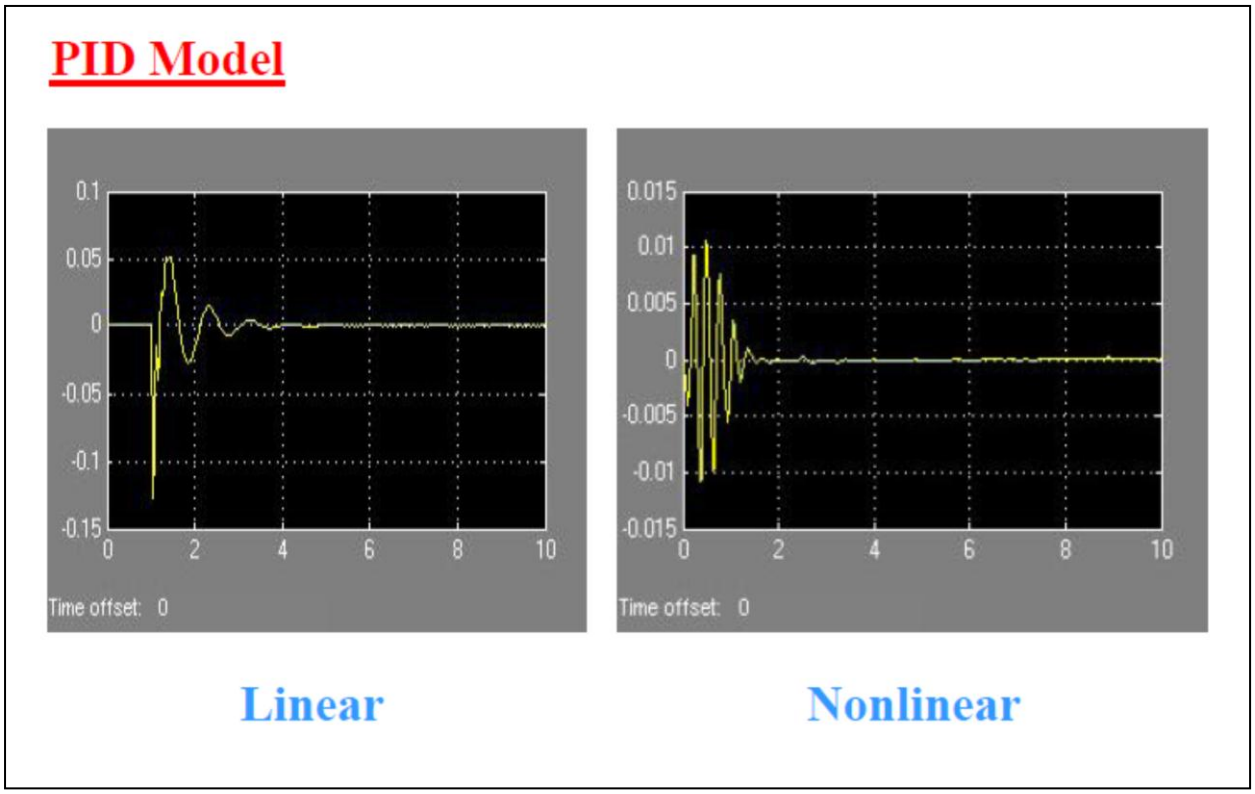

Fig.(8) Model Response of linear and nonlinear quarter car active PID models.

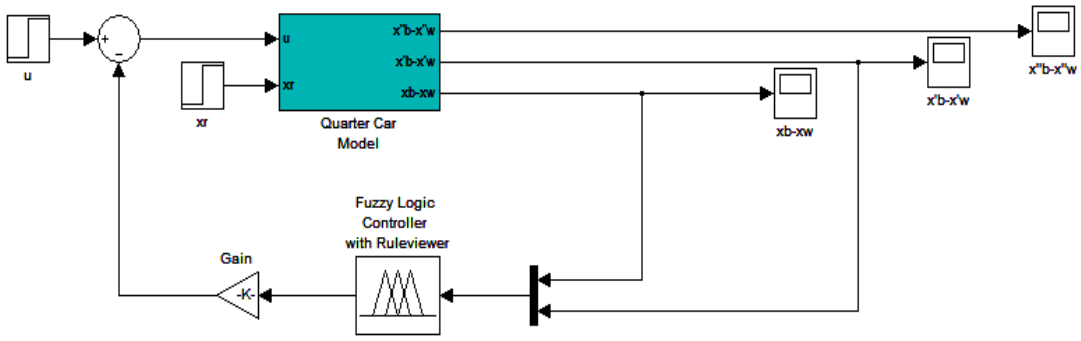

Fig.(9) Simulink Block Diagram of linear and nonlinear quarter car active Fuzzy models.

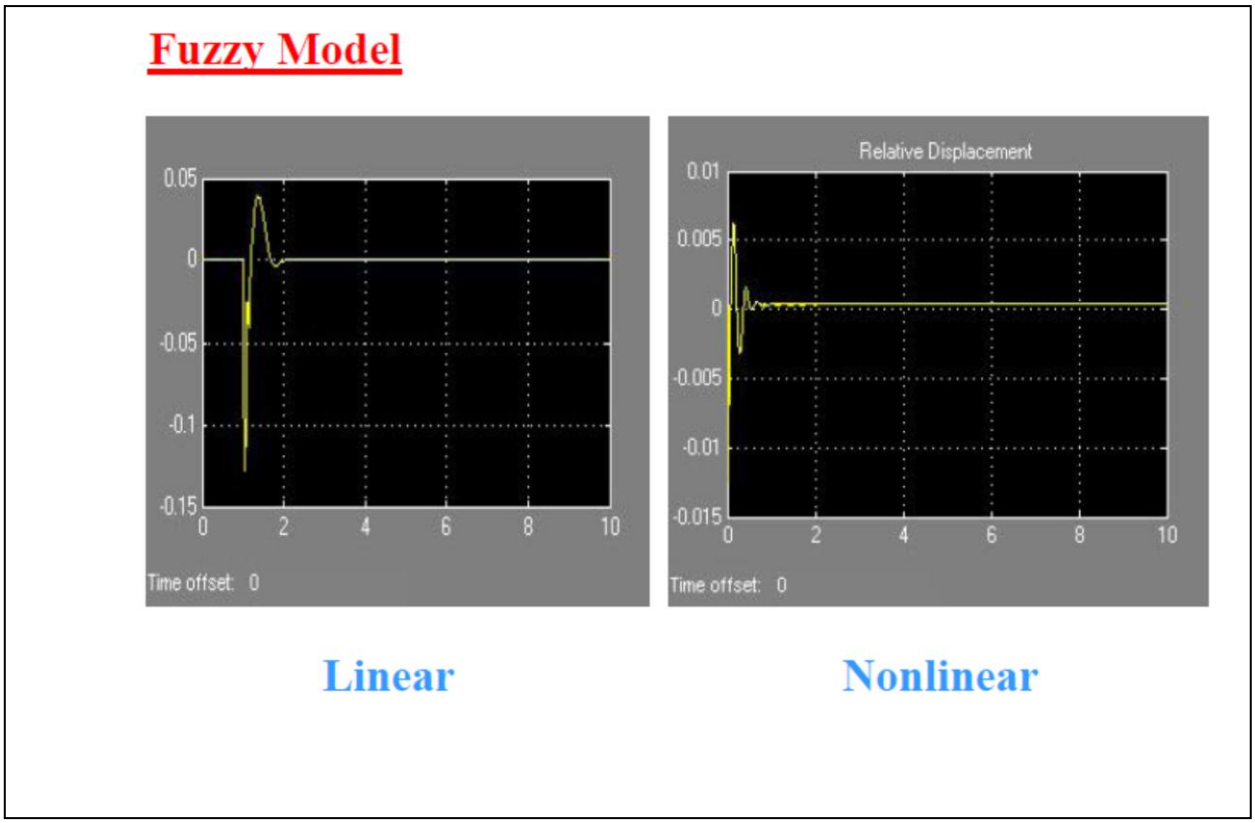

Fig.(10) Model Response of linear and nonlinear quarter car active Fuzzy models.

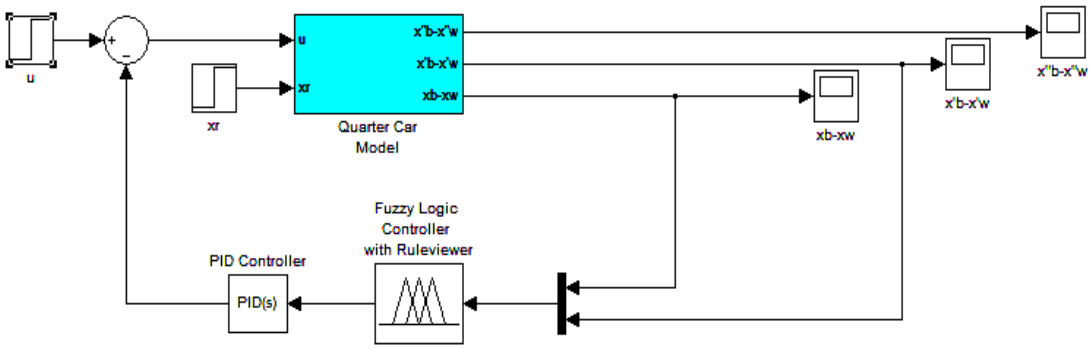

Fig.(11) Simulink Block Diagram of linear and nonlinear quarter car active Fuzzy PID models.

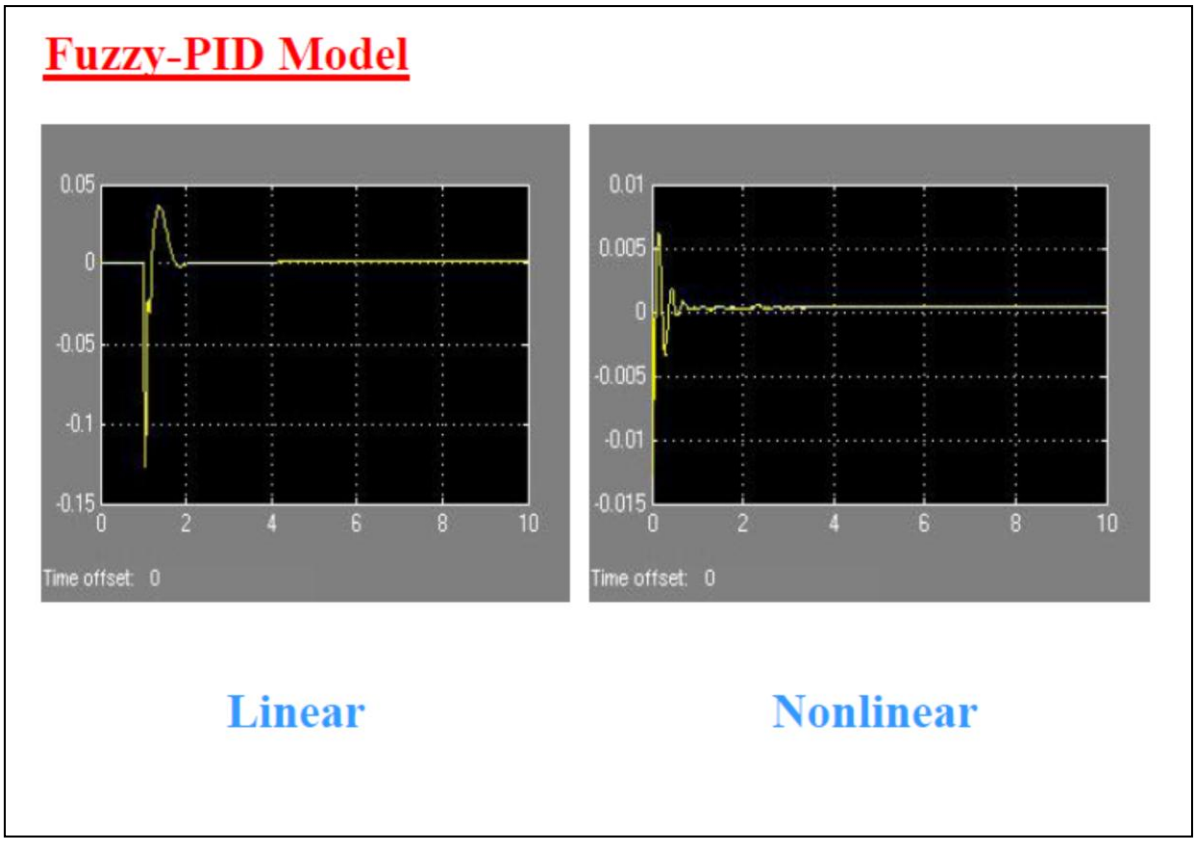

Fig.(12) Model Response of linear and nonlinear quarter car active Fuzzy PID models.

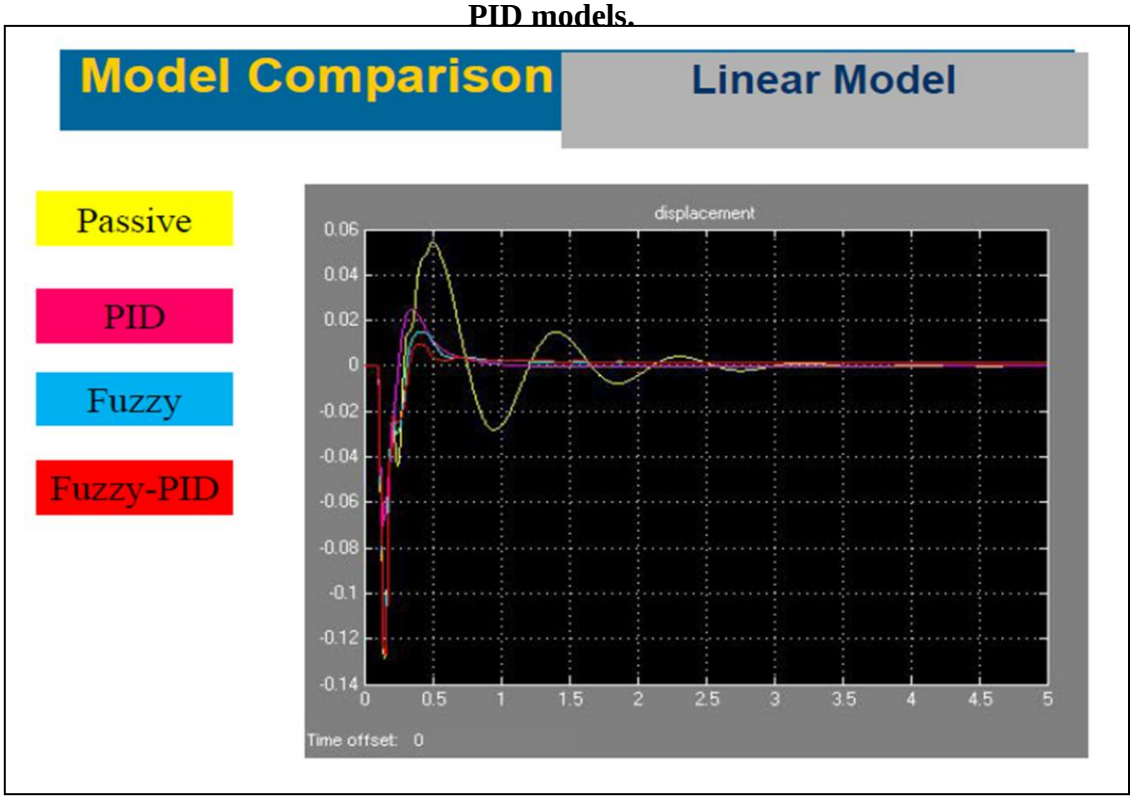

Fig.(13) Model comparison of linear quarter car model with different control methods.

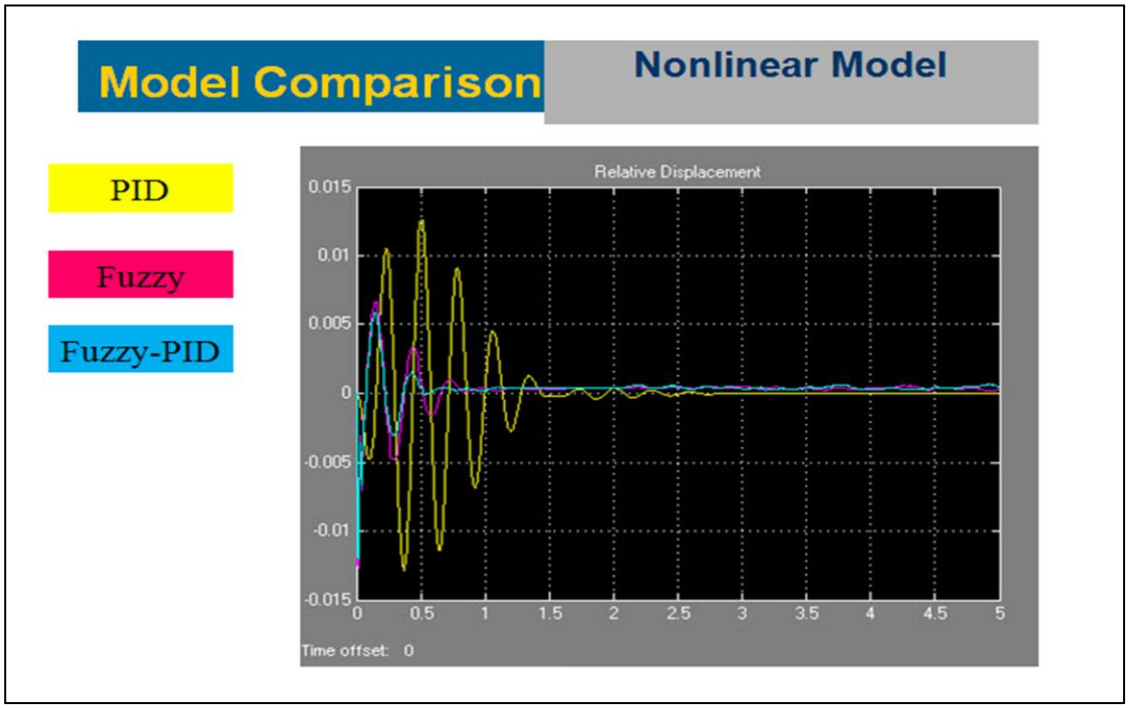

Fig.(14) Model comparison of nonlinear quarter car model with different control methods.

Effect of glass fibers on mechanical properties of structural lightweight foamed concrete(SLFC)

Dr.Eethar Thanon Dawood
Head of Building & Construction
Eng.-Technical College of Mosul

Ali Jehad Hamad
MSc. Candidate Building & Construction
Eng.-Technical College of Mosul

Abstract

Lightweight foamed concrete exhibits many advantages and excellent features comprising more efficient strength-to-weight ratio in structural elements, high strength, reduced dead load, decrease foundation loads, energy saving, waste consuming, temperature conservation, and noise insulation. This work was prepared to investigate the effect of glass fibers on mechanical properties of structural lightweight foamed concrete (SLFC), Foam agent (organic material) was used to produce SLFC using different mix proportions to obtain structural compressive strength and high workability with slightest fresh density. Five mixes of SLFC with Superplasticizer is experimentally studied, also five mixes without Superplasticizer were tested. The compressive strength, flexural strength, ultrasonic pulse velocity (UPV), workability (flowability) and density were measured. Superplasticizer used in some mixes was 1% by weight of cement. Glass fibers were added in different volume fraction for SLFC and SLFC with superplasticizer. The volume fractions of the glass fibers used are: 0.06, 0.2, 0.4, and 0.6 % total volume. The results of SLFC mixes showed that the increase of glass fibers content can produce foam concrete with enhanced mechanical properties. For all percentages of glass fibers in the mixes it increases in compressive strength and flexural strength. But the increase in compressive strength was 51% for 0.6% glass fibers. Also the flexural strength increased 19.2% for 0.6% glass fibers. The compressive and flexural strength increased with the increase of glass fibers with acceptable range of workability.

Keywords: Structural lightweight foamed concrete (SLFC); Lightweight concrete; foamed concrete; Glass fibers; Mechanical properties.

تأثير اضافة الالياف الزجاجية على الخصائص الميكانيكية للخرسانة الرغوية الخفيفة الوزن الانشائية

الخلاصة:

الخرسانة الرغوية الخفيفة الوزن لها العديد من الايجابيات والخصائص والتي تتضمن: مقاومة عالية مقارنة بوزن العنصر الانشائي و تقلل من الحمل الميت و تقليل الاحمال على الاسس و استخدام المخلفات و هي عازلة

للحرارة والصوت. ان هذا البحث يهدف الى دراسة تأثير الالياف الزجاجية على الخصائص الميكانيكية للخرسانة الرغوية الخفيفة الوزن الانشائية. استعمل العامل الرغوي للحصول على خرسانة رغوية الخفيفة الوزن الانشائية، حيث تم عمل عدة نسب خلط للوصول او الحصول على مقاومة انضغاط انشائية مع قابلية تشغيل عالية وبأقل كثافة. خمس نسب خلط للخرسانة الرغوية الخفيفة الوزن الانشائية مع الملدن المتفوق وخمس نسب خلط اخرى للخرسانة الرغوية الخفيفة الوزن الانشائية بدون الملدن المتفوق ، كل هذه الخلطات اجريت عليها فحص مقاومة الانضغاط وفحص مقاومة الانحناء و فحص سرعة الموجات فوق الصوتية وقياس قابلية التشغيل والكثافة. استخدم الملدن الفائق بنسبة 1% من وزن السمنت. كانت نسبة الالياف الزجاجية المضافة للخرسانة الرغوية الخفيفة الوزن الانشائية مع الملدن الفائق و الخرسانة الرغوية الخفيفة الوزن الانشائية بدون الملدن الفائق هي 0.06 و 0.2 و 0.4 و 0.6% من الحجم الكلي للخرسانة. النتائج اوضحت ان اضافة الالياف الزجاجية للخرسانة الرغوية الخفيفة الوزن الانشائية يحسن من مقاومة الانضغاط بنسبة 51% بنسبة الياف زجاجية 0.6% مقارنة مع الخلطة التي بدون الياف زجاجية. كذلك بالنسبة لمقاومة الانحناء تحسنت بنسبة 19.2% عند اضافة 0.6% من الالياف الزجاجية. وكذلك بالنسبة لباقي نسب الخلط حيث ان مقاومة الانضغاط والانحناء لكل النسب ازدادت بزيادة نسبة الالياف الزجاجية اي ان اضافة الالياف الزجاجية الى الخرسانة الرغوية الخفيفة الوزن الانشائية سوف يحسن من مقاومة الانضغاط ومقاومة الانحناء مع الحفاظ على قابلية التشغيل.

الكلمات الدالة: الخرسانة الرغوية الخفيفة الوزن الانشائية ، الخرسانة الخفيفة الوزن ، الخرسانة الرغوية ، الالياف الزجاجية ، الخصائص الميكانيكية.

1. Introduction

Lightweight concrete is widely used for modern construction as it is mortar less and can be produced with different densities. Lightweight concrete also known as aerated, cellular lightweight concrete, or foam concrete (Kamarulzaman, 2010) [1]. Lightweight concretes have an oven-dry density varies from 300 kg/m^3 to 2000 kg/m^3, with compressive strength for cube may reach to more than 60 MPa (Owens et al., 2003)[2]. Recently, with the rapid development in the construction, the lightweight concrete has been used for structural purpose and many applications for modern construction. The advantages of lightweight concrete are high strength/weight ratio, good tensile strain capacity, low coefficient of thermal expansion due to the voids, thermal insulation, increased fire resistance over ordinary concrete, improved durability properties, smaller cross-sections in load-bearing elements and reduction in the size of foundations. The applications of lightweight concrete are tall buildings, long span structure, the requirements for high performance are higher strength and higher toughness (Libre et al., 2011)[3]. Structural lightweight concrete have bulk density lower than 1950 kg/m^3 with compressive strength more than 17 MPa, such concrete can be produced with 25% lighter than normal-weight concrete with a

compressive strength up to 60 MPa (Li, Z., 2010)[4]. Aerated concrete is produced by introducing or generating bubbles voids within the concrete (cement matrix), the voids or cell structure having a homogeneous distribution in cement matrix when formed of voids inside the fresh cement mixture, density varies from 300 to 1600 kg/m^3 (Fouad, 2006)[5]. Aerated concrete is known as foamed concrete. Foamed concrete is classified in two types according to the method producing i. pre-foaming method include preformed foamed (foam agent with water) and mixed with cement slurry (cement paste or mortar), ii. mixing foaming method is mixed of foam agent with cement slurry, foam will produce voids inside the concrete (Ramamurthy et al., 2009)[6]. Density of foam concrete depend on proportion of foam agent and water (Ramamurthy et al., 2009)[6]. The compressive strength of foam concrete is just about 1 to 60 Mpa compare to normal concrete which achieved 100Mpa in compressive strength (Zahari, 2009)[7]. Foam concrete can be used for structural application, partition, insulation and filling grades (Ramamurthy et al., 2009)[6].

Concrete is considerable as brittle material, which results in poor fracture toughness, poor resistance to crack propagation, and low impact strength. This inherent brittleness has limited their application in fields requiring high impact, vibration and fracture strengths Therefore, to improve the mechanical properties of concrete, fibers can be used. Fibers are used to modify the tensile and flexural strengths, toughness, impact resistance, fracture energy, arrest crack formation and propagation, and thus improve strength and ductility (Dawood and Ramli, 2011)[8].

Glass Fibers is one type of fiber reinforced concrete, the main applications used in exterior building facade panels and as architectural precast concrete. The fibers glass is less dense than steel thus is very good in making fair face in front of any building (Abdullah and Jallo, 2012)[9]. Glass fibers improve the strength of the material by increasing the force required for deformation and enhance the toughness by increasing the energy required for crack propagation (Chandramouli et al., 2010)[10]. The glass fibers when added to the mix would enhance the mechanical properties, flexural strength, compressive strength, tensile strength and young modulus of the materials (Abdullah and Jallo, 2012)[9]. However, the use of glass fibers decreases the workability of fresh concrete and this effect is more prominent for fibers with higher aspect ratios (Chandramouli et al., 2010)[10].

Therefore, this paper was conducted to produce structural lightweight foam concrete with structural compressive strength, high workability (flowability), and acceptable

range of density. Adding glass fibers to structural lightweight foam concrete with different ratio to study the effect of glass fibers on compressive strength, flexural strength, ultrasonic pulse velocity, workability and density.

2. Materials and mix proportions

2.1. Materials

2.1.1. Cement: ordinary Portland cement type I from Badoosh manufacture in Nineveh Governorate of Iraq was used in this study, the physical characteristics according to IQS : 5/1984[11] are shown in Table 1, the chemical compositions of cement according to IQS : 5/1984[11] are shown in Table 2.

2.1.2. Fine aggregates (Sand): sand used in this study was natural sand supplied from Kanhash region (Mosul). The specific gravity of sand 2.63 and fineness modulus is 2.69. The grading limits according to ASTM C33[12] are given in Table 3.

2.1.3. Water: Potable water was used in this study.

2.1.4. Foam agent: was used to obtain structural lightweight foam concrete. The type of foam agent (NEOPOR) (leycoChem LEYDE GmbH Germany) is an organic material, which has no chemical reaction but serves solely as wrapping material for the air to be induced in the concrete. The foaming agent has to be diluted in 40 parts of water before using it according to manufacturer.

2.1.5. Glass fibers: were used in the lightweight foam concrete, the properties of the glass fibers are listed in Table 4 and Figure 1. Different volume fractions of glass fibers are used as given in Table 5.

2.1.6. Superplasticizer: a high Range Water Reducing based on naphthalene sulphonate (RHEOBUILD® 181 K) (BASF the chemical company) was used in this study. The technical data of High Range Water Reducing based on naphthalene sulphonate shown in Table 6.

Table 1.
Physical characteristics of ordinary Portland cement.

Test	result	IQS : 5/1984
Initial setting time (minute)	210	Min. 45 minute
Final setting time (minute)	330	Max. 600 minute
Fineness (Blain m^2/kg)	263	Min. 230 (m^2/kg)

Table 2.
Chemical properties of ordinary Portland cement.

Constituent	Component of OPC (%)	Limits of IQS : 5/1984
SiO_2	21.31	…
Al_2O_3	5.89	…
Fe_2O_3	2.67	…
CaO	62.2	…
MgO	3.62	$\leq 5\%$
SO_3	2.6	$\leq 2.8\%$
Loss of ignition	1.59	$\leq 4\%$
Insoluble residue	0.24	$\leq 0.75\%$
Free CaO	1.74	…
L.S.F.	0.8818	…
C_3S	33.37	…
C_2S	35.92	…
C_3A	11.09	…
C_4AF	8.12	…

Table 3.
Grading of fine aggregates.

Sieve No. (mm)	Passing (%)	Limits of ASTM C 33
No.4 (4.75)	100	95-100
No.8 (2.36)	80.96	80-100
No.16 (1.18)	66.33	50-85
No.30 (0.6)	51.5	25-60
No.60 (0.3)	24.65	5-30
No.100 (0.15)	7.26	0-10

Table 4.
Properties of glass fibers.

Fiber properties	Quantity
Fiber length	1.2 cm.
Aspect ratio	24
Specific gravity	2.68 g/cm^3
Modulus of elasticity	72 GPa
Tensile Strength	1,700 MPa
Chemical Resistance	Very high
Electrical Conductivity	Very low
Softening point	860 °C
Material	Alkali Resistant Glass

Table 5.
The volume fraction of glass fibers and Superplasticizer in lightweight concrete mixes.

Mix no.	N0	N1	N2	N3	N4	N5	N6	N7	N8	N9
Glass fiber ratio* (%)	0.0	0.06	0.2	0.4	0.6	0.0	0.06	0.2	0.4	0.6
Superplasticizer# (%)	0.0	0.0	0.0	0.0	0.0	1	1	1	1	1

* Percentages of glass fibers taken by total volume of concrete.
# Percentages of Superplasticizer taken by weight of cement.

Table 6.
Technical date of High Range Water Reducing based on naphthalene sulphonate.

Technical data	
Structure of the materials	Napthalene Sulphonate Based
Color	Brown
Density	1.153-1.213 kg/liter
Chloride content %(EN 480-10)	< 0.1
Alkaline content %(EN 480-12)	< 10

Figure 1: Micro glass fiber.

2.2 Mix proportions

The mix proportion used in this study was 1:2.25 cement and sand respectively with water cement ratio w/c=0.4 for mixes with superplasticizer and w/c =0.49 for mixes without superplasticizer. The foam agent used was 1 kg/m^3 see Table 7. The procedure of mixing is achieved by blending the cement with sand according to the mix proportion and then the water was added to prepare the mortar. After that, the foam was added to the mortar to obtain lightweight foamed concrete. It should be mentioned that the preparation of the foam is done using the foam agent which is diluted in 40 parts of water according to manufacturer. This is calculated as a part of the total water of the mix shown in Table 7. When the foam added to the mortar, the foam should be blended to make homogeneous mixture. Glass fibers are incorporated in different proportions of volume fraction as shown in Table 5. Finely, Gradually added the glass fibers to the mix (foamed concrete). The mix should have a uniform dispersion of the fibers in order to prevent segregation or balling of the fibers during mixing. Most balling occurs during the fiber addition process. Increase of aspect ratio, volume percentage of fiber, and size and quantity of coarse aggregate will intensify the balling tendencies and decrease the workability (Hassan, 2012)[13].

Superplasticizer used in the mix as 1% from weight of cement as shown in Table 5. Each mix proportion was measured in term of flow according to ASTM C 1437[14] and ASTM C 230[15].

Table 7.

Mix proportions.

Series	Mix No.	Mix proportion	Glass fibers (kg/m³)	w/c	Cement (kg/m³)	Sand (kg/m³)	Water (kg/m³)	Foam agent (kg/m³)	Theoretical density (kg/m³)	Flow (%)
Series I	N0	(1 : 2.25) (cement : sand)	0.0	0.49	481.2	1082.7	235.8	1	1799.6	130
	N1		1.6	0.49	484.8	1090.8	237.5	1	1813.1	125
	N2		5.4	0.49	488.4	1098.9	239.3	1	1826.6	120
	N3		11	0.49	490.2	1103.0	240.2	1	1833.4	113
	N4		16	0.49	493.2	1109.7	241.6	1	1844.5	95
Series II	N5		0.0	0.4	510.6	1148.9	204.2	1	1863.7	118
	N6		1.6	0.4	517.6	1164.7	207.0	1	1889.3	114
	N7		5.4	0.4	521.4	1173.2	208.5	1	1903.1	107
	N8		11	0.4	522.7	1176.1	209.0	1	1907.8	92
	N9		16	0.4	523.3	1177.5	209.3	1	1910.1	84

3. Experimental work

Test specimens of 50×50×50 mm^3 cubes were used for testing the compressive strength of lightweight concrete according to ASTM C 109[16] as shown in Figure 2. The average of three cubes was used to determine the compressive strength for each age (7 and 28 days) of test. The prisms of 40×40×160 mm^3 were used to determine the flexural strength according to ASTM C 348[17] as shown in Figure 3. The average of three prisms was used to determine the flexural strength. In the laboratory the foam produced by using a mixer, which forming the foam according to the pre-foaming method, adding the preformed foam to a base mix (cement, sand, and water). The structural lightweight foamed concrete mixture was divided into two series: series I, used fibers glass only, and series II, used fibers glass and superplasticizer as shown in Table 8. The fresh density was measured by using container of known weight and volume. The specimens were stripped approximately 24 h after casting and placed in water using a water tank as a normal water curing method with a controlled temperature of 23 ºC ± 2 ºC according to ASTM C 192[18]. Each mix was tested in

the compressive strength and flexural strength at ages (7 and 28 days) according to ASTM C109[16] and ASTM 348[17] respectively. The ultrasonic pulse velocity (UPV) test was performed on cube of structural lightweight foamed concrete for all mixes, the ultrasonic tester PUNDIT (Portable Ultrasonic Non-destructive Digital Indicating Tester) used to measure the ultrasonic pulse velocity Figure 4 (a), direct transmission manner was used in this test as shown in Figure 4 (b), The oven dry density and voids were determined using 100 mm cubes according to ASTM C 642[18] for each mix.

Figure 2: **a)** Compressive strength test machine. **b)** Test specimens 50×50×50 mm^3. cubes. **c)** Specimen inside the testing machine.

Figure 3: Flexural strength test machine and specimen inside the testing machin

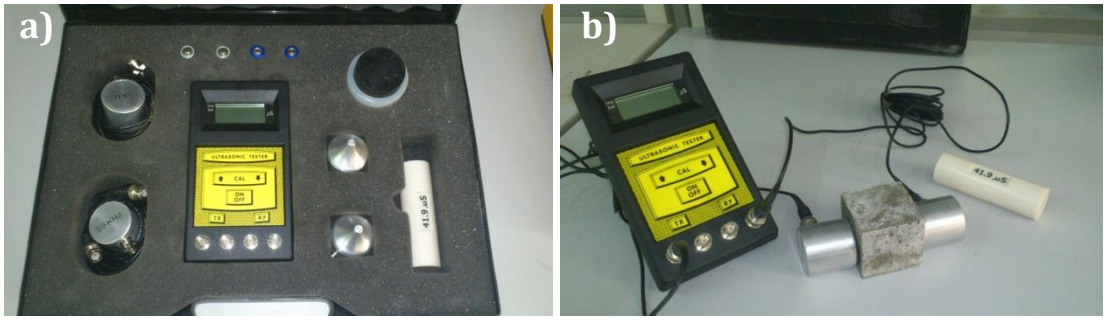

Figure 4: a) Ultrasonic tester (PUNDIT). **b)** Direct transmission manner of ultrasonic pulse velocity test.

4. Results and discussion

4.1. Workability

The workability (flow) was measured according to ASTM C 1437[14], the flow for foamed concrete reinforced with glass fibers varied among mixes depending on volume fraction of glass fiber, the flow of mixes given in Table 7. The flow varied between (130-84%), the flow was about 130% for mix N0 (series I), and flow reduced with the increase of glass fibers. Thus, the use of 0.6% of glass fibers reduced the flow to 95%. Regression analysis was used in all figures to obtain the equation. Regression analysis was used to show the relationship between glass fibers and workability of foamed concrete as shown in Figure 5. This relationship illustrates that the workability (flow) reduces with the increase of fibers (Neville and Brooks, 2010)[20].

The flow for mixes containing superplasticizer decreases due to the reduction in water-cement ratio (w/c=0.4) and also the use of glass fibers as shown in Table 7. The flow was 118% for mix N5, and also with the fiber increase the workability (flow) would decrease. For mix N9, with glass fibers 0.6%, the flow is 84% and thus the percentage of reduction in the flow is about 28.81% compared with reference mix (N5). Figure 5 shows the effect of glass fibers on the flow of mixes containing superplasticizer (series II).

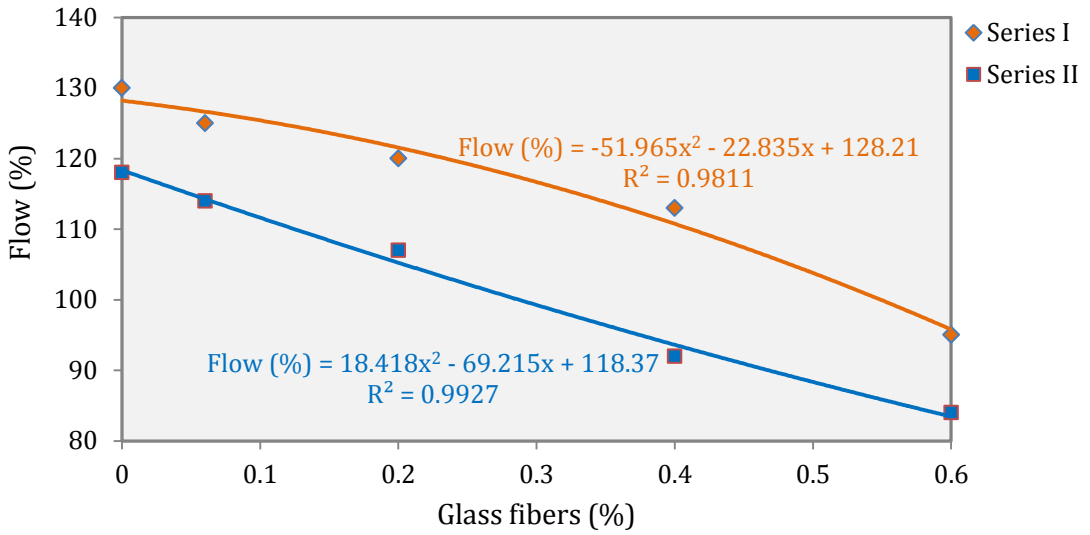

Figure 5: Effect of glass fiber (%) on the flow of the mixes.

4.2. Microstructure

Microstructure of structural lightweight foamed concrete reveal the effect of foam and fibers on the mechanical properties. The microstructure of the mixes is shown in Figure 6, this images taken by stereo microscope. It seems that increase internal voids (pore) microstructure of the structural lightweight foamed concrete would decrease the density. The increase in the number of the larger voids tends to lower the density of such concrete but the density increased when the voids be smaller and more unbroken in size (Mydin and Soleimanzadeh, 2012)[21]. The microstructure for each mixes is varied widely depending on the density, addition of glass fibers, and volume fraction of glass fibers for mixes. Figure 6 (a and b) shows the image for structural foamed concrete without glass fibers , and also exhibit the shape of voids inside of concrete. The amount of foam influences the production of bubbles inside the concrete and creating the voids (Awang et al., 2012)[22]. The addition of glass fibers would increase the density, resulting from the reduction of the pores and voids within the foam concrete as seen in Table 8. Figure 6 (c and d) shows the microstructure of structural lightweight foamed concrete with 0.2% volume fraction of glass fibers. In these images it can be observed that a reduction of the voids within concrete due to the glass fibers affects the voids and weight of foam concrete. The density of structural lightweight foam concrete increased with the addition of glass fibers as seen in Table 8. Figure 6 (e and f) images for structural lightweight foamed concrete with 0.6% glass fibers. In this percentage of glass fibers the density of structural lightweight foamed concrete will increased and the voids decrease resulting enhance in performance of mechanical properties such as compressive and flexural strength as shown in Table 8.

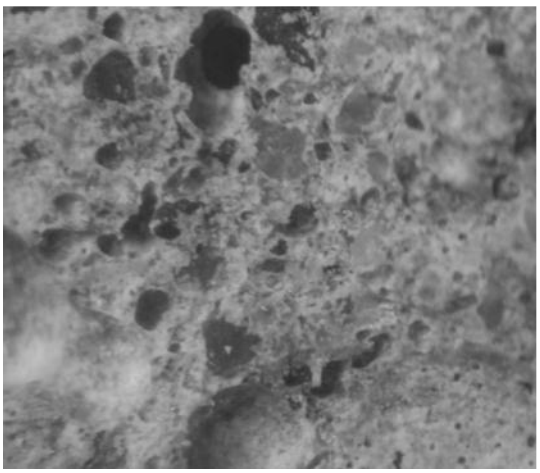

(a) Mix no. N0 24X

(b) Mix no. N5 24X

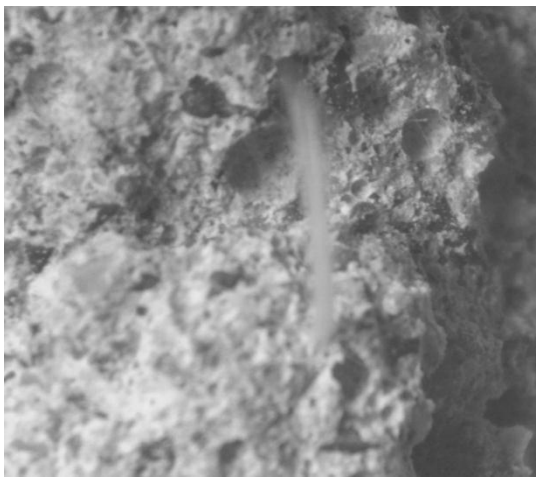

(c) Mix no. N2 24X

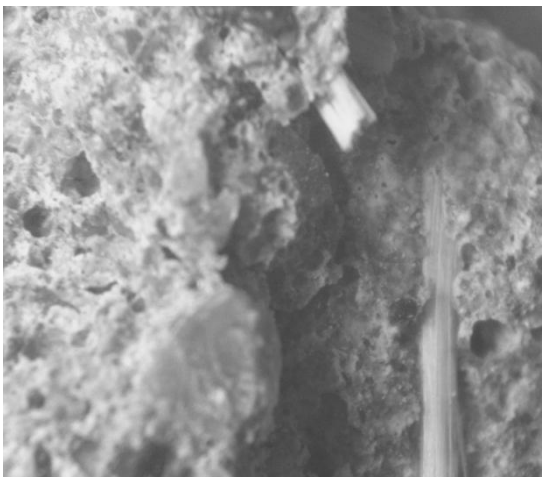

(d) Mix no. N7 24X

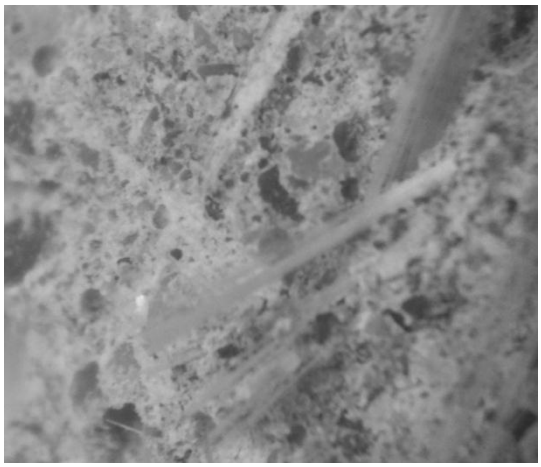

(e) Mix no. N4 24X

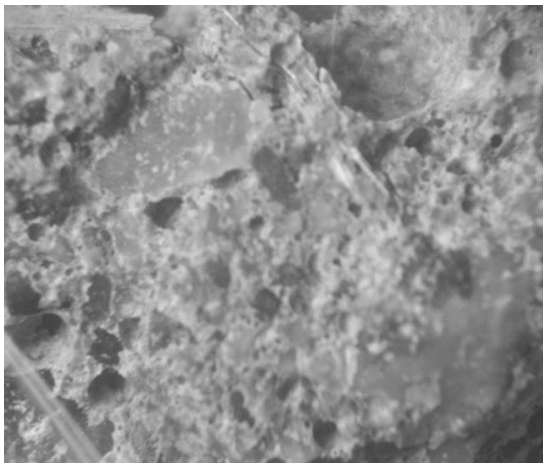

(f) Mix no. N9 24X

Note. (24X: mean the image zoom in 24 times)

Figure 6: Microstructure for structural lightweight foamed concrete for different mixes and density.

4.3. Compressive strength

The results of compressive strength at the age of 7 and 28 days are shown in Table 8. The compressive strength of structural lightweight foamed concrete incorporated with different percentage of glass fibers as 0.06, 0.2, 0.4, 0.6 % volume fraction. Compressive strength increases with the percentage increase of glass fibers as seen in Table 8 agree with (Deshmukh et al., 2012)[23]. Figure 7 shows the relationship between the compressive strength and percentage of glass fibers for two group mixes: series I and series II (without and with superplasticizer), respectively.

For series I mixes, it can be seen that the compressive strength increased by 14.28% with the addition of 0.06% of glass fibers compared with reference mix N0. Also, it can be noticed that the compressive strength is increased by 35.2% with the addition of 0.2% of glass fibers. Whereas, the incorporation of 0.4% glass fibers the compressive strength increased by about 45.2% compared with mix N0, and the compressive strength increased by about 51% with the addition of 0.6% of glass fibers as shown in Figure 7.

For series II mixes, also the compressive strength increased with the glass fibers increase, the compressive strength increased by about 26.2% with the addition of 0.06% of glass fibers compared with reference mix N5. The addition of 0.2% of glass fibers would increase the compressive strength by about 48.1%. However, the incorporation of 0.4% of glass fibers increases the compressive strength by about 45.3%. Furthermore, the compressive strength increases by about 60.6% with the addition of 0.6% glass fibers as can be noticed in Figure 7.

The results of compressive strength of series II mixes containing superplasticizer show the compressive strength at early age (7 days) exhibits better performance compared with mixes without superplasticizer (series I). Figure 8 shows the gain in compressive strength of foam concrete for mixes with and without superplasticizer (series II and series I).

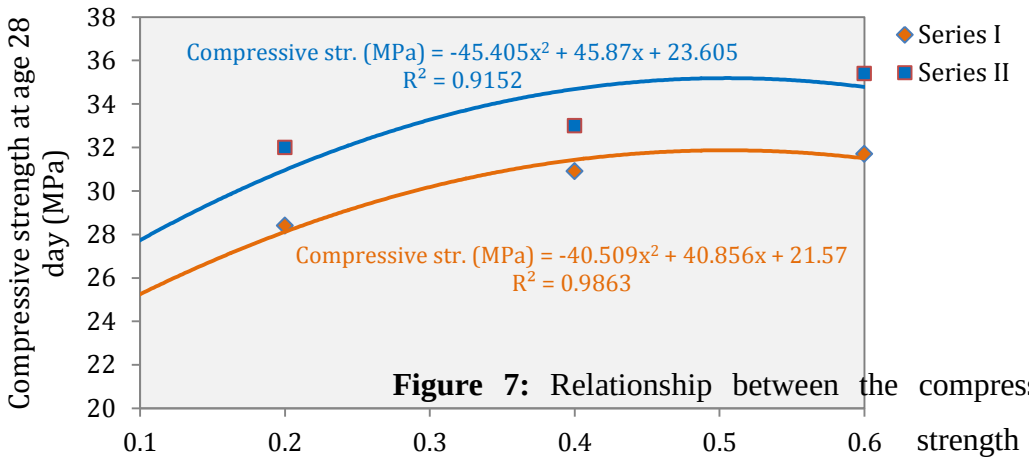

Figure 7: Relationship between the compressive strength at 28 day and percentage of glass fibers.

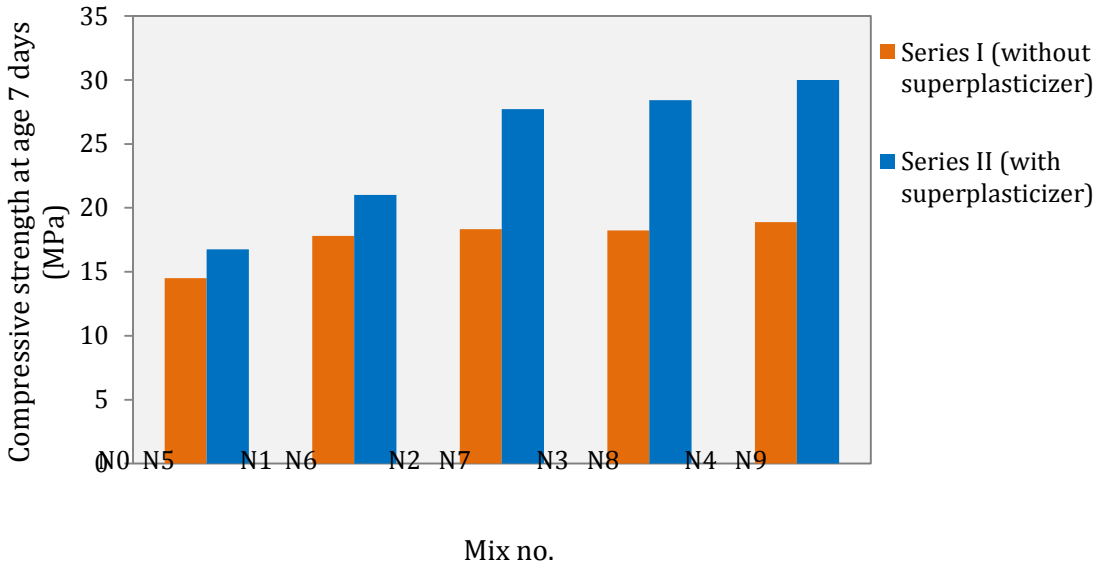

Figure 8: The influence of the addition of superplasticizer on the early strength at age 7 days of foam concrete

Table 8.

Hardened structural lightweight foamed concrete properties.

Series	Mix No.	Fresh density (kg/m³)	Dry density (kg/m³)	Compressive strength (MPa)		Increase (%)	Flexural strength (MPa)	Increase (%)	Voids (%)
				7 days	28 day		28 day		
Series I	N0	1760	1718	14.50	21.00	------	7.48	------	20.0
	N1	1784	1759	17.8	24.50	14.2	7.87	5.2	19.4
	N2	1810	1787	18.34	28.40	35.2	8.06	7.7	18.8
	N3	1850	1824	18.23	30.50	45.2	8.44	12.8	18.5
	N4	1881	1868	18.88	31.70	51.0	8.92	19.2	18.0
Series II	N5	1775	1731	16.75	22.03	------	6.90	------	19.7
	N6	1819	1795	21.00	27.80	26.2	7.48	8.4	18.6
	N7	1845	1822	27.73	32.64	48.1	7.68	11.3	18.0
	N8	1870	1849	28.42	32.00	45.3	7.86	14.0	17.8
	N9	1886	1861	30.00	35.40	60.6	8.16	18.2	17.7

4.4. Flexural strength

Table 8 gives the test results of flexural strength at 28 days. For series I mixes, the average flexural strength without glass fibers mix N0 is 7.48 MPa. However, the addition of glass fibers will enhance the flexural strength of structural lightweight foamed concrete with glass fibers percentage increase. It can be observed that the flexural strength increased by about 5% with the addition of 0.06% glass fibers compared with mix N0. The use of 0.2% of glass fibers would increase the flexural strength by about 7.7%. Besides, the flexural strength increased by about 12.8% with the addition of 0.4% glass fibers. Whereas, the use of 0.6% glass fibers increases the flexural strength of foamed concrete by about 19.2%. Figure 9 shows the relationship between flexural strength and glass fibers percentage. It can be noticed that flexural strength of foamed concrete increases with the glass fibers increase, agree with (Chandramouli et al., 2010 ; Deshmukh et al., 2012).

For series II mixes the average flexural strength without glass fibers mix N5 is 6.9 MPa. It can be observed that the flexural strength increased by about 8.4% with the addition of 0.06% glass fibers compared with reference mix N5 as can be noticed in Table 8. The flexural strength increases with the addition of 0.2% of glass fibers and the percentage of increase is 11.3%. The flexural strength increases by about 14% with the addition of 0.4% of glass fibers, and the incorporation of 0.6% glass fibers

increases the flexural strength by about 18.2% as shown in Figure 9. Figure 10 (a & b) seen the structural lightweight foamed concrete and structural lightweight foamed concrete with glass fibers for prism specimen after flexural test.

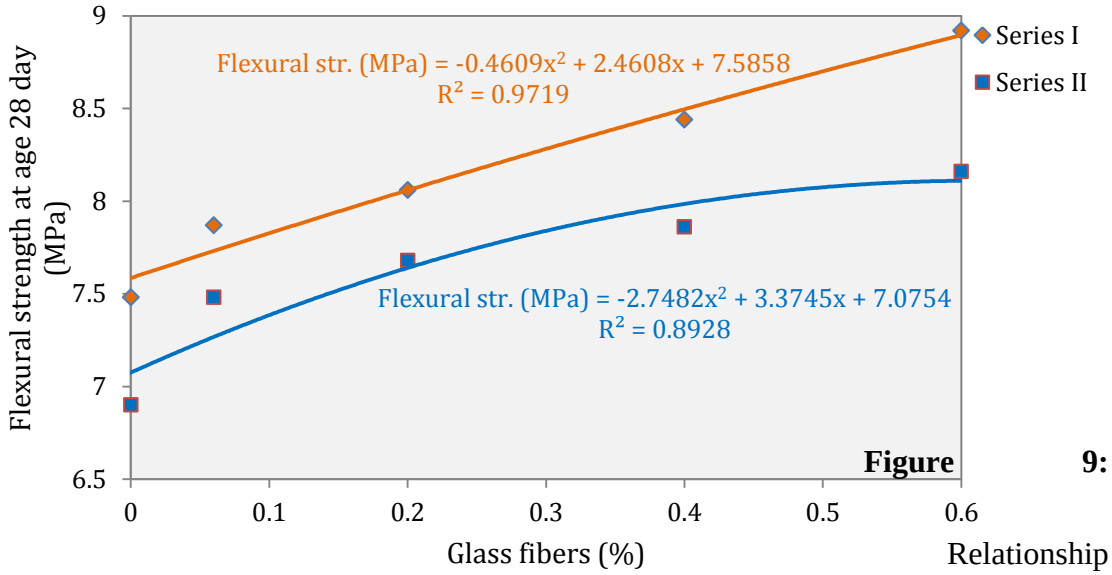

Figure 9: Relationship between flexural strength and glass fiber percentage.

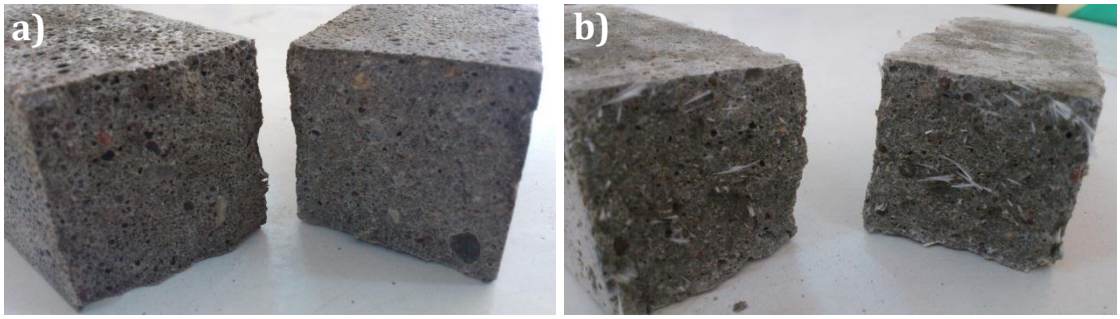

Figure 10: a) The structural lightweight foamed concrete for prism specimen after flexural strength testing (mix N0). **b)** The structural lightweight foamed concrete addtion glass fibers for prism specimen after flexural strength testing (mix N3).

4.5. Ultrasonic Pulse Velocity Measurements

Figure 11 shows the relationships between UPV and compressive strength at the age of 28 days of structural lightweight foamed concrete and structural lightweight foamed concrete with superplasticizer. It can be obsorved that the pulse velocity of structural lightweight foamed concrete without superplasticizer ranges from 3.37 to 3.7 km/sec at age 28 day, and the pulse velocity of structural lightweight foamed concrete with superplasticizer ranges from 3.49 to 3.84 km/sec at age 28 day, the observation of figure 11, it is show that UPV increase with increase compressive

strength of strucutral lightweight foamed concrete (Bungey et al., 2006)[24]. the data in Figure 11 illustrates the mathematical correlations for direct manner ultrasonic pulse test methods.

The relationship between UPV and dry density can be obsorved in Figure 12. The voids and pores were found to be effective on the reading of UPV. The density of structural lightweight foamed concrete increases with the UPV reading increase.

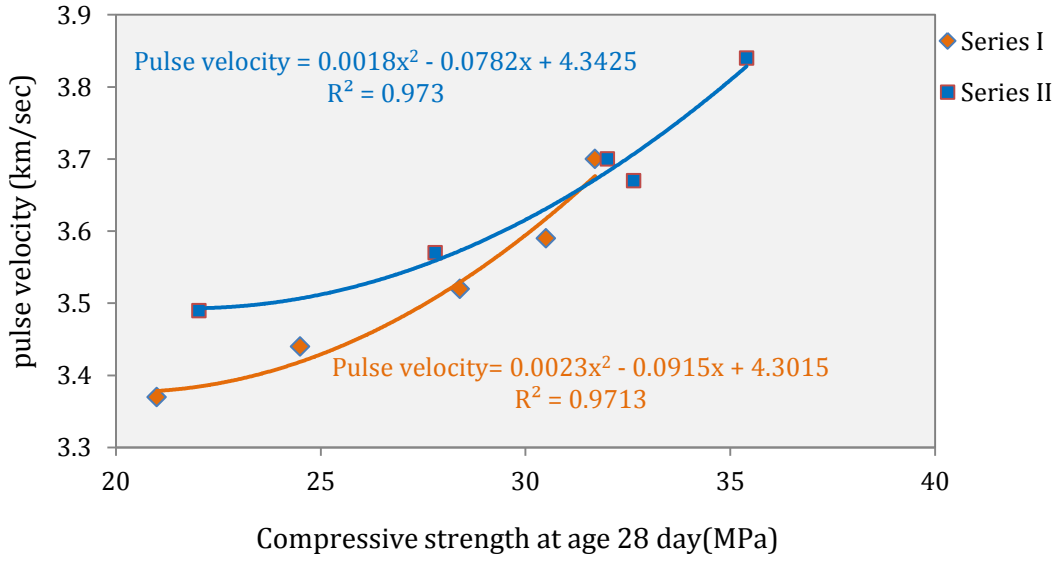

Figure 11: The relationship between compressive strength and pulse velocity.

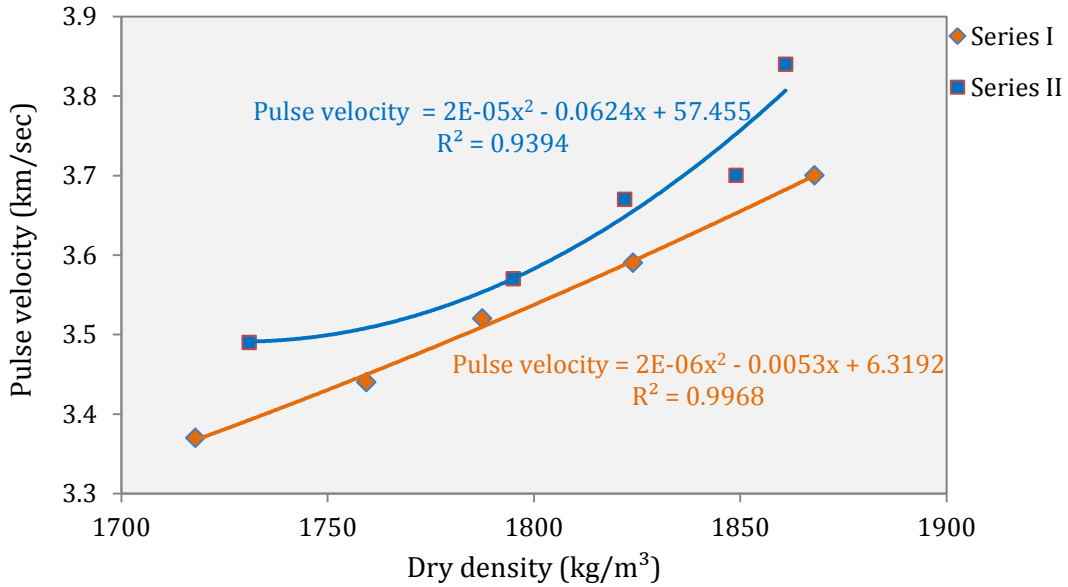

Figure 12: The relationship between dry density and pulse velocity.

5. Conclusion

In this paper Structural lightweight foamed concrete produced by using foam agent, with average density of 1750-1850 kg/m^3. Glass fibers and superplasticizer used in mixes. The glass fibers are used as reinforcement for foamed concrete to enhance the mechanical properties of such concrete. From the results we draw the following conclusions.

1. The workability of structural lightweight foamed concrete decrease with the increase of glass fibers percentages. The least value of flow is 84% with the use of 0.6% of glass fibers. This reduction in workability may be influenced by the high percentage of glass fibers. The increase of percentage of glass fiber more than 0.6% will significantly reduce the workability.
2. The microstructure of structural lightweight foamed concrete show that the percentages of glass fibers is more effective on internal voids of structural lightweight foamed concrete. The density increases with glass fibers percentage increase leading to a reduction in internal voids within structural lightweight foamed concrete.
3. The UPV reading was 3.37 to 3.7 km/sec for mixes without superplasticizer and 3.49 to 3.84 km/sec with superplasticizer, that's mean UPV reading will increase with the increase of density. Besides UPV reading would increase with compressive strength of strucutral lightweight foamed concrete increase.
4. The compressive strength of structural lightweight foamed concrete increases with the increase of glass fibers percentages in the mixes. For mixes without superplasticizer the best glass fibers percentages used are 0.2 and 0.4% , and for mixes with superplasticizer the best percentage is 0.6%. For all percentages of glass fibers in the mixes it can be observed increase in compressive strength would obtain with the volume fraction of glass fibers. For mixes without superplasticizer the compressive strength increases up to 51% with the addition of 0.6% glass fibers, and for mixes with superplasticizer the flexural strength increases by 60.6% with the addition of 0.6% of glass fibers.
5. The flexural strength increases with the increase of glass fibers percentages in the mixes. For mixes without superplasticizer the flexural strength increases up to 19.2% with the addition of 0.6% glass fibers, and for mixes with superplasticizer the flexural strength increases by 18.2% with the addition of 0.6% of glass fibers.

References

[1] Kamarulzaman, N. B., 2010, 'An investigation on effect of quarry dust as sand replacement on compressive and flexural strength of foam concrete', bachelor of civil engineering thesis, universiti Malaysia Pahang.

[2] Owens, P. , Newman, J. and Choo B. S. , 2003, *Advanced Concrete Technology Processe*, Elsevier Ltd.

[3] Libre, N. A., Shekarchi, M., Mahoutian, M., and Soroushian, P., 2011, 'Mechanical properties of hybrid fiber reinforced lightweight aggregate concrete made with natural pumice', Construction and Building Materials, vol. 25, pp. 2458–2464.

[4] Li, Z., 2010, *Advanced Concrete Technology*, John Wiley & Sons, Canada, pp. 317.

[5] Fouad, H. F. , Lamond, J. F. and Pielert J. H. , 2006, *Significance of Tests and Properties of Concrete and Concrete-Making Materials* , stp 169d , ASTM International.

[6] Ramamurthy, K., Kunhanandan Nambiar, E. K. and Indu Siva Ranjani, G. , 2009, ' A classification of studies on properties of foam concrete', cement and concrete composites, vol. 31, pp. 388-396.

[7] Zahari, N. M., Rahman, I. A., and Ahmad Zaidi, A. M., 2009, 'Foamed Concrete: Potential Application in Thermal Insulation', Malaysian Technical Universities Conference on Engineering and Technology, pp. 47-52.

[8] Dawood, E. T., and Ramli, M., 2011, 'High strength characteristics of cement mortar reinforced with hybrid fibres', Construction and Building Materials, vol. 25, pp. 2240–2247.

[9] Abdullah, M. M., and Jallo, E. K., 2012, 'Mechanical properties of glass fiber reinforced concrete', Al-Rafidain Engineering, vol. 20, no. 5, pp. 128-135.

[10] Chandramouli, K., Srinivasa R. P., Pannirselvam N., Seshadri, S.T.,andSravana, P., 2010, 'Strength properties of glass fibre concrete', Journal of Engineering and Applied Sciences, vol. 5, no. 4, pp. 1-6.

[11] IQS No: 5, 1984"Characteristics of OPC" Central Agency for standardization and quality control, Iraq.

[12] ASTM C 33-02a, 2002, standard specification for concrete aggregates, annual book of ASTM, standards, vol. 04.02.

[13] Hassan, S. A., 2012, 'Effect of elevated temperatures on bond strength of steel reinforcement and concrete enhanced with discrete carbon fibers', Journal of Engineering and Development, vol.16, no.4, pp.30-46.

[14] ASTM C 1437-01, 2001, Standard test method for flow of hydraulic cement mortar, annual book of ASTM, standards, vol. 04.01.

[15] ASTM C 230-03a, 2003, Standard specification for flow table for use in tests of hydraulic cement, annual book of ASTM, standards, vol. 04.01.

[16] ASTM C 109/C 109M-99, 1999, Standard test method for compressive strength of hydraulic cement mortars (using 2-in. or [50-mm] cube specimens), annual book of ASTM, standards, vol. 04.01.

[17] ASTM C 348-02, 2002, Standard test method for flexural strength of hydraulic cement mortar, annual book of ASTM, standards, vol. 04.01.

[18] ASTM C 192, 2002, Standard practice for making and curing concrete test specimens in the laboratory, annual book of ASTM, standards, vol. 04.02.

[19] ASTM C 642-97, 1997, Standard test method for density, absorption, and voids in hardened concrete, annual book of ASTM, standards, vol. 04.02**.**

[20] Neville, A.M. & Brooks, J.J. , 2010, *Concrete Technology*, second edition, Prentice Hall, Pearson Education, pp. 339-352.

[21] Mydin, M. O. and Soleimanzadeh, S., 2012, 'Effect of polypropylene fiber content on flexural strength of lightweight foamed concrete at ambient and elevated temperatures', advances in applied science research, vol. 35, pp. 2837-2846.

[22] Awang, H., Mydin, M. O., and Roslan, A. F., 2012,'Microstructural investigation of lightweight foamed concrete incorporating various additives', international journal of academic research, .vol. 4. no. 2, pp. 196-200.

[23] Deshmukh S.H., Bhusari J. P, and Zende A. M., 2012, 'Effect of glass fibres on ordinary portland cement concrete', IOSR journal of engineering, vol. 2, pp.1308-1312.

[24] Bungey, J. H., Millard S. G., and Grantham, M. G., 2006, *Testing of Concrete in Structures*, fourth edition, published in the Taylor & Francis e-Library.